



HAL
open science

Numerical and Experimental Investigation of Water and Cryogenic Cavitating Flows

Maria Giovanna Rodio

► **To cite this version:**

Maria Giovanna Rodio. Numerical and Experimental Investigation of Water and Cryogenic Cavitating Flows. Fluid mechanics [physics.class-ph]. Università degli studi di Lecce, 2011. English. NNT : . tel-00924556

HAL Id: tel-00924556

<https://theses.hal.science/tel-00924556>

Submitted on 7 Jan 2014

HAL is a multi-disciplinary open access archive for the deposit and dissemination of scientific research documents, whether they are published or not. The documents may come from teaching and research institutions in France or abroad, or from public or private research centers.

L'archive ouverte pluridisciplinaire **HAL**, est destinée au dépôt et à la diffusion de documents scientifiques de niveau recherche, publiés ou non, émanant des établissements d'enseignement et de recherche français ou étrangers, des laboratoires publics ou privés.

UNIVERSITÀ DEL SALENTO

Dipartimento di Ingegneria dell'Innovazione
CREA - Centro Ricerche Energia ed Ambiente

Ph.D Thesis
in "Sistemi Energetici ed Ambiente"
XXIII Ciclo

Numerical and Experimental Investigation of Water and Cryogenic Cavitating Flows

Coordinatore

Ch.mo Prof. Ing. Domenico LAFORGIA

Tutors

Ch.mo Prof. Ing. Antonio FICARELLA

Ch.ma Prof.ssa Ing. Maria Grazia DE GIORGI

Studente

Ing. Maria Giovanna RODIO

Anno Accademico 2010-2011

Alla mia famiglia

A Pietro

Numerical and Experimental Investigation of Water and Cryogenic Cavitating Flows

by

Maria Giovanna Rodio

(ABSTRACT)

The accuracy of the numerical simulation in the prediction of cavitation in cryogenic fluids is of critical importance for the efficient design and performance of turbopumps in rocket propulsion systems. One of the main challenges remains the efficiency in modeling the physics, handling the multi-scale properties and developing robust numerical methodologies. Such flows involve thermodynamic phase transition and cavitation bubbles smaller than the global flow structure. Cryogenic fluids are thermo-sensible, then thermal effects and strong variations in fluid properties can alter the cavity properties.

The aim of this work is to address the challenge of efficiently modeling cavitating flows when using water and cryogenic fluids. Because of the complexity of the phenomenon, we focus on improving accuracy of the numerical simulation and on proposing some approaches for a strong coupling between numerics and experiments.

We first discuss how to simulate cavitation by means of a mixture model. We specifically address two challenges. The first one is associated with the prediction of thermal effect during the phase transition, requiring the solution of the energy conservation equation. The second challenge is associated to the prediction of the number of bubbles, by considering a transport equations for the bubble density. This study is applied to the numerical simulation of a cavitating flow in a Venturi configuration. We observe an improved estimation of temperature and pressure profiles by using the energy equation and the nucleation model.

Secondly, we focus on bubble dynamics. Several forms of Rayleigh-Plesset (RP) equations are solved in order to estimate the temperature and pressure during the collapse of the bubble. We observe that, for high Mach number flows, RP modified with a compressible term can predict the bubble behavior more accurately than the classical form of RP. It is necessary to use a complex equation of state for non-condensable gas (van der Waals) in order to have an

accurate estimation of the bubble temperature during the collapse phase. We first apply this approach to the water treatment with cavitation, by proposing a model for the estimation of radicals developed during the collapse of the bubble. Secondly, this equation is modified by adding a term of convective heat transfer at the interface between liquid and bubble and it is coupled with a bubbly flow model in order to assess the prediction of thermal effect. We perform a parametric study by considering several values and models for the convective heat transfer coefficient, h_b , and we compare temperature and pressure profiles with respect to the experimental data. We observe the importance of the choice of h_b for correctly predicting the temperature drop in the cavitating region and we assess the most efficient models.

In addition, we perform an experimental study on nitrogen cavitating flows in order to validate numerical prediction of thermal effect, and in order to assess the fundamental characteristics of the nucleation and the transient growth process of the bubble.

Acknowledgments

I have to thank Professor Domenico Laforgia for giving me the opportunity to do a Ph.D.. I have to thank Professor Maria Grazia De Giorgi and Professor Antonio Ficarella for their guidance and support over the last three years. I have to thank Professor Jean Pierre Franc for his strong support during my research period at INPG in Grenoble, and for his collaboration in the period after.

Publications

- [1] M.G.Rodio, M.G. De Giorgi and A. Ficarella, *Influence of convective heat transfer modeling on estimation of thermal effect in cryogenic cavitating flows*. Submitted to International Journal of Heat and Mass Transfer.
- [2] M.G. De Giorgi, A.Ficarella and M.G.Rodio, *Cavitation Modeling in Cryogenic Fluids for Liquid Rocket Engine Applications*, AIAA-2008-3842, 19th AIAA Computational Fluid Dynamics Conference, June 2008, Seattle (USA).
- [3] M.G. De Giorgi, P.M. Congedo, M.G.Rodio and A.Ficarella, *Shape Optimization for cavitating flows in Liquid Rocket Engine*. FEDSM2008 2008 ASME Fluids Engineering Conference, 10-14 August, 2008 , Jacksonville (USA).
- [4] M.G. De Giorgi, A.Ficarella, M.G.Rodio and D. Laforgia, *Flow Visualization Study On Two-Phase Cryogenic Flow*. ILASS 2008, 8-10 September, 2008, Como Lake, Italy.
- [5] M.G. De Giorgi, A.Ficarella, M.G.Rodio, *CFD Modeling of Two phase Cryogenic Flow in an Internal Orifice*. Ansys Italy Conference 2008, 16-17 October, 2008, Mestre, Italy.
- [6] M.G. De Giorgi, M.G.Rodio and A.Ficarella, *Thermodynamic Effects On Cavitation In Water And Cryogenic Fluids*. ASME 2010 10th Biennial Conference on Engineering Systems Design and Analysis (ESDA 2010), 12-14 July 2010, Istanbul, Turkey.
- [7] M.G. De Giorgi, A.Ficarella, M.G.Rodio, *Modellazione ed analisi sperimentale di flussi bifase criogenici*. 63° Congresso Nazionale ATI, Palermo, 2008.
- [8] Antonio Ficarella, Marco Milanese, Antonio Trevisi, M.G.Rodio and Domenico Laforgia, *Analisi Di Scenario Per La Riduzione Delle Emissioni Inquinanti Nella Regione Puglia*. 63° Congresso Nazionale ATI, Palermo, 2008.
- [9] Report (in french), Simulation Numrique de la Dynamique dune Bulle de

Cavitation: Application au Traitement de l'Eau, Institut National Polytechnique de Grenoble (INPG), 2009.

Contents

Nomenclature	7
List of Figures	8
1 Introduction	17
2 State Of Art	21
2.1 Cavitation Modeling	21
2.2 Nucleation Modeling	22
2.3 Water Treatment with Cavitation	24
2.4 Thermal Effect Modeling	25
First Part: Numerical Study	28
3 Homogeneous Equilibrium Model and Nucleation Theory	29
3.1 HEM Model	29
3.2 Nucleation Theory	35
3.2.1 Model of Nucleation	35
3.3 Test Cases	38
3.4 Results	42
3.5 Conclusions	43
4 Bubble Dynamics and Water Treatment	47
4.1 Introduction	47
4.2 Rayleigh-Plesset Equation	48
4.2.1 Classical Rayleigh-Plesset Equation	48
4.2.2 Rayleigh-Plesset Equation with Compressible Term	48
4.3 Bubble Collapse Phenomenon	49
4.4 Rayleigh-Plesset Equation Discretization	50

CONTENTS

4.4.1	The Runge-Kutta Fehlberg method	51
4.4.2	The Runge-Kutta method with TVD	53
4.4.3	Comparison of Two Discretization Methods	54
4.5	Results	59
4.5.1	Validation	59
4.5.2	Influence of Equation of State	60
4.5.3	Compressible Effect Evaluation	67
4.5.4	Radicals estimation	67
4.6	Conclusions	74
5	Thermal Effects	76
5.1	Governing Equations	76
5.1.1	Quasi-1D Model	76
5.1.2	Ansys-Fluent Model	83
5.2	Test Cases	85
5.3	Grid Convergence for 1D CFD code	88
5.4	Results and Discussion	88
5.4.1	Constant Convective Heat Transfer Coefficient h_b	91
5.4.2	Theoretical Models for the Estimation of Convective Heat Transfer Coefficient $h_b(x)$	105
5.4.3	Ansys-Fluent Results	107
5.5	Conclusions	123
	Second Part: Experimental Study	125
6	Experimental Study	126
6.1	Experimental Nucleation in Cavitating Flow	126
6.1.1	Experimental Set-Up	126
6.1.2	Results	128
6.1.3	Conclusions	133
6.2	Experimental Thermal Effect in Water and Cryogenic Cavi- tating Flow	137
6.2.1	Experimental Set-Up	138
6.2.2	Mathematical Model	139
6.2.3	Results	139
6.2.4	Conclusions	143
7	Conclusions	153

CONTENTS

A	Classical Equation of Rayleigh-Plesset	157
B	Rayleigh-Plesset equation with compressible effect	160
	Bibliography	161

Nomenclature

A	cross section area [m^2]
C	mass concentration
c	speed of sound [m/s]
c_p	specific heat capacity [J/(kg K)]
h_b	convective heat transfer coefficient [$kg/(s^3 K)$]
H_b	enthalpie [J]
J	nucleation rate [$1/m^3s$]
$K(T)$	equilibrium constant [m^3/mol]
k	politropic coefficient, Runge-Kutta method coefficient
L	length of nozzle [m]
L_{ev}	latent heat [J/kg]
$M_{v,g}$	vapor or gas molar mass
n_b	number of bubbles for mixture volume [$1/m^3$]
p	liquid pressure [Pa]
p_c	critical pressure [Pa]
p_g	non-condensable gas pressure [Pa]
p_{dw}	downstream pressure [Pa]
p_{uw}	upstream pressure [Pa]
P_{ext}	upstream pressure [Pa]
p'_{turb}	turbulent fluctuations pressure [Pa]
R, R_b	bubble radius [m]
R_c	critical bubble radius [m]
r	spherical coordinate
S	surface tension [N/m]
T	temperature [K]
t	time [s]
u	liquid velocity [m/s]
v	bubble velocity [m/s]

CONTENTS

V_{ch}	characteristic velocity [m/s]
x	axial coordinate [m]
λ, K	thermal conductivity [W/(m K)]
η	bubble population per unit liquid volume [$1/m^3$]
ν	kinetic viscosity [m^2/s]
μ	dynamic viscosity [Pa s]
ρ	density [kg/m^3]
χ	density [kg/m^3]
σ	density [kg/m^3]
<i>Subscripts</i>	
0	upstream condition
l	liquid
v	vapor
b	bubble
∞	infinity - far from bubble
sat	saturation
<i>Dimensionless group</i>	
\bar{A}	A/A_0 dimensionless cross-sectional area
\bar{R}	R/R_0 dimensionless bubble radius
\bar{t}	tu_0/R_0 dimensionless time
\bar{u}	u/u_0 dimensionless liquid velocity
\bar{v}	v/u_0 dimensionless bubble velocity
\bar{x}	x/R_0 dimensionless x coordinate
$\bar{\eta}$	η/R_0^3 dimensionless bubble population per unit liquid volume
C_p	pressure coefficient
C_{pMIN}	minimum fluid pressure coefficient
C_D	drag coefficient
\bar{L}	L/R_0 dimensionless length of the nozzle
M	Mach number
n_{H_2O}	vapor mol number
n_{OH}	radicals mol number
Nu	Nusselt number
Pe	Peclet number
Pr	Prandtl number
Re	Reynolds number
α	Weber number
Φ	potential

List of Figures

1.1	Phase diagrams	18
1.2	Cavitation Erosion	19
1.3	Vapor Density Of three Cryogenic Fluids	20
3.1	Variations of the normalized Gibbs activation energy G_b and the critical radius with respect to the reduced superheat temperature T_l/T_c for water and for cryogenic fluid (H_2)	38
3.2	Variations of the homogeneous and heterogeneous nucleation rate J with respect to the reduced superheat temperature T_l/T_c for water and for cryogenic fluid (H_2) at room pressure	39
3.3	Variations of the heterogeneous nucleation rate J with respect to the pressure ratio p_l/p_v for water at $T = 500.8K$ and for cryogenic fluid (H_2) at $T = 22.69K$ and $22.49K$	39
3.4	Ventury geometry	40
3.5	Comparison between pressure profiles of three cavitation model for the two test cases. Simulation 1 and simulation 15, ME mechanical equilibrium model. Simulation 4 and simulation 18, TE thermal equilibrium model. Simulation 9 and simulation 20, SP full cavitation model.	44
3.6	Comparison between pressure profiles obtained by using thermal equilibrium model (TE) and the mechanical equilibrium (ME) model with and without nucleation effects. Simulation 1 and 15, ME. Simulation 4 and 18, TE. Simulation 2 and 16, ME with nucleation. Simulation 5 and 19, TE with nucleation.	44

LIST OF FIGURES

3.7	Comparison between pressure profiles obtained by using ME model for the two test cases with and without nucleation and energy effects. Simulation 1 and 15, ME. Simulation 2 and 16, ME with nucleation. Simulation 3 and 17, ME with nucleation and energy.	45
3.8	Comparison between vapor fraction profiles for the test case 125A. Simulation 3, ME with nucleation and energy. Simulation 5, TE with nucleation. Simulation 9, SP. Experimental cavity length equal to 0.0191 m [1].	45
3.9	Comparison between numerical and experimental temperature profiles for the test case 125A. Simulation 3, ME with nucleation and energy.	46
4.1	Comparison of temporal bubble radius profiles, obtained by the resolution of classical RP (Eq.(4.2)), using three stage Runge-Kutta TVD and four stage Runge-Kutta Fehlberg 4-5. Bubble at a constant temperature during growth phase ($\gamma = 1$). Adiabatic compression if the bubble radius lower than R_0	55
4.2	Zoom of last four rebounds of Fig.4.1	56
4.3	Comparison of temporal temperature variation, obtained by the resolution of classical RP (Eq.(4.2)), using three stage Runge-Kutta TVD and four stage Runge-Kutta Fehlberg 4-5. Bubble at a constant temperature during growth phase ($\gamma = 1$). Adiabatic compression if the bubble radius lower than R_0	57
4.4	Zoom of last five collapses of Fig.4.1	58
4.5	Behavior of an air bubble with initial radius $R_0 = 2mm$ in the water at standard condition ($T = 20C; P_0 = 1atm$). Pressure wave with frequency $f = 10kHz$ and amplitude $P_a = 2.7bar$. Comparison between the profiles obtained by Leighton [2] and by in-house code, solving a classical RP equation	61
4.6	Comparison of temporal radius evolution obtained with the in-house code (RP1, RP2 and RP3) and numerical and experimental profiles. In this case $R_0 = 4.5\mu m$, $f = 26.5kHz$, $\sigma = 0.03kg/s^2$, $c_{l\infty} = 1481m/s$, $\mu = 0.003kg/m$ and $P_a = 1.35atm$. The bubble is supposed at constant temperature ($\gamma = 1$) and the properties are uniform in the bubble.	62

LIST OF FIGURES

4.7	Zoom of first collapse of Fig.(4.6). Comparison of profiles obtained by RP1, RP2 and RP3 and by Lofstedt [3] with Eq.(4.14)	63
4.8	a) Zoom of first collapse of Fig.4.6. b) Comparison of profiles obtained by RP1 and by Lofstedt [3] with Eq.(4.14)	63
4.9	(a) Comparison of radius profiles obtained by RP1 with the hypothesis of PFG and VDW EOS. (b) Zoom of 2 th , 3 th and 4 th maximum radius. (c) Zoom of first collapse of (a). (d) Temperature profiles.	64
4.10	(a) Comparison of radius profiles obtained by RP2 with the hypothesis of PFG and VDW EOS. (b) Zoom of 2 th , 3 th and 4 th maximum radius. (c) Zoom of first collapse of (a). (d) Temperature profiles.	65
4.11	(a) Comparison of radius profiles obtained by RP3 with the hypothesis of PFG and VDW EOS. (b) Zoom of 2 th , 3 th and 4 th maximum radius. (c) Zoom of first collapse of (a). (d) Temperature profiles.	66
4.12	Comparison between radius evolution profiles obtained by classical RP and by RP1 (with liquid compressible effect) in the case described by Yuan [4]	68
4.13	Comparison between radius evolution profiles obtained by classic RP and by RP1 (with liquid compressible effect) in the case described by Lofstedt [3]	69
4.14	Comparison of OH radicals estimations obtained by RP1 with van der Waals EOS and with perfect gas EOS in the test case described by Yuan[4].	71
4.15	Comparison of OH radicals estimations obtained by RP2 with van der Waals EOS and with perfect gas EOS in the test case described by Yuan[4].	72
4.16	Comparison of OH radicals estimations obtained by RP3 with van der Waals EOS and with perfect gas EOS in the test case described by Yuan[4].	73
5.1	Partial view of experimental apparatus reproduced in this study.	86
5.2	B_{EXP} compared with (a) cavitation number σ , (b) inlet temperature T_0 , (c) Reynolds number Re and (d) theoretical temperature drop ΔT^*	87
5.3	Profiles of bubble radius R in 121B case [1] obtained by using four different grids.	89

LIST OF FIGURES

5.4	Profiles of liquid velocity in 121B case [1] obtained by using four different grids.	90
5.5	Comparison of temperature profiles for the case 121B [1] with $h_b = 1 \times 10^{+10}$ at different upstream vapor fraction α_0 and initial radius $R_0 = 1 \times 10^{-04}m$. The experimental temperature error is of $\pm 0.1K$	93
5.6	Comparison of vapor fraction profiles for the case 121B [1] with $h_b = 1 \times 10^{+10}$ at different upstream vapor fraction α_0 and initial radius $R_0 = 1 \times 10^{-04}m$	94
5.7	Comparison of absolute value of thermal (T-E) and pressure (P-E) effects for a $h_b = 1 \times 10^{+10}$ at different upstream vapor fraction α_0 and initial radius $R_0 = 1 \times 10^{-04}m$	95
5.8	Comparison of temperature profiles for the case 121B [1] with $h_b = 1 \times 10^{+05}$ at different upstream vapor fraction α_0 and initial radius $R_0 = 1 \times 10^{-04}m$. The experimental temperature error is of $\pm 0.1K$	96
5.9	Comparison of vapor fraction profiles for the case 121B [1] with $h_b = 1 \times 10^{+05}$ at different upstream vapor fraction α_0 and initial radius $R_0 = 1 \times 10^{-04}m$	97
5.10	Comparison of absolute value of thermal (T-E) and pressure (P-E) effects for a $h_b = 1 \times 10^{+05}$ at different upstream vapor fraction α_0 and initial radius $R_0 = 1 \times 10^{-04}m$	98
5.11	Comparison between numerical bubble temperature T_b and experimental temperature for the case 134[1], with $Re = 9.9 \times 10^{+06}$, $T_0 = 20.69$, $\sigma = 2.01$ and $\alpha_0 = 1 \times 10^{-03}$.The experimental temperature error is of $\pm 0.1K$	99
5.12	Comparison between numerical liquid pressure P_l and experimental liquid pressure for the case 134[1], with $Re = 9.9 \times 10^{+06}$, $T_0 = 20.69$, $\sigma = 2.01$ and $\alpha_0 = 1 \times 10^{-03}$.The experimental pressure error is of $\pm 6900Pa$	100
5.13	h_{bMAX} , h_{bOPT} and h_{bMIN} obtained for each case, with respect to B-factor.	101
5.14	h_{bMAX} , h_{bOPT} and h_{bMIN} obtained for each case, with respect to cavitation number σ	102
5.15	h_{bMAX} , h_{bOPT} and h_{bMIN} obtained for each case, with respect to Reynolds number.	103
5.16	h_{bMAX} , h_{bOPT} and h_{bMIN} obtained for each case, with respect to T_0/T_c (with critical temperature $T_c = 33.145K$)	104

LIST OF FIGURES

5.17	Comparison between bubble temperature T_b , obtained with the Ranz& Marshall [5], Oresta <i>et al.</i> [6], Christopher <i>et al.</i> [7] model, and experimental temperature for the case 125A, with $Re = 6.2 \times 10^{+06}$, $\sigma = 1.3$, $Pr = 1.1917$, $T_0 = 22.69$ and $\alpha_0 = 5 \times 10^{-04}$	107
5.18	Comparison between bubble temperature T_b , obtained with the Ranz&Marshall [5], Oresta <i>et al.</i> [6], Christopher <i>et al.</i> [7] model, and experimental temperature for the case 120B, with $Re = 7.6 \times 10^{+06}$, $\sigma = 1.3$, $Pr = 1.2541$, $T_0 = 20.36$ and $\alpha_0 = 2 \times 10^{-04}$	108
5.19	Comparison between bubble temperature T_b , obtained with the Ranz&Marshall [5], Oresta <i>et al.</i> [6], Christopher <i>et al.</i> [7] model, and experimental temperature for the case 123B, with $Re = 6.2 \times 10^{+06}$, $\sigma = 1.3$, $Pr = 1.1917$, $T_0 = 22.69$ and $\alpha_0 = 4 \times 10^{-05}$	109
5.20	Comparison between liquid pressure P_l , obtained with the Ranz&Marshall [5], Oresta <i>et al.</i> [6], Christopher <i>et al.</i> [7] model, and experimental temperature for the case 125A, with $Re = 6.2 \times 10^{+06}$, $\sigma = 1.3$, $Pr = 1.1917$, $T_0 = 22.69$ and $\alpha_0 = 5 \times 10^{-04}$	110
5.21	Comparison between liquid pressure P_l , obtained with the Ranz&Marshall [5], Oresta <i>et al.</i> [6], Christopher <i>et al.</i> [7] model, and experimental temperature for the case 120B, with $Re = 7.6 \times 10^{+06}$, $\sigma = 1.3$, $Pr = 1.2541$, $T_0 = 20.36$ and $\alpha_0 = 2 \times 10^{-04}$	111
5.22	Comparison between liquid pressure P_l , obtained with the Ranz&Marshall [5], Oresta <i>et al.</i> [6], Christopher <i>et al.</i> [7] model, and experimental temperature for the case 123B, with $Re = 6.2 \times 10^{+06}$, $\sigma = 1.3$, $Pr = 1.1917$, $T_0 = 22.69$ and $\alpha_0 = 4 \times 10^{-05}$	112
5.23	Comparison between bubble radius, obtained with the Ranz&Marshall [5], Oresta <i>et al.</i> [6], Christopher <i>et al.</i> [7] model, and experimental temperature for the case 125A, with $Re = 6.2 \times 10^{+06}$, $\sigma = 1.3$, $Pr = 1.1917$, $T_0 = 22.69$ and $\alpha_0 = 5 \times 10^{-04}$	113
5.24	Comparison between bubble radius, obtained with the Ranz&Marshall [5], Oresta <i>et al.</i> [6], Christopher <i>et al.</i> [7] model, and experimental temperature for the case 120B, with $Re = 7.6 \times 10^{+06}$, $\sigma = 1.3$, $Pr = 1.2541$, $T_0 = 20.36$ and $\alpha_0 = 2 \times 10^{-04}$	114

LIST OF FIGURES

5.25 Comparison between bubble radius, obtained with the Ranz&Marshall [5], Oresta *et al.* [6], Christopher *et al.* [7] model, and experimental temperature for the case 123B, with $Re = 6.2 \times 10^{+06}$, $\sigma = 1.3$, $Pr = 1.1917$, $T_0 = 22.69$ and $\alpha_0 = 4 \times 10^{-05}$ 115

5.26 Comparison between convective heat transfer coefficient h_b , obtained with the Ranz&Marshall [5], Oresta *et al.* [6], Christopher *et al.* [7] model, and experimental temperature for the case 125A, with $Re = 6.2 \times 10^{+06}$, $\sigma = 1.3$, $Pr = 1.1917$, $T_0 = 22.69$ and $\alpha_0 = 5 \times 10^{-04}$ 116

5.27 Comparison between convective heat transfer coefficient h_b , obtained with the Ranz&Marshall [5], Oresta *et al.* [6], Christopher *et al.* [7] model, and experimental temperature for the case 120B, with $Re = 7.6 \times 10^{+06}$, $\sigma = 1.3$, $Pr = 1.2541$, $T_0 = 20.36$ and $\alpha_0 = 2 \times 10^{-04}$ 117

5.28 Comparison between convective heat transfer coefficient h_b , obtained with the Ranz&Marshall [5], Oresta *et al.* [6], Christopher *et al.* [7] model, and experimental temperature for the case 123B, with $Re = 6.2 \times 10^{+06}$, $\sigma = 1.3$, $Pr = 1.1917$, $T_0 = 22.69$ and $\alpha_0 = 4 \times 10^{-05}$ 118

5.29 Comparison between temperature profiles, obtained with the Ranz&Marshall [5] and Christopher *et al.* [7] model and with 1D and 2D code for the case 121B [1] with $\alpha_0 = 1 \times 10^{-04}$ and initial radius $R_0 = 1 \times 10^{-04}m$. The experimental temperature error is of $\pm 0.1K$ 119

5.30 Comparison between convective heat transfer coefficient, obtained with the Ranz&Marshall [5] and Christopher *et al.* [7] model and with 1D and 2D code for the case 121B [1] with $\alpha_0 = 1 \times 10^{-04}$ and initial radius $R_0 = 1 \times 10^{-04}m$. The experimental temperature error is of $\pm 0.1K$ 120

5.31 Comparison between the contour of mass transfer, obtained with the Ranz&Marshall [5] and Christopher *et al.* [7] model in 2D code for the case 121B [1] with $\alpha_0 = 1 \times 10^{-04}$ and initial radius $R_0 = 1 \times 10^{-04}m$. The experimental temperature error is of $\pm 0.1K$ 121

5.32 Comparison of vapor contour, obtained with the Ranz&Marshall [5] and Christopher *et al.* [7] model in 2D code for the case 121B [1] with $\alpha_0 = 1 \times 10^{-04}$ and initial radius $R_0 = 1 \times 10^{-04}m$. The experimental temperature error is of $\pm 0.1K$ 122

LIST OF FIGURES

6.1	Experimental Set-Up	128
6.2	Sketch of the Experimental Set-up	129
6.3	Visualization flow test section.	129
6.4	Test section particular.	129
6.5	Distribution of density of activated nuclei density for different cavitation numbers.	132
6.6	Standard deviation of downstream pressure signals for different cavitation numbers	133
6.7	FFT Amplitude Spectrum of the upstream pressure for different cavitation numbers	134
6.8	FFT Amplitude Spectrum of the downstream pressure for different cavitation numbers.	134
6.9	FFT Amplitude Spectrum of accelerometer for different cavitation numbers.	135
6.10	Maximal Amplitude obtained at $400Hz$ of downstream pressure signal at different cavitation numbers.	135
6.11	$S(0 - 10kHz)$ function for the downstream pressure signal at different cavitation numbers.	137
6.12	Test section for water and nitrogen cavitation experimental analysis. The lengths are in mm and the nozzle depth is 10mm.	139
6.13	Experimental set-up for water cavitation.	140
6.14	Experimental set-up for nitrogen cavitation.	140
6.15	Fourier transformation (FFT) amplitude spectrum of the upstream pressure signals for the nitrogen fluid at $T = 82K$ at different cavitation numbers σ	143
6.16	Fourier transformation (FFT) amplitude spectrum of the upstream pressure signals for the nitrogen fluid at $T = 82K$ and $\sigma = 1.55$, and for water at $\sigma = 8$ and at two different temperatures, $T = 293K$ and $T = 348K$	144
6.17	Amplitude spectrum of the image brightness for the nitrogen fluid at $T = 82K$ at different cavitation numbers.	144
6.18	Comparison between the FFT image brightness and the FFT of pressure signals for water at $T = 293K$ and at $\sigma = 8.0$	145
6.19	Comparison between the FFT image brightness and the FFT of pressure signals for water at $T = 348K$ and at $\sigma = 8.0$	145

LIST OF FIGURES

6.20 Bubble radius distributions in tested converging-diverging nozzle ($C_{pMIN} = -10$), obtained respectively by assuming $T_c = T_\infty$ and $T_c \neq T_\infty$, for water at $T = 348K$ ($Re = 1000$, $\sigma = 8$, $\alpha_0 = 5 \times 10^{-7}$, $R_0 = 0.0001$). 146

6.21 Bubble radius distributions in experimentally tested converging-diverging nozzle ($C_{pMIN} = -10$), for water at $T = 348K$ and $T = 293K$, by the isothermal calculations ($\alpha_0 = 5 \times 10^{-8}$, $R_0 = 0.0001$). 147

6.22 Bubble radius distributions in the nozzle ($C_{pMIN} = -1$), for water at different temperatures ($Re = 1000$, $\alpha_0 = 2.5 \times 10^{-6}$, $\sigma = 0.8$, $R_0 = 0.0001$ and $C_{pMIN} = -1$). 148

6.23 Bubble radius distributions in converging-diverging nozzle ($C_{pMIN} = -10$), obtained respectively by assuming $T_c = T_\infty$ and $T_c \neq T_\infty$, for nitrogen at $T = 82K$, $\alpha_0 = 5 \times 10^{-7}$, $R_0 = 0.0001$. . . 149

6.24 Nitrogen Bubble radius distributions in nozzle ($C_{pMIN} = -10$), obtained by assuming $T_c \neq T_\infty$ ($T = 82K$, $\alpha_0 = 5 \times 10^{-6}$, $R_0 = 0.0001$, $h_b = 5 \times 10^{+05}$). 150

6.25 Nitrogen bubble radius and temperature distributions ($C_{pMIN} = -10$ obtained by assuming $T_c \neq T_\infty$, ($T = 82K$, $\alpha_0 = 5 \times 10^{-6}$, $R_0 = 0.0001$, $h_b = 5 \times 10^{+05}$, $\sigma = 1.9$). 151

6.26 Experimental normalized image brightness, for the axial centerline, for the nitrogen fluid at $T = 82K$ at different cavitation numbers. 152

Chapter 1

Introduction

The present work is devoted to the analysis of cavitation in water and cryogenic flows. Cavitation is a phenomenon characterized by the formation of vapor or gas bubbles in the liquid. It happens when the liquid pressure falls below the vapor pressure inducing a phase transition (Fig.1.1). Cavitation can assume several forms, see Franc *et al.* [8] for a detailed explanation, depending on the flow configuration, on the geometry, the liquid properties, the forces applied on the flow and so on. It is very difficult to give a comprehensive definition of a so complex phenomenon. Basically, it is possible to distinguish between two types of cavitation: (i) Ultrasonic cavitation and (ii) Hydrodynamic cavitation. In the first case i), gas bubbles in the liquid are supposed to be in thermodynamic equilibrium and they are subjected to an oscillating pressure that determines the bubble grow or collapse. In the second case ii), cavitation is produced by a pressure drop due to the flow configuration and geometry, such as for example in a convergent-divergent nozzle. In this case, as explained by Brennen [9], bubbles of non-condensable gas, which are present into the liquid bulk due to a homogeneous and heterogeneous nucleation process, could become the nuclei of cavitation. In the low pressure region, during phase transition gas bubbles can become gas-vapor bubbles and they can grow. Moreover, on some low-pressure points close to the wall, vapor bubbles can develop and determine a *blade cavitation* or *pocket cavitation* [9].

The study of cavitation is of great interest in several industrial applications, like as in fuel injection, hydraulic turbines, pumps, rocket engine system and in all the applications where a drop of pressure could appear [10]. If there is the formation of some bubbles, they can be transported

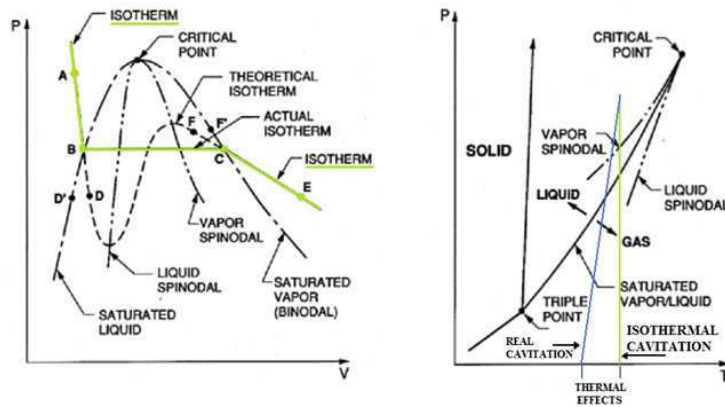


Figure 1.1: Phase diagrams: (left) pressure-volume; (right) pressure-temperature.

by liquid flow and collapse in higher pressure regions, creating the following problems:

- Reduction of machine performances
- Noise emission
- Erosion (Fig.1.2).

However, in some fields cavitation is purposely induced [11]. For example, the bubble collapse is often used in order to induce chemical reactions, basing on the high pressure and temperature in the bubble.

Usually, the cavitation is considered as an isothermal phenomenon [9]. The phase transition is described by the pressure reduction, following the isothermal line (green) in the phase diagrams (Fig.1.1). This assumption is valid for example for water at room condition and is used usually in conditions far from critical temperature. On the contrary, in some fluids, the vapor production in cavitation extracts the latent heat of evaporation from the surrounding liquid. This decreases the local temperature and hence the local vapor pressure in the vicinity of cavity. This is known as *thermal effect* in cavitation [9]. Thermal effect become more important for cryogenic fluids. In this case, numerical and experimental studies have shown the necessity

to consider thermal effect for a reliable prediction. A typical mixture constituted by a combination of liquid oxygen (LOX) and liquid hydrogen (LH₂), is currently used as rocket propellant.



Figure 1.2: Image of typical cavitation damage on the blade of a mixed flow pump [9]

In the rocket engine, it is important to minimize the size and the weight of all the components. This requires that turbopump works with high impeller speeds. These high speeds generate a region of static pressures below the vapor pressure causing the propellant to cavitate around the inducer blades [10]. Then, these fluids are typically associated to a cavitation phenomenon, because they are used at temperatures close to the critical point and at very low pressure. In these conditions the vapor density is much greater than far from the critical point [12]. Then, cryogenic fluids demand more heat to cavitate and thermal effects can not be neglected.

A good estimation of the loads on the inducer blades is fundamental in order to design efficiently the whole system. Because of the complexity of the phenomenon, numerical and experimental studies show great deficiencies. In this work, several numerical and experimental methodologies have been proposed in order to reduce some of these deficiencies.

The present work is presented showing numerical developments in the first part and the experimental results in the second one.

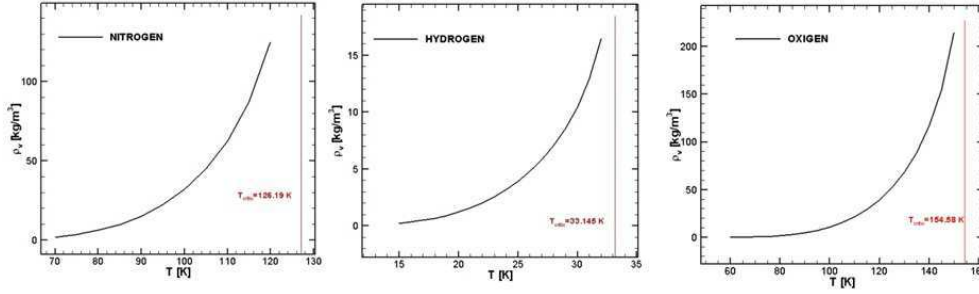


Figure 1.3: Profiles of vapor density as function of temperature along the saturation curve for nitrogen, hydrogen and oxygen liquid fluids.

In chapter 3, different cavitation models have been proposed in order to simulate cryogenic flows. Thermal and nucleation effects have been taken into account, solving the transport equations for the bubble density and energy conservation. The performances of these models have been compared with the available experimental data. In chapter 4, bubble dynamics have been studied by means of four differential equations, based on Rayleigh-Plesset equation. This model links together the dynamic behavior to the global set of forces (mechanical, thermal, etc.) applied on the bubble. This study is then employed on the water treatment in cavitation. In chapter 5, thermal effect has been examined by adding a term of convective heat transfer at the interface between liquid and bubble in Rayleigh-Plesset equation. The aim of this study has been to improve the prediction of thermal effect by a more accurate estimation of convective heat transfer coefficient h_b . This study has been validated on an experimental test case, *i.e.* hydrodynamic cavitation in cryogenic flows.

In the second part of this manuscript (Chapter 6) an experimental study has been presented. In particular, nitrogen cavitating flows have been observed. This work allowed i) clarifying the fundamental characteristics of the nucleation and transient growth process bubbles, and ii) showing how the thermal effect could influence the development of cavitation.

The state of art for cavitation and for each aspects studied in this work, will be presented in the next chapter.

Chapter 2

State Of Art

In this chapter the state of art concerning previous cavitation studies is described. This section is divided in four paragraphs. The first one concerns the numerical cavitation modeling, the second one the nucleation theory, the third one describes the water treatment with cavitation and the fourth one, the thermal effects.

2.1 Cavitation Modeling

Several numerical models have been proposed to reproduce a cavitating flow (see for a detailed review [13, 14]). Two classes of models are available in literature: i) interface models and ii) the two-phase models. In the first approach (i), two phases co-exist, with a clear and distinct interface between the liquid and the vapor. Moreover the diffusion term in the equation is neglected. These models avoid the numerical difficulties associated to the diffusion term, but on the contrary the interface reconstruction and the re-meshing is a difficult task and really expensive in terms of computational cost [15, 14]. In the two phase models (ii), two known approaches exist depending on the mixture of the two phases. If this mixture is treated like as one, one-fluid method is considered. Otherwise, if co-existence of both phases are taken into account, bubbly flows and two-fluids methods are defined.

The one-fluid method, known also as HEM (Homogeneous Equilibrium Model), is based on the hypothesis of kinematic and thermodynamic equilibrium between the two phases (initial local velocity, temperature and pressure are the same for the two phases). Then, the governing equations are solved for

the mixture and the exchange terms are not solved. Due to its simplicity, this model is well used in the numerical simulation of cavitating flows. But, it presents several limitations. The first difficulty is to choose an equation of state (EOS) that allows reproducing all thermodynamic conditions of the mixture. It can not reproduce thermodynamic and kinetic non-equilibrium effects. Finally, the mixture EOS is valid only for flows constituted by the liquid and its vapor only. On the contrary, in many situations, the liquid is not a pure fluid and some non-condensable gases (air in water for example) are present. In this case the mixture EOS no longer holds. Moreover the vaporization or condensation processes are assumed to be instantaneous.

Among the two phase models, two other models are the bubbly flows or two-fluid model, obtained by considering the co-existence of both phases. In bubbly flows model, a continuous model for the mean flow, compressible or not is considered, with a microscopic model for the description of the bubble dynamics based on the Rayleigh equation. The drawbacks of this type of model consist in assuming that the gas phase must be present initially and that the flow topology is fixed. Moreover, the choice of some tuning parameters, such as the initial vapor fraction or the initial bubble radius (when an equation for the evolution of bubble radius is taken into account), is set up in order to reproduce the experimental data. The two-fluid method allows treating explicitly the mass, momentum and energy exchanges as transfer terms, and so obtaining a correct estimation of temperatures in liquid and vapor [16, 17]. However, these models are characterized by a difficulty to define the source term. In chapter 3, some of HEM models are used and coupled with thermal model and nucleation model. This coupling allows estimating whether thermal effects or a variable bubble number (cavitation nuclei) could influence the cavitation prediction. In chapter 4, a bubbly flow model is used in order to analyze thermal effects, in particular the importance of a correct estimation of convective heat transfer coefficient.

2.2 Nucleation Modeling

In the nucleation model the existence of cavitation nuclei is supposed, that in low pressure conditions could become vapor structures. Vapor bubbles may be generated in liquid (homogeneous nucleation), on a surface or other locations at the flow field boundaries (heterogeneous nucleation). In the first case, the formation of temporary microscopic voids are the nuclei for the

2.2. NUCLEATION MODELING

formation and growth of macroscopic vapor bubble. However, in engineering systems, bubble formation usually occurs in the form of heterogeneous nucleation, in which the bubble formation is induced by particular conditions at the interface between the solid wall and the liquid or between the liquid and the particles in the fluid. Becker and Doring [18] were the first to develop the nucleation theory, known in literature as classical approach. It is based on the hypothesis that the bubble formation is proportional to the minimum molecular energy needed for the critical cluster to survive. In this theory, the free energy of formation is given by:

$$ME_{CL} = \frac{16\pi\sigma^3}{3\Delta P^2}, \quad (2.1)$$

where $\delta P = p_l - p_v$ is the pressure difference between the liquid and the vapor pressure, σ is the surface tension of an equilibrium planar liquid-vapor interface.

Moreover, the small portions of the new phase are treated as if they present macroscopic regions of the space and, thus, the effects of droplet curvature on the rate of nucleation are not taken into account. As observed in several studies, the liquid cannot be cleaned of such impurities that catalyze inevitably to heterogeneous nucleation, and thus the nucleation theory has attracted a great deal of interest in several field of application, as boiling [19], cavitation erosion [20], acoustic cavitation and recently in microelectronics cooling or in MEMS application. In the case of cryogenic fluids, there are few impurities in normal conditions, but they may include non-condensable gas with an high probability to influence the bubble formation. For example, the liquid oxygen used in liquid rocket may include non-condensable gas of helium that is often used to compress liquid oxygen. In addition to the classical nucleation theory (CNT), others theories have been developed, where the effects of droplet curvature on the rate of nucleation are taken into account. Guilleumas and co-workers [21] studied the thermal cavitation of an isotope of helium (He-3) using the square-gradient density-functional approach. They observed a discrepancy of results when the liquid temperature is low. Dupont-Roc *et al.* [22] and successively Oxtoby *et al.* [23, 24] proposed the application of nonlocal density-functional approach to the study of He-3 and they observed, as in Guilleumas, that the classical theory over-estimates the nucleation rate by two orders of magnitude at high liquid temperature and under-estimates at low temperature. As observed by Tsuda *et al.* [25], the CNT could calculate the nucleation rate by starting from macroscopic physi-

cal values and it could describe qualitatively a change of nucleation rate even with a discrete accuracy. Tsuda *et al.* [25] investigated the bubble nucleation in liquid oxygen with dissolved impurities (nitrogen and helium molecules), using the classical nucleation theory. They observed that the nucleation is affected by the gas typology dissolved in the liquid. De Giorgi *et al.* [26] underlined the necessity to implement a cavitating flow model taking into account the nucleation, in particularly in the case of cryogenic flows. This paper has been widely described in Chapter 3.

2.3 Water Treatment with Cavitation

Usually, the cavitation phenomenon is considered very dangerous for machine performance. However, in several fields, cavitation is exploited as in the case of sonoluminescence or liquid treatment, as shown also in this manuscript. Due to complexity of phenomenon, several simplified hypothesis have been considered in water treatment field. In 1998, simple models have been considered, supposing the uniformity of fluid properties in the bubble and neglecting the chemical reactions and the transport phenomenon at the interface of bubble [13, 27]. Kamath *et al.* [28] estimated the radical production only on the base of temperature and pressure of bubble. In the 1995, Yasui [29] took into account the thermal conduction effects in the description of evaporation and condensation of water vapor. Successively, the same author pointed out the importance of liquid temperature estimation for a good prediction of bubble reaction due to sonoluminescence phenomenon. So, Yasui [30] coupled the bubble dynamic model with chemical reaction. Successively, he considered also the spatial variation of temperature close to interface. Finally, in the 2005, Yasui *et al.* [31] developed a model for the estimation of radical $[OH]$ by supposing an analytical approximation of the temperature at the interface. Sochard *et al.* [32] considered the diffusion of gas in the bubble and the vaporization and condensation through the bubble interface as Yasui [29], but by supposing the thermal equilibrium for the reactions. Yuan *et al.* [4], pointed out the importance of viscosity, thermal conductivity and superficial tension at the interface and in particular of the equation of state (EOS) for the estimation of temperature bubble at the center during the collapse. Lin *et al.* [33] pointed out the uniformity of pressure in the bubble and proposed the equation of Rayleigh-Plesset in order to model the bubble dynamics. Xu *et al.* [34] presented a complete model with all radial properties variation in

the bubble. Storey and Szeri [11, 35, 36] presented a model constituted by the Navier-Stokes equations for the mixture (gas+vapor) and by chemical reaction mechanisms. They pointed out that the vapor in the bubble induces the sonoluminescence phenomenon. A model very complex has been developed by Hauke et al. [37], including the dynamics of bubble and of liquid around, the radial properties variation, the chemical reactions and the mass and heat exchange at the interface.

2.4 Thermal Effect Modeling

A first quantification of thermal effects in cryogenic cavitation, has been assessed through the dimensionless coefficient B-factor proposed by Stahl *et al.* [38] and Stepanoff. [39]:

$$B = \frac{\Delta T}{\Delta T^*} \text{ and } \Delta T^* = \frac{\rho_v L_{ev}}{\rho_l c_{pl}}, \quad (2.2)$$

where B represents a ratio between the temperature drop determined in a cavitating flow and the theoretical temperature drop calculated by the liquid properties at the operating liquid temperature. This constitutes a prediction of the temperature drop in cavitating condition. Also other parameters for the estimation of thermal effects have been proposed and fully explained by Franc *et al.* [14]. When using cryogenic fluids, it seems necessary to include the effect of heat transfer in the cavitation model for a correct prediction of cavitation. As fully explained by Goncalves *et al.* [13] and Franc *et al.* [14], several numerical models have been proposed to simulate a cavitating flow and, also, to take into account the thermal effect. Two modeling approaches are available in literature: i) interface models and ii) the two-phase models. In the first approach (i), two phases co-exist and a clear and distinct interface between the liquid and the vapor is assumed. The difficulty of this method is the systematic reconstruction of interface [15, 14]. Conversely, in the two-phase models (ii), the liquid-vapor interface is not computed, but the cavitating flow is treated as a liquid-vapor mixture. Main differences between models in this class (ii) mostly come from the hypothesis to consider the mixture of the two phases behaving as one (one-fluid method) or to consider the co-existence of both phases, governed by its own set of conservation laws (two-fluids and hybrid methods). In order to take into account thermal effect, in the case of one-fluid method, an equation of state (EOS) can be

2.4. THERMAL EFFECT MODELING

used in order to define the thermodynamic behavior of the mixture [40, 41]. Goncalves *et al.* [13, 42] proposed an homogeneous equilibrium model with different EOS in order to reproduce a freon R-114 and liquid hydrogen cavitating flows. Also Goel *et al.* [43] proposed a sensitivity analysis on the empirical parameter of homogeneous cavitating model and on the uncertainties of material properties. The study underlines that in cryogenic flows the changes in model parameters influence the performances of cavitation model more than the uncertainties in material properties. However, the assumptions of kinematic and thermodynamic equilibrium impose the same local velocity, pressure and temperature of the two phases. In these studies and in others [44, 45], a gradient of temperature is obtained, but it is equal for both phases.

Considering the co-existence of both phases, allows treating explicitly the mass, momentum and energy exchanges as transfer terms [16, 17]. However, in these models there is a difficulty to define the term source and their tuning parameters, as the initial vapor fraction or the initial bubble radius (when an equation for the bubble growth is used), usually calibrated in order to reproduce the experimental data. When a convective heat exchange is considered between the two phases, it is necessary to use the convective heat coefficient h_b that represents the crucial parameter in the energy transfer term. Considering the importance of the convective heat transfer coefficient h_b , the aim of this study has been to investigate the influence of the convective heat transfer coefficient in the modeling of thermal effect in cavitating cryogenic fluid. There are two possibilities: (i) to consider a constant value of h_b chosen on the base of empirical values; (ii) to include in the cavitation model, a model for the estimation of h_b coefficient. Franc and Pellone [14] proposed a simple model to compare the convective approach and the conductive approach in order to model the heat transfer at the bubble wall. In both models tuning parameters appear that are the convective heat transfer coefficient and the eddy thermal diffusivity, respectively, for convective and conductive approach. Constant values have been imposed for the tuning parameters. Cavitating flows of Freon R114 in an inducer have been presented, showing that both models predict a cavity length close to the experimental data. However, these models presented some limitations due to simplifying assumptions. Calibration with respect to experiments is mandatory in order to use a correct value of h_b . Otherwise, an incorrect value of h_b could invalidate the predictive character of the global approach. So the calibration of empirical laws in order to predict the h_b coefficient is necessary. At

our knowledge, in literature, heat transfer in cavitating flows is object of experimental and numerical studies in boiling flow [46, 47, 7] and ultrasonic cavitation [48, 49, 50, 51], but values of convective heat transfer coefficient when hydrodynamic cavitation in cryogenic flows at high Reynolds number is taken into account, are not provided. Several models for the prediction of convective heat transfer coefficient have been proposed, but usually formulated for water and validated far from hydrodynamic cavitation conditions. This is due to the high complexity of cryogenic flows experiments and then to the difficulty to obtain a fitted model. For some aspects, the cryogenic cavitating flow is similar to the boiling flow, because, as explained before, the pressure decrease do not appear as an isothermal transformation, but it is coupled to a temperature drop in the liquid bulk. For this reason the model for the estimation of convective heat transfer coefficient have been studied for the boiling applications. Qi *et al.* [46] studied the flow boiling of liquid nitrogen in the micro-tubes. They tested four correlations for the estimation of heat flux in cryogenic fluids, but the models did not give excellent results in comparison to experimental data in micro-channel. Though some of these correlations have been tested for cryogenic fluids, however they are difficult to adapt for cavitating flow. Kim and Park [47] confirmed the importance of h_b parameter for the analysis of multi-phase flow. They performed experiments in order to correlate the interfacial heat transfer coefficient at low pressure in subcooled boiling flow. They obtained a new h_b estimation model. The Ranz and Marshall model [5] estimates the h_b coefficient as function of the bubble Reynolds number and Prandtl number.

Basing on the fact that cryogenic fluids are associated to a thermal effect, we focused also on others models, in which liquid or vapor temperature appears. For the estimation of h_b coefficient, Oresta *et al.* [6] proposed a model in order to fit two previous models obtained for low and very large Péclet number. This model has been tested in simulations to reproduce the phase transitional the two-phase flow in natural convection problems. This model, as in Ranz and Marshall model[5], is a function of Reynolds and Prandtl number, but also depends on the Jacob number. Finally, Christopher *et al.* [7] adopted a model for the estimation of h_b coefficient that is a function of bubble properties and conditions. Christopher [7] studied the bubble motion in a Marangoni flow, where the flow is driven by the non-uniform temperature distribution in the liquid inducing the well-known Marangoni effect. Then, the model has been adopted in a case in which the temperature is very high. This model has been also employed in our analysis.

First Part: Numerical Study

Chapter 3

Homogeneous Equilibrium Model (HEM) and Nucleation Theory

3.1 HEM Model

The multiphase nature of cavitating flow coupled with a complex physics yields a system of highly coupled governing equations. Furthermore, interfacial dynamics, compressibility effects, and turbulence constitute necessary ingredients for the numerical simulation of these physical phenomena. Three cavitation models have been implemented as external subroutines in Fluent commercial code (release 6.3):

- The classical thermal equilibrium cavitation model (called TE in the following), based on a simplified Rayleigh-Plesset equation [52].
- The mechanical equilibrium model (called ME) [53].
- The "full cavitation model" (called SP), developed by Singhal [54].

These models have been tested in their original form, numerically simulating some experimental test cases [1]. Their performances have been examined comparing the computed pressure and temperature profiles with the available experimental data. Then, a variable number density has been taken into account and a nucleation transport equation have been coupled to mixture models. As explained before, thermal effects are particularly significant in

3.1. HEM MODEL

cryogenic fluids, then in the last part of work the energy equation has also been taken into account with the others. Physically, cavitation is controlled by the thermodynamics and kinetics of the phase change. The liquid-vapor conversion associated with the cavitation process is modeled by means of two terms, which represents, respectively, condensation and evaporation. The particular form of these terms constitutes the base of the cavitation model. In the TE model, the mass source is related to the increase of the vapor bubbles radius, by considering the inertial effects induced by pressure difference between the bubble and the liquid. In the ME model, the enthalpy available to create the vapor phase is considered as a limiting factor for the bubbles growth, and the vapor mass source is evaluated by considering the heat transfer between the liquid and vapor phases. For all the three cavitation models, the vapor-liquid flow is treated as an homogeneous vapor-liquid mixture. The overall flow-field has been described by the Navier-Stokes equations. The cavitation models used in this study have been implemented in Fluent by a purposely-developed C routines. Considering, for the sake of simplicity, a 1D flow, the continuity equation for the vapor phase can be written as:

$$\frac{\partial \alpha_v \rho_v}{\partial t} + \frac{\partial \alpha_v \rho_v u}{\partial x} = \dot{m}_v. \quad (3.1)$$

The continuity equation for the liquid phase is:

$$\frac{\partial (1 - \alpha_v) \rho_l}{\partial t} + \frac{\partial (1 - \alpha_v) \rho_l u}{\partial x} = -\dot{m}_v. \quad (3.2)$$

The flow velocity u has been assumed to be the same for the two phases; ρ_l and ρ_v are the densities of the liquid and of the vapor phases, respectively; α_v is the vapor volume fraction, and \dot{m}_v represents the mass exchange rate between the liquid and the vapor phases. Assuming the liquid and the vapor densities constant, and substituting Eq.(3.2) into Eq.(3.1), the following equation can be written:

$$(\rho_l - \rho_v) \left(\frac{\partial \alpha_v}{\partial t} + u \frac{\partial \alpha_v}{\partial x} \right) = -\rho \frac{\partial u}{\partial x}, \quad (3.3)$$

where

$$\rho = \alpha_v \rho_v + (1 - \alpha_v) \rho_l. \quad (3.4)$$

Then, the continuity equation for the mixture is:

$$\frac{\partial \rho}{\partial t} + \frac{\partial \rho u}{\partial x} = 0. \quad (3.5)$$

3.1. HEM MODEL

Combining Eq.(3.4) and Eq.(3.5), the following equation can be obtained:

$$(\rho_l - \rho_v) \frac{D\alpha_v}{Dt} = \frac{D\rho}{\partial t}. \quad (3.6)$$

The vapor volume fraction can be related to the bubble radius R_b and to the bubble number density n_b , which is the nuclei concentration per unit volume of mixture. Usually n_b is taken as a constant. However, in the following paragraphs other results will be shown where a variable coefficient has been used. The vapor fraction has been computed as:

$$\alpha_v = \frac{4}{3} n_b \pi R_b^3. \quad (3.7)$$

The closure of the system of equations requires an appropriate cavitation model. The classical *thermal equilibrium cavitation model* is based on a simplified Rayleigh-Plesset approach [54]. The mass transfer is related to the growth of the vapor bubbles radius. The liquid and the vapor phase are supposed to be in thermal equilibrium, and then they are characterized by the same temperature. The model neglects the energy requirements related to the vapor formation (enthalpy difference between liquid and vapor phase). The basic hypothesis of this model argues that the limiting factor for the bubble growth is the mechanical energy necessary to displace the liquid in order to permit the growth of the bubble. The enthalpy transfer from the liquid to the vapor, that is necessary to provide the latent heat to the evaporating molecules, is not limiting the velocity of the vapor formation; the phase exchange depends only on the pressure difference between liquid and vapor in the surrounding of the bubble. The growth of the bubble radius, R_b , given by the simplified Rayleigh equation, is expressed as:

$$\frac{DR_b}{Dt} = \frac{|p_b - p|}{p_b - p} \left(\frac{2|p_b - p|}{3\rho_l} \right)^{1/2}. \quad (3.8)$$

In the above equation, p is the pressure at a large distance from the bubble, in the liquid phase (the value of pressure used in the momentum equation); p_b is the pressure in the liquid at the bubble boundary, that is considered equal to the vapor pressure in the bubble (neglecting the surface tension effects):

$$p_b = p_v(T), \quad (3.9)$$

3.1. HEM MODEL

where T is the same temperature for the liquid and vapor phases (mixture temperature, considered constant). A new approach with respect to the classical thermal model [54] has been used by taking into account the effect of turbulence on cavitating flows. Singhal [54] developed a numerical model, where a probability density function (PDF) approach has been used for considering the effects of turbulent pressure fluctuations. This approach required the estimation of the local values of the turbulent pressure fluctuations and the computations of the time-averaged phase-transition rates by integration of instantaneous rates in conjunction with assumed PDF for pressure variation in time:

$$p'_{turb} = 0.39\rho k. \quad (3.10)$$

The thermal cavitation model used in these calculations (called TE) accounts for the turbulence-induced pressure fluctuations by simply correcting the bubble pressure, p_v , that drives the radius growth, with the following:

$$p_v(T) = p_b p'_{turb}/2. \quad (3.11)$$

Using the simplified Rayleigh-Plesset equation of Eq.(3.8), and combining Eq.(3.1) and Eq.(3.7), the following equation can be written

$$\dot{m}_v = \left(\frac{\rho_l \rho_v}{\rho} \right) (4n_b \pi)^{1/3} (3\alpha_v)^{2/3} \frac{|p_b - p|}{p_b - p} \left(\frac{2|p_b - p|}{3\rho_l} \right)^{1/2}. \quad (3.12)$$

The so-called *full cavitation model* (SP), used in this study, has been developed by Singhal [54]. The working fluid has been assumed to be a mixture of liquid, vapor and non-condensable gases. The model is based on the simplified Rayleigh-Plesset approach, previously described; moreover, it accounts for some other first-order effects, as surface tension on the bubble surface, turbulent pressure fluctuations, and presence of non-condensable gases. The mass fraction of non-condensable gases has been considered constant and known in advance. Moreover, it has been expected the bubble collapse process to be different from that of the bubble growth: bubbles formation (evaporation) and collapse (condensation) have been treated in a slight different ways in the model. Eq.(3.10) could be further manipulated, considering the effects of the bubble surface tension and some physical limitations to bubbles size. The following expressions for vapor generation/condensation rates, \dot{m}_v , in terms of the vapor mass fraction χ_v , where ($\chi_v = \alpha_v \rho_v / \rho$), and the non-condensable mass fraction χ_g , where ($\chi_g = \alpha_g \rho_g / \rho$), can be derived,

3.1. HEM MODEL

considering the effects of turbulence-induced pressure fluctuations and non-condensable gases:

$$\dot{m}_v = (C_e \rho_l \rho_v V_{ch} / \sigma_{sup})(1 - \chi_v - \chi_g) \sqrt{2(p_b - p) / 3\rho_l} \quad \text{when } p < p_v, \quad (3.13)$$

$$\dot{m}_v = (C_c \rho_l \rho_v V_{ch} / \sigma_{sup})(\chi_v) \sqrt{2(p_b - p) / 3\rho_l} \quad \text{when } p > p_v, \quad (3.14)$$

where p_v is given by Eq.(3.10) and Eq.(3.11). In the above equation, σ_{sup} is the surface tension of the liquid, C_e and C_c are two empirical coefficients (the default values are $C_e = 0.02$ and $C_c = 0.01$) and V_{ch} is a characteristic velocity, which reflects the effect of the local relative velocity between liquid and vapor. In most turbulent flows, the local turbulent velocity fluctuations are also of this order. Therefore, as a first pragmatic approximation, V_{ch} can be expressed as the square root of local turbulent kinetic energy:

$$V_{ch} = \sqrt{k} \quad (3.15)$$

The *mechanical equilibrium model* (called ME), is based on the thermal transport processes, where the bubbles growth is related to energy (heat) transfer between the liquid and the vapor phases [19]. The mechanical energy requirements, necessary to displace the liquid in order to permit the growth of the vapor bubble, have been considered favorable for the bubble growth. The mass transfer can be evaluated by means of the heat flux between the liquid and the vapor bubble:

$$\dot{m}_v = \frac{\dot{q}_v}{\Delta h_{lv}}. \quad (3.16)$$

The interphase mass transfer is due to the heat transfer between the bubble and its surrounding liquid. If the liquid is overheated ($T_l > T_{sat}$), it has been assumed that the heat transfer (from the liquid to the vapor) determines the amount of the vaporized liquid phase. An useful assumption has been the following:

$$\dot{q}_v = A_b h_b (T_l - T_b), \quad (3.17)$$

where the vapor inside the bubbles is at the same pressure of the liquid (neglecting inertial and surface tension effects), $p_b = p$, and the saturation

3.1. HEM MODEL

temperature T_{sat} correspond to the saturation temperature for the local static pressure of the liquid, that is the so-called mechanical equilibrium hypothesis:

$$T_v = T_{sat}(p). \quad (3.18)$$

Then, considering the mechanical equilibrium hypothesis, the bubble and the liquid have been considered at the same pressure (neglecting the effects of the surface tension). The interfacial area density (total bubbles surface for unit volume of mixture) can be evaluated as:

$$A_b = 4n_b\pi R_b^2, \quad (3.19)$$

and hence,

$$\dot{q}_v = 3\frac{\alpha_v}{R_b}h_b(T_l - T_b). \quad (3.20)$$

The interphase heat transfer coefficient at the interphase of a spherical bubble can be approximated by:

$$h_b = \frac{Nu_b\lambda_l}{2R_b} = \frac{\lambda_l}{2R_b}(2 + 0.6Re^{1/2}Pr^{1/3}) \quad (3.21)$$

where Re is the Reynolds number and Pr the Prandtl number. The source term for the inter-phase mass transfer between the primary phase l (liquid) and the secondary phase (vapor) v , can be evaluated as the following (neglecting the slip velocity and the turbulent velocity fluctuations between the two phases):

$$\dot{m}_v = \frac{12\lambda_l\alpha_v}{2R_b^2\Delta h_{lv}}. \quad (3.22)$$

At the beginning of calculations, the vapor volume is zero as well as the interfacial area. When the liquid pressure falls below the vapor tension, a liquid-vapor temperature difference appears, but no vapor can grow because the interfacial area remains zero, as well as the heat transfer; then, only at the incipient cavitation conditions, a potential interface area could be calculated considering the critical (minimum) value of the bubbles radius:

$$R^* = \frac{2\sigma}{p_v(T_l) - p}. \quad (3.23)$$

In all the three cavitation models in which the mass transfer is defined, the bubble number density n_b appears. It can be defined constant [26] or it can

be modeled by a nucleation model [9]. Usually, the nucleation model is used in different fields of study as boiling [19], but the objective of this part of the study has been to verify whether the nucleation model, coupled with cavitation model, could give a better prediction of cavitation phenomenon. In the following section, the classical theory of nucleation has been analyzed.

3.2 Nucleation Theory

Ishii *et al.*[55] and Kocamustafaogullari [56] postulated that the number of bubbles in a given control volume can be conserved. Then by using the transport theorem, it follows that:

$$\frac{dn_b}{dt} = \int_v \frac{\partial N_b}{\partial t} dv + \int_S N_b \nabla \cdot u ds, \quad (3.24)$$

where N_b is the number density of the bubbles, n_b is the total number of bubbles and u is the velocity field. Then, for an infinitesimal control volume:

$$\frac{\partial N_b}{\partial t} + \text{div} N_b u = \text{total change of } n_b. \quad (3.25)$$

The change in N_b is induced from homogeneous nucleation in the bulk of the liquid (J_{HOM} , and heterogeneous nucleation on the surfaces (J_{HET} . A term involving bubble growth due to the disintegration of larger bubbles could also be included but it should be negligible because of the size of the bubbles at the initial phase of an expansion. The number density for one-dimensional flow is then given by:

$$\frac{\partial N_b}{\partial t} + u \frac{\partial N_b}{\partial x} + N_b \frac{\partial u}{\partial x} = J_{HOM} + J_{HET}. \quad (3.26)$$

3.2.1 Model of Nucleation

Considering a liquid at temperature T and at room pressure, if the temperature of the liquid is well above the boiling point or the room pressure is well below the saturation pressure p_v at a given temperature T , the system is metastable. Vapor bubbles may be generated in liquid (homogeneous nucleation), on a surface or at a corner (heterogeneous nucleation). In practice homogeneous bubble nucleation could occur in boiling at constant liquid pressure or in cavitation where the temperature of the liquid

3.2. NUCLEATION THEORY

remains constant. In practical situations, bubble formation is facilitated by the presence of an external surface which usually takes the form of dissolved or suspended impurities or the walls containing the metastable liquid. This is referred to as heterogeneous bubble nucleation. In the absence of such heterogeneities, formation of the vapor phase must take place entirely within the bulk metastable liquid, and this is called homogeneous bubble nucleation. The classical nucleation theory [19] indicates that nucleation begins after the "energy barrier" is overcome. Most theoretical treatments of nucleation have focused on the thermodynamic calculation of the free-energy barrier height. Thermodynamic and mechanical equilibrium on a curved vapor-liquid interface requires a certain degree of superheat in order to maintain a given curvature. In so-called classical nucleation theory which has historically provided the canonical description of nucleation phenomena, it is assumed that pre-critical and critical bubbles are macroscopic and uniform objects possess the properties of the thermodynamically stable phase. Within the classical framework, the free-energy barrier height for homogeneous bubble nucleation is given by

$$W_{CR} = \frac{16\pi\sigma^3}{3\Delta p_c^2}, \quad (3.27)$$

where

$$\Delta p_c = \frac{2\sigma}{R_c}, \quad (3.28)$$

and R_c is the critical radius for the growth of a spherical bubble. It is equal to:

$$R_c = \frac{2\sigma}{p_b - p_l} = \frac{2\sigma}{p_v(T) - p_l}, \quad (3.29)$$

where p_l denotes the pressure of the surrounding liquid. The number of bubble per unit of volume is related exponentially to the minimum work W_{CR} required to form the bubble:

$$n_b = N \exp\left(\frac{-W_{CR}}{kT}\right) = \frac{\rho_l}{MW} \exp(-G_b), \quad (3.30)$$

where N is the number density of liquid, MW is the molecular weight and G_b is the Gibbs normalized activation energy. The homogeneous nucleation rate (the rate of critical bubble formation) can be calculated by means of the following equation:

3.2. NUCLEATION THEORY

$$J_{HOM} = \frac{\rho_l}{MW} \left(\frac{2\sigma N_a}{B\pi MW} \right) \exp \left(-\frac{3\pi\sigma^3}{3kT(p_v(T) - p_l)} \right), \quad (3.31)$$

where B is a coefficient which takes into account chemical or mechanical equilibrium. In this study $B = 2/3$ and N_A is the Avogadro number. As it is shown, in most situations the temperature has a value for which the homogeneous nucleation rate can be negligible. This implies that bubble nucleation does not occur in the bulk of liquid but mainly on the walls or on impurities in the liquid (heterogeneous nucleation). In this case the only contribution is the heterogeneous nucleation rate given by

$$J_{HET} = \left(\frac{\rho_l}{MW} \right)^{2/3} \frac{1-m}{2} \left(\frac{2\sigma N_a}{B\pi MW} \right)^{1/2} \exp \left(-\frac{16\pi\sigma^3}{3kT(p_v(T) - p_l)} \Phi \right), \quad (3.32)$$

where J_{HET} is an heterogeneous factor which physically implies that the molecular clusters formed on a rough surface or suspended particles need less energy to survive.

Φ and m are linked by the following equation:

$$\Phi = \frac{2 - 3m + m^2}{4}, \quad (3.33)$$

where m is equal also to $-\cos\theta$ where θ is the contact angle at the bubble surface. Finally, the number of density is expressed by Eq.(3.26). This equation has been implemented in the numerical code by external user defined sub routines. Comparisons of the predicted values for the Gibbs activation energy (Fig.3.1) showed that the cryogenic fluid has a smaller value of the Gibbs normalized activation energy, that means an higher tendency to nucleate. This have been confirmed by the plot of the critical radius for the two fluids in function of the reduced superheat temperature T_l/T_c , where it is clear that the critical clusters have smallest critical radii in the case of cryogenic fluid. Looking to Fig.3.2, it is possible to appreciate that the homogeneous nucleation in water is only possible when the reduced superheat temperature T_l/T_c is higher than 0.86. Then, in most practical situations this temperature is not reached and the bubble generation does not occur in the bulk of the liquid but mainly on the walls. In fact the heterogeneous nucleation rate is different from zero for smaller values of the reduced superheat temperature T_l/T_c . Comparisons with the hydrogen showed that the

3.3. TEST CASES

nucleation starts for low temperatures in particular for the case of the heterogeneous nucleation. The exponential terms of Eq.(3.31) vary slower with temperature than the exponential. At room pressure (see Fig.3.2) homogeneous nucleation in water occurs at about $0.89T_c$. At this temperature the predicted rate of homogeneous nucleation is about 10^{10} bubbles $m^{-3}s^{-1}$ and its value change of two order of magnitude per degree Celsius. At the same pressure, homogeneous nucleation in hydrogen starts at $0.78T_c$ and the nucleation rate is about 10^{13} bubbles $m^{-3}s^{-1}$. This value changes of ten orders of magnitude per degree Celsius. The exponential term of heterogeneous nucleation rate is lower than the exponent of the homogeneous nucleation rate for the presence of the factor Φ , that is lower than 1. This means that bubbles on a rough surface need less energy to survive. The heterogeneous nucleation in hydrogen flow occurs also at very low temperature and for small pressure difference between the saturated vapor and the superheated liquid.

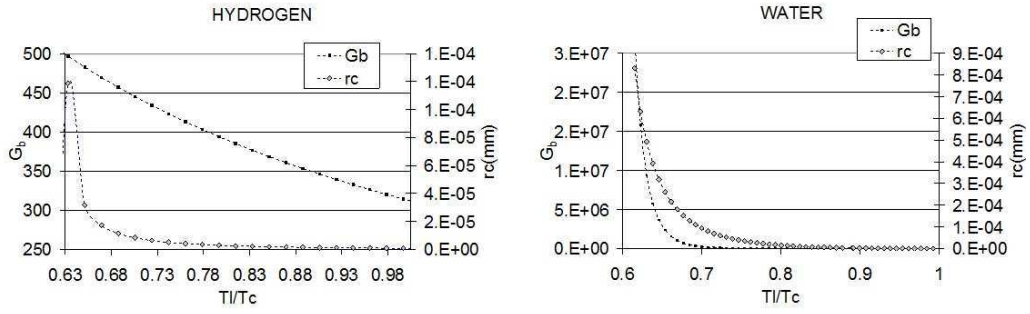


Figure 3.1: Variations of the normalized Gibbs activation energy G_b and the critical radius with respect to the reduced superheat temperature T_l/T_c for water and for cryogenic fluid (H_2)

3.3 Test Cases

Numerical simulations have been performed by using the commercial code FLUENT. The numerical model uses an implicit finite volume scheme, based on a Pressure-Velocity Coupling algorithm, associated with multiphase and cavitation model. The code solves the Navier Stokes equations, for the conservation of mass and momentum, and other scalars, such as turbulence, and

3.3. TEST CASES

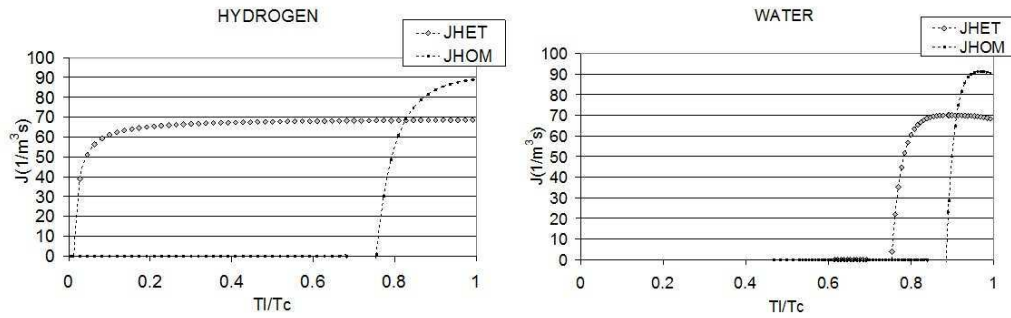


Figure 3.2: Variations of the homogeneous and heterogeneous nucleation rate J with respect to the reduced superheat temperature T_i/T_c for water and for cryogenic fluid (H_2) at room pressure

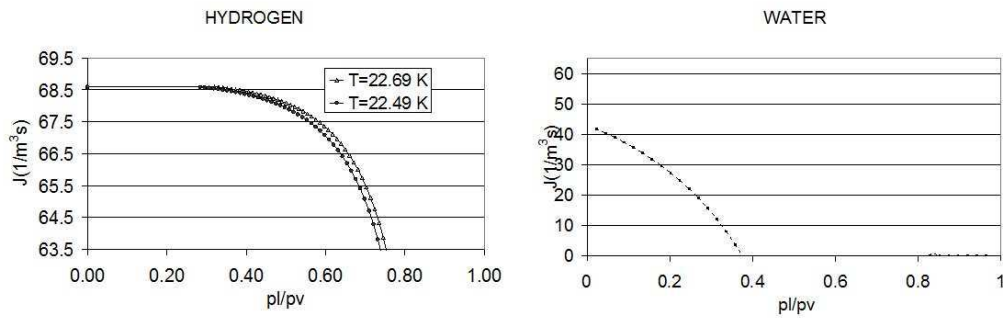


Figure 3.3: Variations of the heterogeneous nucleation rate J with respect to the pressure ratio p_l/p_v for water at $T = 500.8K$ and for cryogenic fluid (H_2) at $T = 22.69K$ and $22.49K$.

3.3. TEST CASES

CASES	$T_0(K)$	$V_0(m/s)$	$P_0(N/cm^2)$	$P_v(N/cm^2)$
125 A	22.69	32.5	24.11	19.44
132 A	22.49	57.2	38.40	18.50

Table 3.1: Operating conditions for case 125A and 132A

bubble density. In particular, in these calculations turbulence effects were considered using the Standard $k - \epsilon$ turbulence model. The numerical study have been concentrated on the simulations of some experiments (called 125A and 132A), performed by Hord [1], in a Ventury geometry (Fig.3.4). The operating conditions for the analyzed test cases have been shown in Tab.3.1 and the working fluid is hydrogen at two different temperatures. Several simulations have been performed to analyze the influence of the different modeling choices Tab.3.2. The grid is axial symmetric and has about 110000 cells. This grid is composed of a fine mesh close to the wall, in order to get an accurate description of the cavity formation and of the turbulence variables. The inlet and the outlet boundary conditions are set as pressure boundary condition, in particular the total and the static pressures have been set up at the inlet, and the static pressure as set at the outlet because the use of a pressure outlet boundary condition instead of an outflow condition results in a better rate of convergence when backflow occurs during iteration. The upper boundaries are no-slip walls.

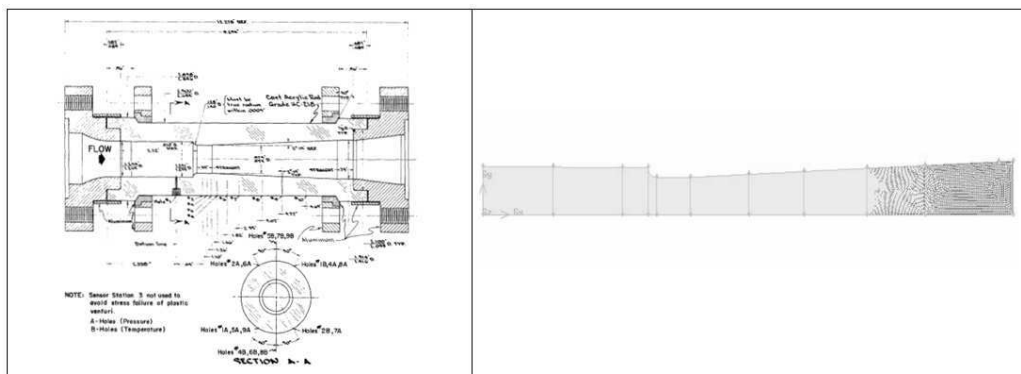


Figure 3.4: Ventury geometry

3.3. TEST CASES

SIMULATION	CAVITATION MODEL	NUCLEATION	ENERGY
1(125A)-15(132A)	ME	NO nucleation $\rightarrow n_b = 1 \times 10^{09}[1/m^3]$	NO energy equation
2(125A)-16(132A)	ME	YES \rightarrow Bubble transport equation(Eq.(3.26))	NO energy equation
3(125A)-17(132A)	ME	Eq.(3.26)	ENERGY
4(125A)-18(132A)	TE	NO nucleation $\rightarrow n_b = 1 \times 10^{09}[1/m^3]$	NO energy equation
5(125A)-19(132A)	TE	YES \rightarrow Bubble transport equation Eq.(3.26)	NO energy equation
9(125A)-20(132A)	SP ($C_e = 0.01; C_c = 0.02$)	NO nucleation $\rightarrow n_b = 1 \times 10^{09}[1/m^3]$	NO energy equation

Table 3.2: Simulations for the cases 125A and 132A

3.4 Results

Pressure profiles, obtained by means of numerical simulations, have been compared with experimental data [1]. As De Giorgi *et al.* [53] showed, the Singhal model [54], with the empirical coefficients validated for water fluid, gives an over-estimation of the vapor cavity length in the case of hydrogen flow. In [54], it has been supposed that this over-estimation could be due to the choice of the empirical coefficients. The two coefficients C_e and C_c of the Singhal model have been set to $C_e = 0.01$ and $C_c = 0.02$ after a preliminary sensitivity analysis. In Fig.3.5 the different cavitation models (mechanical equilibrium model, thermal equilibrium model and Singhal model) have been used to simulate the two test cases. The numerical results have been compared with the experimental data; the simulations have been performed without taking into account additional effects as thermal effects (energy equation) and nucleation (nuclei transport equation). It is clear that the mechanical equilibrium model seems to give better performances (Fig.3.5). The thermal equilibrium model (TE) neglects the energy requirements related to the vapor formation (enthalpy difference between liquid and vapor phase). The basic hypothesis of the model considers, as a limiting factor for the bubble growth, the mechanical energy necessary to displace the liquid in order to permit the growth of the bubble. The enthalpy transfer from the liquid to the vapor, necessary to provide the latent heat to the evaporating molecules, is not considered as a limiting factor for the vapor formation; the phase exchange depends only on the pressure difference between liquid and vapor in the surrounding of the bubble. For a given cavitation model it is interesting to see the influence of the nucleation and of the heat transfer near the vapor region. In Fig.3.6, previous results have been compared with the ones obtained considering the nucleation effects by implementing in the code the Eq.(3.26). The mechanical equilibrium model still gives the best accordance with experimental data, then the use of the transport nucleation equation improves the predictions. However there is an over-estimation of the minimum pressure in the cavitation region. For all these simulations the pressure correction equation has been used to limit the low pressure to the vapor pressure. Then, for these simulations, where the flow has been assumed as isothermal, the minimum pressure level is equal to the vapor pressure corresponding to the inlet flow temperature. However in cryogenic cavitation the thermal effects of cavitation become more pronounced than in conventional fluids, such as water at room temperature, that

3.5. CONCLUSIONS

typically disregard thermal effects, in particular at liquid temperature close to critical temperature. At these temperatures, evaporative cooling effects are pronounced, due also to the low ratio of liquid to vapor density, consequently more liquid mass should vaporize to sustain a cavity. The ME model is based on the thermal transport processes, where the bubbles growth is related to energy (enthalpy) transfer between the liquid and the vapor phases. It is assumed that the mechanical energy requirements do not limit the bubble growth. Therefore, for this model the implementation of the energy equation has a great impact on the vapor mass transfer rate. This is evident in Fig.3.7, where the mechanical equilibrium cavitation model ME has been used with three different approaches, without energy and nucleation effects (simulation1 and simulation15), with the nucleation transport equation and without energy equation (simulation2 and simulation16) and with both the nucleation transport equation and energy equation (simulation3 and simulation17). Results show that the performances of the ME model have been improved by considering both nucleation and thermal effects. Comparing the predicted cavity length in Fig.3.8, it is clear that the thermal equilibrium model (simulation19) and the Singhal model (simulation17), also based on a thermal equilibrium hypothesis, show a higher cavitation region than the ME model (simulation3 and simulation17). The temperature decrease in cryogenic vapor cavity (see Fig.3.9) reduces the extension of the cavitation and has also strong dependence on fluid thermodynamics properties that influence the cavitation phenomena (i.e. vapor pressure, density).

3.5 Conclusions

This part of the manuscript concerns the modeling of cavitating cryogenic flows, usually used in liquid rocket engine. The main objective has been to adapt the well-known cavitation models in order to study cryogenic flows. Numerical simulations of cavitation in liquid hydrogen in a Venturi geometry have been presented, representing a broader class of problems where the fluid is operating close to its critical temperature and thermal effects of cavitation and nucleation are important. A multiphase formulation accounting for the energy balance, variable thermodynamic properties of the fluid and nucleation transport equation, has been described. Several cavitation models have been compared. Then the importance of the nucleation modeling and of the thermal effects for the simulation of two phase flow cryogenic flows, has

3.5. CONCLUSIONS

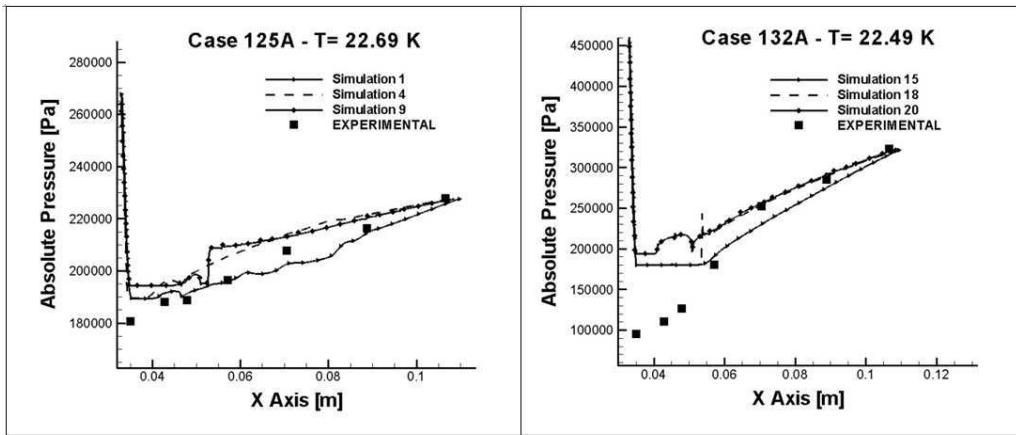


Figure 3.5: Comparison between pressure profiles of three cavitation model for the two test cases. Simulation 1 and simulation 15, ME mechanical equilibrium model. Simulation 4 and simulation 18, TE thermal equilibrium model. Simulation 9 and simulation 20, SP full cavitation model.

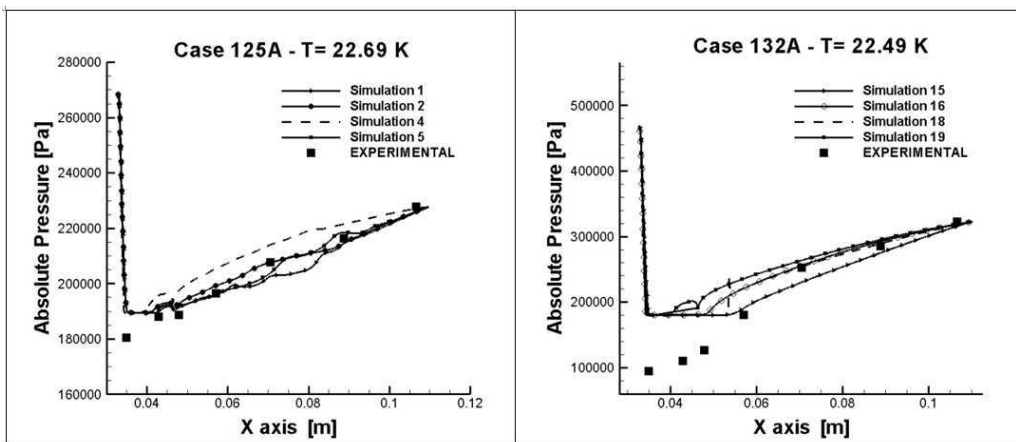


Figure 3.6: Comparison between pressure profiles obtained by using thermal equilibrium model (TE) and the mechanical equilibrium (ME) model with and without nucleation effects. Simulation 1 and 15, ME. Simulation 4 and 18, TE. Simulation 2 and 16, ME with nucleation. Simulation 5 and 19, TE with nucleation.

3.5. CONCLUSIONS

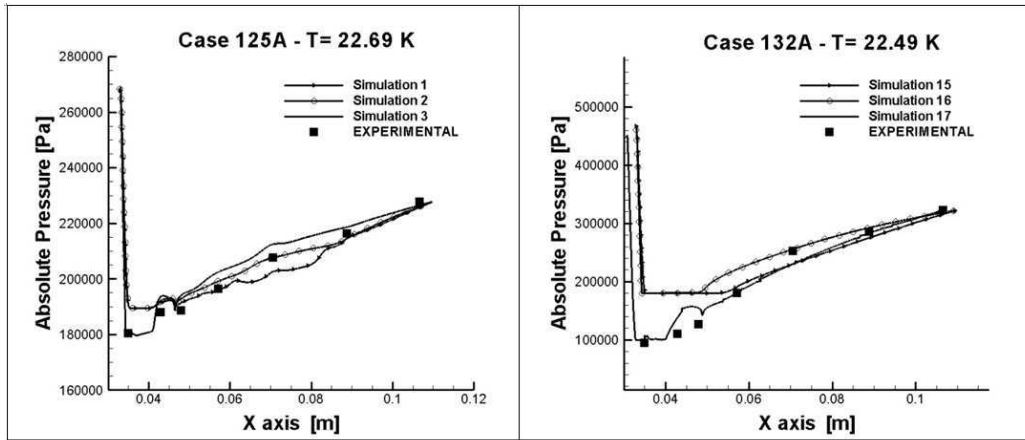


Figure 3.7: Comparison between pressure profiles obtained by using ME model for the two test cases with and without nucleation and energy effects. Simulation 1 and 15, ME. Simulation 2 and 16, ME with nucleation. Simulation 3 and 17, ME with nucleation and energy.

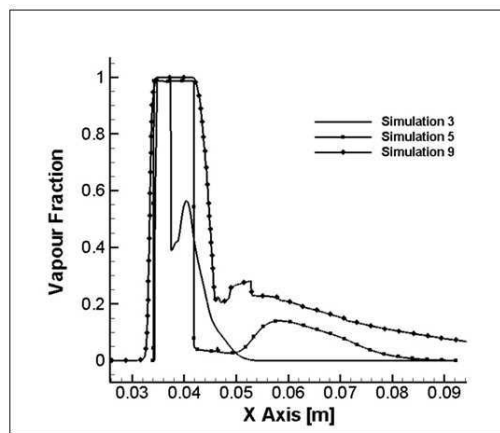


Figure 3.8: Comparison between vapor fraction profiles for the test case 125A. Simulation 3, ME with nucleation and energy. Simulation 5, TE with nucleation. Simulation 9, SP. Experimental cavity length equal to 0.0191 m [1].

3.5. CONCLUSIONS

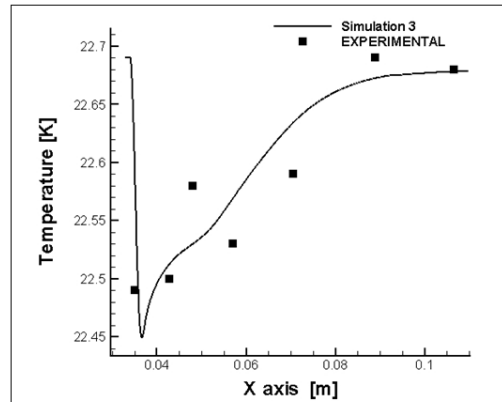


Figure 3.9: Comparison between numerical and experimental temperature profiles for the test case 125A. Simulation 3, ME whit nucleation and energy.

been assessed. Results show the importance of the choice of the cavitation model for the performance of the numerical simulations, in particular the best predictions have been given by the mechanical equilibrium cavitation model, based on the thermal transport processes, where the bubbles growth is related to energy (enthalpy) transfer between the liquid and the vapor phases. Performances of the ME model have been improved by considering both nucleation and thermal effects.

Chapter 4

Bubble Dynamics and Water Treatment with Cavitation

4.1 Introduction

To understand the physical mechanism of the bubble collapse, the numerical simulation of the acoustic cavitation has been performed and will be presented in this section. Let us suppose that a bubble (non-condensable gas + vapor), that is in an initial thermodynamic equilibrium in the water, is subjected to an oscillating pressure, that induces its growth (if the pressure is positive) or its collapse (when the pressure is negative). This work has been divided in two parts:

- Study of Rayleigh-Plesset (RP) equation
 - Discretization and numerical scheme
 - Influence of the equation of state (EOS) on bubble behavior
 - Compressible effect.
- Study of the production of hydroxyl radicals due to dissociation of water molecules present in the bubble, during the collapse

A Rayleigh-Plesset equation and three slightly modified equations (RP1, RP2, RP3) in order to consider the liquid compressible effects, have been implemented and solved by using in an in-house code (C language). Results have been compared with the numerical and experimental data of Yuan *et*

4.2. RAYLEIGH-PLESSET EQUATION

al. [4] and Lofstedt [3]. For the modeling of the gas in the bubble, two EOS has been used:

- Perfect gas equation
- Van der Waals equation

The evolution of bubble radius allows giving a first estimation of bubble temperature. In the following paragraphs, numerical details will be given. In the last paragraph, the production of radicals has been computed.

4.2 Rayleigh-Plesset Equation

4.2.1 Classical Rayleigh-Plesset Equation

The Rayleigh-Plesset equation describes the behavior of a bubble with an initial radius R_0 that is in equilibrium with the liquid phase and it is subjected to a known variation of pressure. Considering the Navier Stokes equation for the liquid phase (see Appendix A) and by making the hypothesis of zero viscosity and irrotational field, a potential solution can be obtained (see for more details Appendix A):

$$\phi = \phi_\infty - \frac{1}{r}F(t - r/c) \approx \phi_\infty - \frac{1}{r}F(t) + \frac{\dot{F}(t)}{c}, \quad (4.1)$$

where $F(t)$ is $F(t) = R^2 \frac{\partial R}{\partial t} = R^2 \dot{R}$, ϕ_∞ is the potential law of the bubble (non-perturbed liquid field), c is the speed of sound. Supposing a negligible radiation effect induced by the bubble (then the liquid is incompressible), the classical equation of Rayleigh-Plesset is defined as (see Appendix A):

$$\rho \left[R\ddot{R} + \frac{3}{2}\dot{R}^2 \right] = P_g - P_0 - P_{ext}(t) - \frac{2\sigma}{R} - \frac{4\mu\dot{R}}{R}. \quad (4.2)$$

4.2.2 Rayleigh-Plesset Equation with Compressible Term

If the liquid should be considered compressible, by replacing the Eq.(4.1) in the Navier-Stokes equation (see Appendix B) it is possible to obtain different versions of RP. The first equation is named RP1 and it has been obtained by Rayleigh, Plesset, Noltingk et Protsky and then modified by Keller et Kolodner[57]:

4.3. BUBBLE COLLAPSE PHENOMENON

$$R\ddot{R} + \frac{3}{2}\dot{R}^2 = \frac{1}{\rho_{l\infty}} \left(P_g(R, t) - P_0 - P_{ext}(t) - \frac{2\sigma}{R} - \frac{4\mu\dot{R}}{R} \right) + \frac{t_R}{\rho_{l\infty}} \frac{d}{dt} [P_g(R, t) - P_{ext}(t)] \quad (4.3)$$

where $t_R = R/c_{l\infty}$, $c_{l\infty}$ is the speed of sound at room condition. The second equation, RP2, comes from the formulation of Keller-Miksis [58]:

$$(1-M)R\ddot{R} + \frac{3}{2} \left(1 - \frac{M}{3} \right) \dot{R}^2 = \frac{1}{\rho_{l\infty}} (1+M) [P(R(t)) - P_0 - P_{ext}(t+t_R)] + \frac{t_R}{\rho_{l\infty}} \frac{dP(R(t))}{dt} \quad (4.4)$$

where $M = \dot{R}/c_{l\infty}$. The equation RP3 [28] is :

$$(1-M)R\ddot{R} + \frac{3}{2} \left(1 - \frac{M}{3} \right) \dot{R}^2 = (1+M) \left[H_b - \frac{1}{\rho_l} P(t+t_R) \right] + t_R \frac{dH_b}{dt}, \quad (4.5)$$

where ρ_l, H_b are, respectively, the density and the enthalpy of liquid phase defined by Tait law (See Appendix B).

4.3 Bubble Collapse Phenomenon

When the bubble collapses, the gas in the bubble is compressed. The temperature in the bubble increases compared to liquid around and, from the bubble to the liquid phase, a thermal flow develops, making cold the bubble. A temperature gradient due to thermal flux appears from the interface in the two phases. Conversely, if the thermal effect in the liquid phase is neglected, the temperature at the interface is supposed to be the liquid temperature far from the bubble T_∞ . For the mass diffusion and particularly for vapor formation, a similar mechanism develops. Considering the perfect gas equation:

$$p_v V = \frac{m_v}{M_v} RT \quad (4.6)$$

it is possible to obtain the vapor mass concentration in the mixture of the bubble:

$$C = \frac{m_v}{m_v + m_g} = \frac{p_v M_v}{p_v M_v + p_g M_g}, \quad (4.7)$$

where p_v and p_g are, respectively, the pressure partial of vapor and gas, M_v M_g are the molecular mass of vapor and gas. At the interface, the vapor partial pressure is equal to vapor pressure of saturation corresponding to interface temperature $p_v(T_i)$. At the initial instant when the radius bubble is greatest and the implosion phase starts, the pressure of water vapor is supposed uniform in the bubble and equal to $p_v(T_i)$. The gas mass in the bubble is supposed as a constant. If the vapor mass is constant (in absence of condensation) the Eq.(4.7) shows that the concentration of vapor remains constant during the bubble implosion. However the concentration of vapor at the interface tends to decrease, because the non-condensable gas pressure p_g increase due to volume reduction:

$$C = \frac{p_v(T_i)M_v}{p_v(T_i)M_v + p_g M_g}. \quad (4.8)$$

If the vapor diffusion through the non-condensable gas develops without resistance, the vapor spreads every moment until the pressure becomes uniform in the bubble at the value $p_v(T_i)$. In the thermal diffusion, the temperature at the interface can be considered constant until the bubble temperature increases due to compression. On the contrary, in the case of mass diffusion, the mass concentration of vapor is constant at the center of the bubble (the two partial pressure increase together), but it decreases at the interface because the partial pressure is computed on the base of thermodynamic equilibrium. It remains constant while the gas partial pressure tends to increase due to decrease of the volume. In these conditions, it is assumed that the behaviors of water vapor and non-condensable gas in the bubble are similar, because the characteristic implosion time is shorter than diffusion time during the collapse phase.

4.4 Rayleigh-Plesset Equation Discretization

Two Runge-Kutta methods have been used for the temporal discretization of RP equation:

- An adaptive step size Runge-Kutta method proposed by Fehlberg [59]. It is a four-stage scheme, but it computes the error with a five-stage scheme.
- A three-stage Runge-Kutta with TVD (Total Variation Diminishing) scheme [60].

The two methods have been compared in terms of cost of simulation with a classical Rayleigh-Plesset Eq.(4.2). In the following paragraph, the two methods have been described. Then, the results obtained with the two methods, simulating the test-case of Yuan [4], have been shown. Simulations reproduce the temporal evolution of a bubble at initial thermodynamic equilibrium with the liquid phase. The bubble has an initial radius R_0 and it is subject to an oscillating pressure. The operating condition are summarized in Tab.4.1.

4.4.1 The Runge-Kutta Fehlberg method

This method is based on an adaptive temporal step size. In each iteration, the solution of two different approximations is computed, the first of four-stage scheme and the second of five-stage scheme. If the difference between the two solutions, is higher than tolerance value, the temporal step size h is reduced, by multiplying it with a coefficient that is proportional to the tolerance and to the error. The solution of four-stage scheme is :

$$y_{j+1} = y_j + \frac{25}{216}k_1 + \frac{1408}{2565}k_3 + \frac{2197}{4104}k_4 - \frac{1}{5}k_5. \quad (4.9)$$

The solution of five-stage scheme is:

$$z_{j+1} = z_j + \frac{16}{135}k_1 + \frac{6656}{12825}k_3 + \frac{28561}{56430}k_4 - \frac{2}{55}k_5. \quad (4.10)$$

4.4. RAYLEIGH-PLESSET EQUATION DISCRETIZATION

For each iteration the following coefficients have been computed [59]:

$$\left(\begin{array}{l} k_1 = hf(t_j, y_j) \\ k_2 = hf\left(t_j + \frac{1}{4}h, y_j + \frac{1}{4}k_1\right) \\ k_3 = hf\left(t_j + \frac{3}{8}h, y_j + \frac{3}{32}k_1 + \frac{9}{32}k_2\right) \\ k_4 = hf\left(t_j + \frac{12}{13}h, y_j + \frac{1932}{2197}k_1 - \frac{7200}{2197}k_2 + \frac{7296}{2197}k_3\right) \\ k_5 = hf\left(t_j + h, y_j + \frac{439}{216}k_1 - 8k_2 + \frac{3680}{513}k_3 - \frac{845}{4104}k_4\right) \\ k_6 = hf\left(t_j + \frac{1}{2}h, y_j - \frac{8}{27}k_1 + 2k_2 - \frac{3544}{2565}k_3 + \frac{1859}{4104}k_4 - \frac{11}{40}k_5\right) \end{array} \right)$$

The method is called "adaptive", because, if the absolute difference between the two solutions is more elevated than the tolerance, the solution at four stage is not accepted and the step size h is reduced. The next step size is calculated multiplying h by s :

$$s = \left(\frac{\epsilon h}{2|z_{j+1} - y_{j+1}|} \right)^{1/4} = 0.840896 \left(\frac{\epsilon h}{|z_{j+1} - y_{j+1}|} \right)^{1/4}, \quad (4.11)$$

where ϵ is the tolerance. The Rayleigh-Plesset is an equation of 2^{th} order that can be simplified in two differential equations of 1^{th} order:

$$\begin{aligned} f_1 &= \frac{dR}{dt} = \dot{R} \\ \{ f_2 &= -\frac{3}{2} \frac{\dot{R}^2}{R} + \frac{1}{\rho R} \left[P_g - P_0 - P_{ext} - \frac{2S}{R} - \frac{4\mu\dot{R}}{R} \right] + \text{Compressible term.} \end{aligned}$$

To obtain the radius evolution, it is necessary to apply the R-K method to the two functions f_1 and f_2 :

$$\begin{aligned} y_1 &= R \\ \{ y_2 &= \frac{dR}{dt} \end{aligned}$$

In the numerical code, the tolerance for the function y_2 is equal to $\epsilon = 0.05$. The function z and also the error have been estimated for function y_2 .

4.4. RAYLEIGH-PLESSET EQUATION DISCRETIZATION

The first step size has been fixed to $h = 1 \times 10^{-09} \text{sec}$ and it is used during the iterations in which the error is lower than tolerance. If the error exceeds the tolerance, the time step is decreased. The time step cannot be higher than $h = 1 \times 10^{-09} \text{sec}$, but it can be very short by increasing the computational cost of the simulation.

4.4.2 The Runge-Kutta method with TVD

The general form of Runge-Kutta method is:

$$u^i = \sum_{k=0}^{i-1} (\alpha_{ik} u^k + \Delta t \beta_{ik} L(u^k)) \quad i = 1, \dots, m$$
$$u^0 = u^n$$
$$u^m = u^{n+1}$$

where, Δt must respect the *TVD* properties:

$$\Delta t \leq c \Delta t_1 \quad (4.12)$$

where c is the coefficient *CFL* defined as :

$$c = \min_{i,k} = \frac{\alpha_{ik}}{|\beta_{ik}|} \quad (4.13)$$

The RK TVD proposed by Gottlieb et Shu [60] has been used :

$$u^1 = u^n + \Delta t L(u^{(1)})$$
$$u^2 = \frac{3}{4} u^n + \frac{1}{4} u^1 + \frac{1}{4} \Delta t L(u^{(1)})$$
$$u^{n+1} = \frac{1}{3} u^n + \frac{2}{3} u^2 + \frac{2}{3} \Delta t L(u^{(2)})$$

As for RK-Fehlberg, this method is applied to bubble radius and its derivative. On the contrary, the time step size is not adaptive, but it is the minimum value between $1 \times 10^{-09} \text{sec}$ and the characteristic times obtained

4.4. RAYLEIGH-PLESSET EQUATION DISCRETIZATION

by dimensionless form of Rayleigh-Plesset equation:

$$\begin{aligned}
 T &= \frac{R_0^2}{4\nu} \\
 T^2 &= \frac{4\nu T}{2\sigma} \\
 T^2 &= \frac{\rho_l R_0^2}{P_0} \\
 T_{compressible} &= \frac{\rho_l c_{l\infty} R}{3\gamma P_{g0}} R \left(\frac{R}{R_0} \right)^{3\gamma}
 \end{aligned}$$

where $T_{(compressible)}$ is the time obtained for the compressible term. The optimal time step size is chosen with the following steps: 1) a CFL is chosen, 2) some simulations are performed, 3) if the code presents a problem of robustness, CFL is reduced and loop restarts from step 2).

4.4.3 Comparison of Two Discretization Methods

The two previous methods have been compared, reproducing the test cases presented by Yuan [4]. The operating condition are summarized in Tab.4.1. In Fig.4.1, the temporal variation of radius have been presented. The profiles are very similar, but when $t > 26\mu s$, the four-stage RK method gives a maximal radius higher than RK TVD (see Fig.4.2). A maximal difference of 2.77% corresponding to $t = 37\mu s$ have been obtained. On the contrary, the collapse times and the minimum value of bubble radius, obtained with the two methods, are equal (see Fig.4.4). Only a difference of 0.8% have been determined in the last collapse. The bubble temperature have been presented in Fig.4.3. The results of the two methods are comparable and they present a maximal difference of 4.3% after $t = 30\mu s$. Finally, these conclusions should be done:

- The Runge-Kutta Fehlberg method has an higher accuracy order, but also an higher computational cost (3 hours on a Linux 64bit, 2GB ram).
- Results obtained with the two methods are nearly the same (The maximum difference is of 4.3% on the temperature), but the RK TVD has a computational cost of 1 minute (Linux 64bit, 2GB ram).

The three-stage Runge Kutta TVD method has been chosen for all the following simulations.

4.4. RAYLEIGH-PLESSET EQUATION DISCRETIZATION

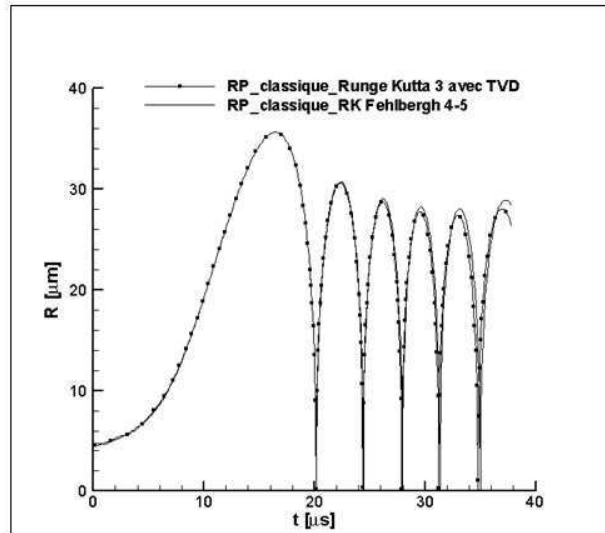


Figure 4.1: Comparison of temporal bubble radius profiles, obtained by the resolution of classical RP (Eq.(4.2)), using three stage Runge-Kutta TVD and four stage Runge-Kutta Fehlbergh 4-5. Bubble at a constant temperature during growth phase ($\gamma = 1$). Adiabatic compression if the bubble radius lower than R_0 .

4.4. RAYLEIGH-PLESSET EQUATION DISCRETIZATION

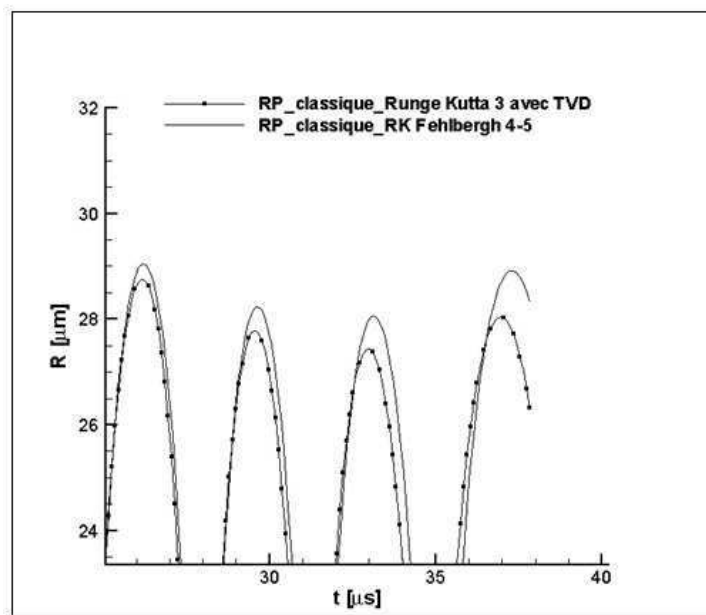


Figure 4.2: Zoom of last four rebounds of Fig.4.1

4.4. RAYLEIGH-PLESSET EQUATION DISCRETIZATION

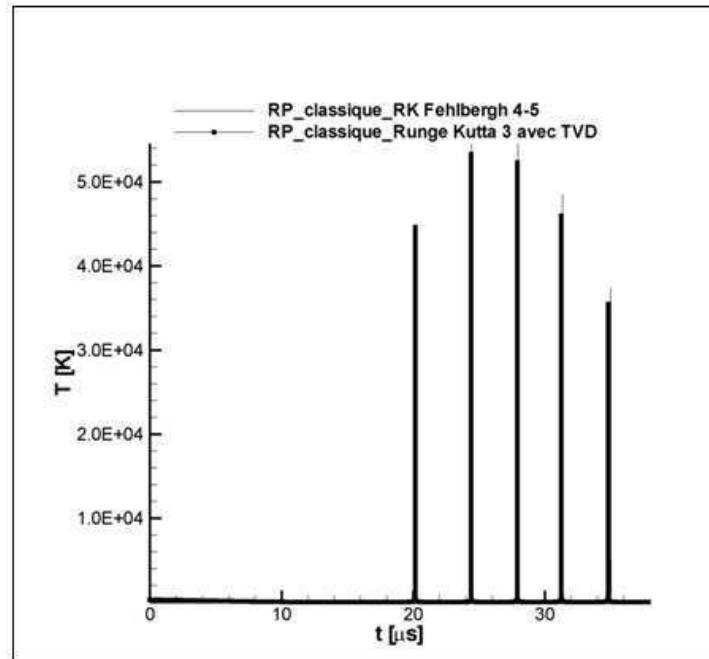


Figure 4.3: Comparison of temporal temperature variation, obtained by the resolution of classical RP (Eq.(4.2)), using three stage Runge-Kutta TVD and four stage Runge-Kutta Fehlbergh 4-5. Bubble at a constant temperature during growth phase ($\gamma = 1$). Adiabatic compression if the bubble radius lower than R_0 .

4.4. RAYLEIGH-PLESSET EQUATION DISCRETIZATION

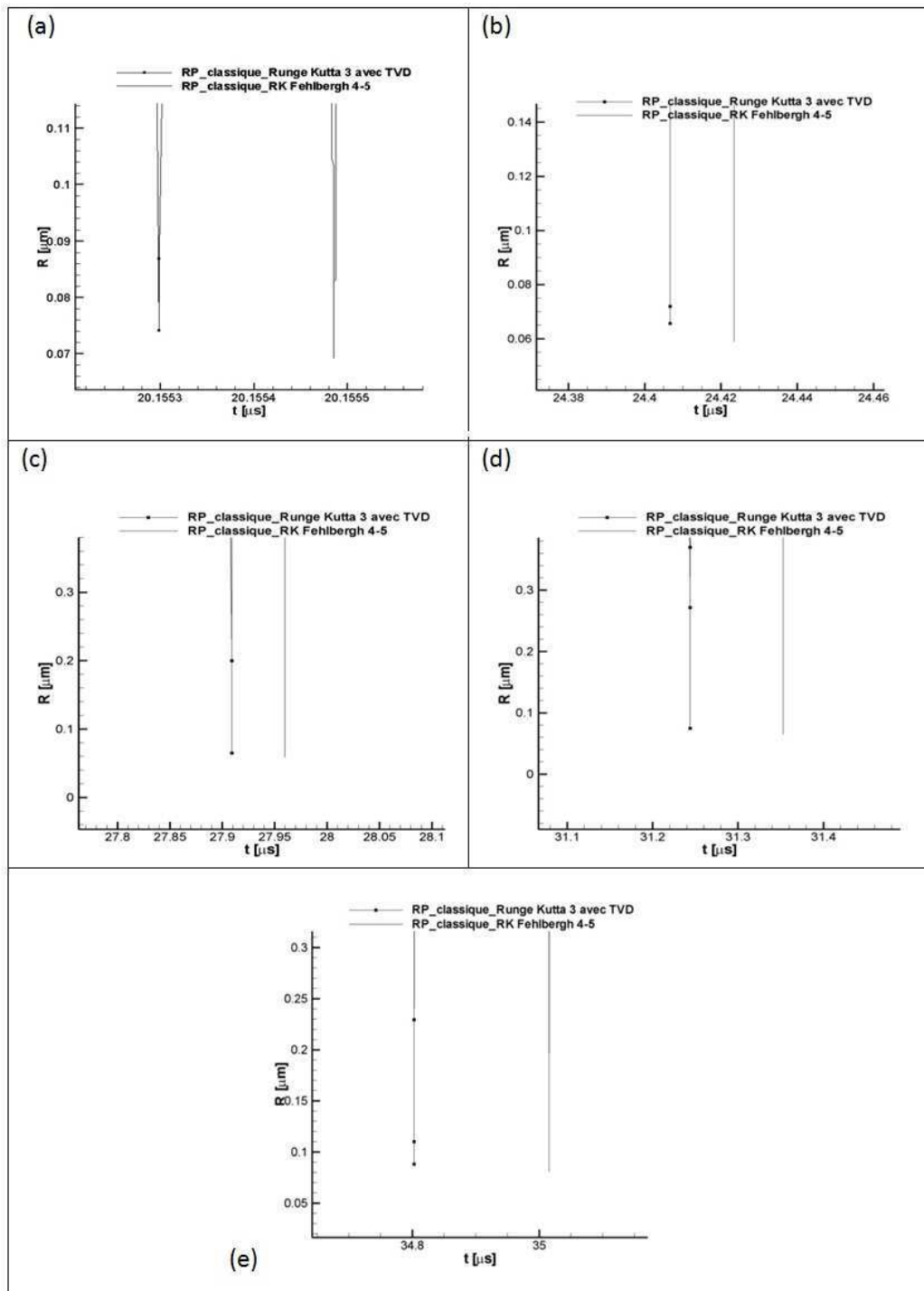


Figure 4.4: Zoom of last five collapses of Fig.4.1

4.5 Results

4.5.1 Validation

In the numerical code, the classical Rayleigh-Plesset equation and RP1, RP2 and RP3 equations (see respectively Eq.(4.2), Eq.(4.3), Eq.(4.4) and Eq.(4.5)) have been implemented. The validation of in-house code has been done by reproducing the test case of Leighton [2] obtained with the classical Rayleigh-Plesset equation and the test case of Lofstedt *et al.* [3] with RP1, RP2, RP3 equations. In the first case, the air bubble is supposed in thermodynamic equilibrium with the liquid phase and it is subject to an oscillation pressure $P_{ext} = P_a \sin(\varpi t)$. The gas in the bubble is subject to an adiabatic transformation. The operating conditions are summarized in Tab.4.1. The numerical results of Leighton [2] have been compared with the results obtained with the in-house code (Fig.4.5). There is a good accord between the profiles of the bubble radius, the derivative of radius (or interface velocity), the bubble pressure and the internal temperature. For the validation of the other RP equations (RP1, RP2 and RP3), the test case of Lofstedt *et al.* [3] has been used. In this test case, the simulation of a bubble in equilibrium subject to an oscillating pressure have been considered. The initial conditions are summarized in Tab.4.1. In this case, experimental data and the numerical results obtained by Lofstedt *et al.* [3] (obtained by resolving a Rayleigh-Plesset equation modified to consider the compressible effects), are available:

$$(1 - 2M)R\ddot{R} + \frac{3}{2} \left(1 - \frac{4M}{3}\right) \dot{R}^2 = \frac{1}{\rho_l} [P(R(t)) - P_0 - P_{ext}(R=0, t)] + t_R \frac{d[R(t)] - P_{ext}(R, t)}{dt} \quad (4.14)$$

where M is the Mach number defined as $M \equiv \dot{R}/c_{l\infty}$, the function $P(R(t))$ is defined by Eq.(A.10) of Appendix A, P_0 is the equilibrium pressure at the instant $t = 0$, P_{ext} is the solicitation pressure of bubble. It can be observed a good accordance between bubble radius profiles obtained by the in-house code with the three equations and the experimental and numerical results of Lofstedt *et al.* [3]. More evident differences can be observed in $23\mu s < t < 33\mu s$, where a higher bubble growth than experimental and numerical results of Lofstedt is obtained. However, the maximum error is low and equal to 2.55%. The first time collapse is well estimated with all equa-

4.5. RESULTS

Test Case	P_0 (atm)	T_0 (K)	R_0 (μm)	$\frac{\varpi}{(2\pi)}$ [kHz]	σ [kg/s ²]	ρ [kg/m ³]	μ [kg/(m·s)]	P_a [atm]	$c_{l\infty}$ [m/s]	$\frac{R_0}{b}$
<i>Yuan</i>	1	300	4.5	26.4	0.0725	1000	0.001	1.275	1481	8.54
<i>Lofstedt</i>	1	300	4.5	26.5	0.03	1000	0.003	1.35	1481	8.54
<i>Leighton</i>	1	293.5	2000	10.0	0.0727	1000	0.001	2.665	-	-

Table 4.1: Test-Case of Validation

tions Fig.4.6, but the critical radius of bubble estimated with in-house code are not much lower than experimental value (Fig.4.7). Observing the difference between profiles obtained with RP1, RP2 et RP3 (Fig. 4.7), RP1 gives best prediction of experimental data. The critical radius of first collapse, obtained with RP1, has been compared with the other numerical profiles (Fig.(4.7)). It is evident that at the collapse, derivatives $dR/dt = 0$, because in the point of minimum radius, the tangent is parallel to x axis (Fig.(4.7)). However the minimal value and the profiles shapes are different.

4.5.2 Influence of Equation of State

In this work, the bubble of gas in equation RP1, RP2 and RP3 (see respectively Eq.(4.3), Eq.(4.4) and Eq.(4.5) is governed by:

- Van der Waals (VDW)
- Perfect gas (PFG).

In a first analysis the equation of state Van der Waals should be more appropriated because when the fluid conditions are closed to saturation curve, the hypothesis of perfect gas is not verified. However the results obtained with two approaches have been compared for each equation RP1, RP2 and RP3 simulating the test-case of Yuan *et al.* [4]. The two thermodynamic approaches give similar results (see Fig.(4.9-a), Fig.(4.10-a) and Fig.(4.11-a)). The radius have almost the same profiles, the maximal values of radius obtained with PFG is higher than values obtained with VDW (see Fig.(4.9-b), Fig.(4.10-b) and Fig.(4.11-b)), but the difference is lower than 1%. On the contrary, the two approaches give different predictions for the minimal radius during the first collapse and in the temperature estimation. In all the

4.5. RESULTS

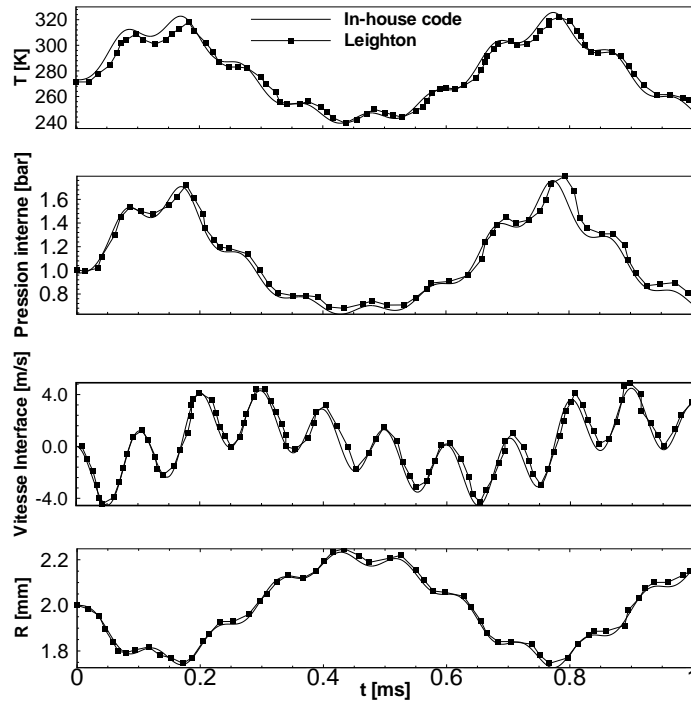


Figure 4.5: Behavior of an air bubble with initial radius $R_0 = 2mm$ in the water at standard condition ($T = 20C; P_0 = 1atm$). Pressure wave with frequency $f = 10kHz$ and amplitude $P_a = 2.7bar$. Comparison between the profiles obtained by Leighton [2] and by in-house code, solving a classical RP equation

4.5. RESULTS

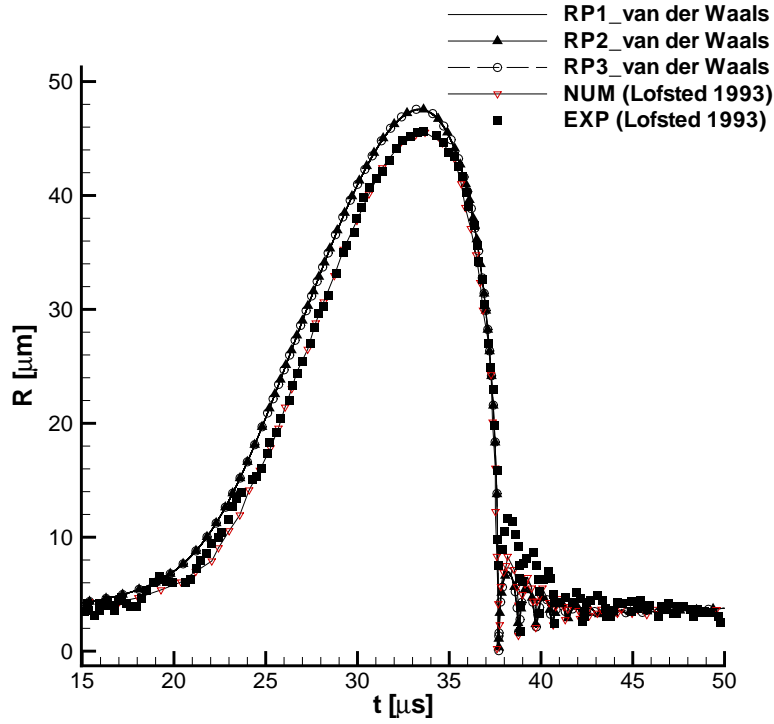


Figure 4.6: Comparison of temporal radius evolution obtained with the in-house code (RP1, RP2 and RP3) and numerical and experimental profiles. In this case $R_0 = 4.5\mu m$, $f = 26.5kHz$, $\sigma = 0.03kg/s^2$, $c_{l\infty} = 1481m/s$, $\mu = 0.003kg/m$ and $Pa = 1.35atm$. The bubble is supposed at constant temperature ($\gamma = 1$) and the properties are uniform in the bubble.

4.5. RESULTS

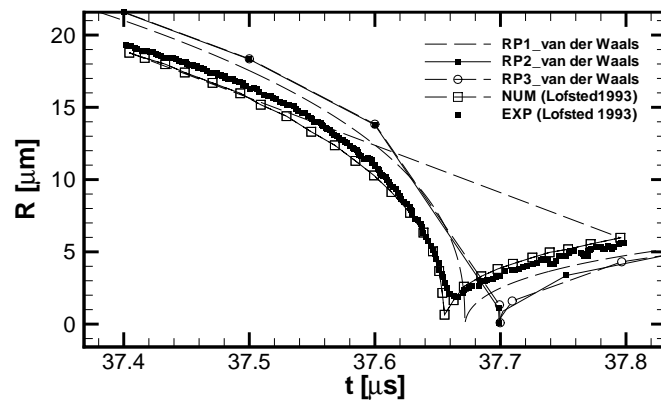


Figure 4.7: Zoom of first collapse of Fig.(4.6). Comparison of profiles obtained by RP1, RP2 and RP3 and by Lofstedt [3] with Eq.(4.14)

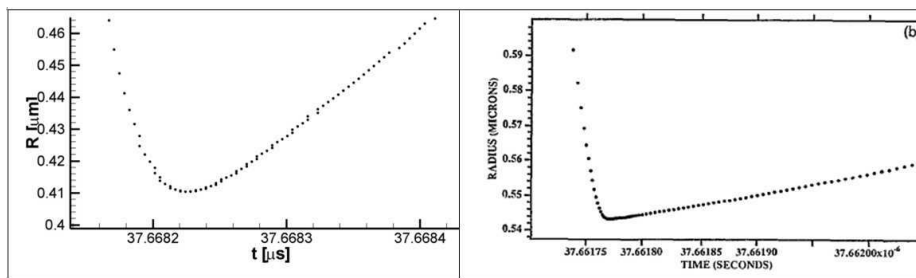


Figure 4.8: a) Zoom of first collapse of Fig.4.6. b) Comparison of profiles obtained by RP1 and by Lofstedt [3] with Eq.(4.14)

4.5. RESULTS

simulations (see Fig.(4.9-c), Fig.(4.10-c) and Fig.(4.11-c)) the estimation of critical radius is different. When PFG is used, the minimal radius is lower than the value estimated with VDW. This difference has a strong influence on the temperature estimation that shows a difference of $10^3 K$ between the solutions obtained with the two EOS. The most elevated temperature is obtained with RP3 ((see Fig.(4.9-d), Fig.(4.10-d) and Fig.(4.11-d))).

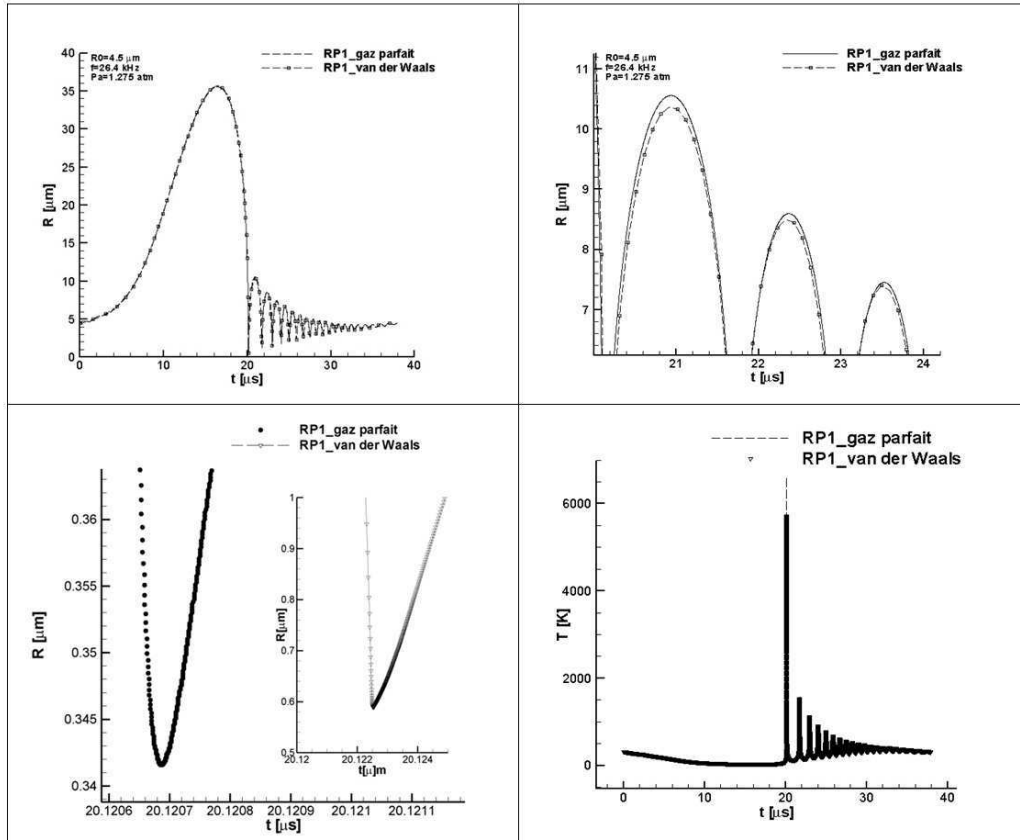


Figure 4.9: (a) Comparison of radius profiles obtained by RP1 with the hypothesis of PFG and VDW EOS. (b) Zoom of 2th, 3th and 4th maximum radius. (c) Zoom of first collapse of (a). (d) Temperature profiles.

4.5. RESULTS

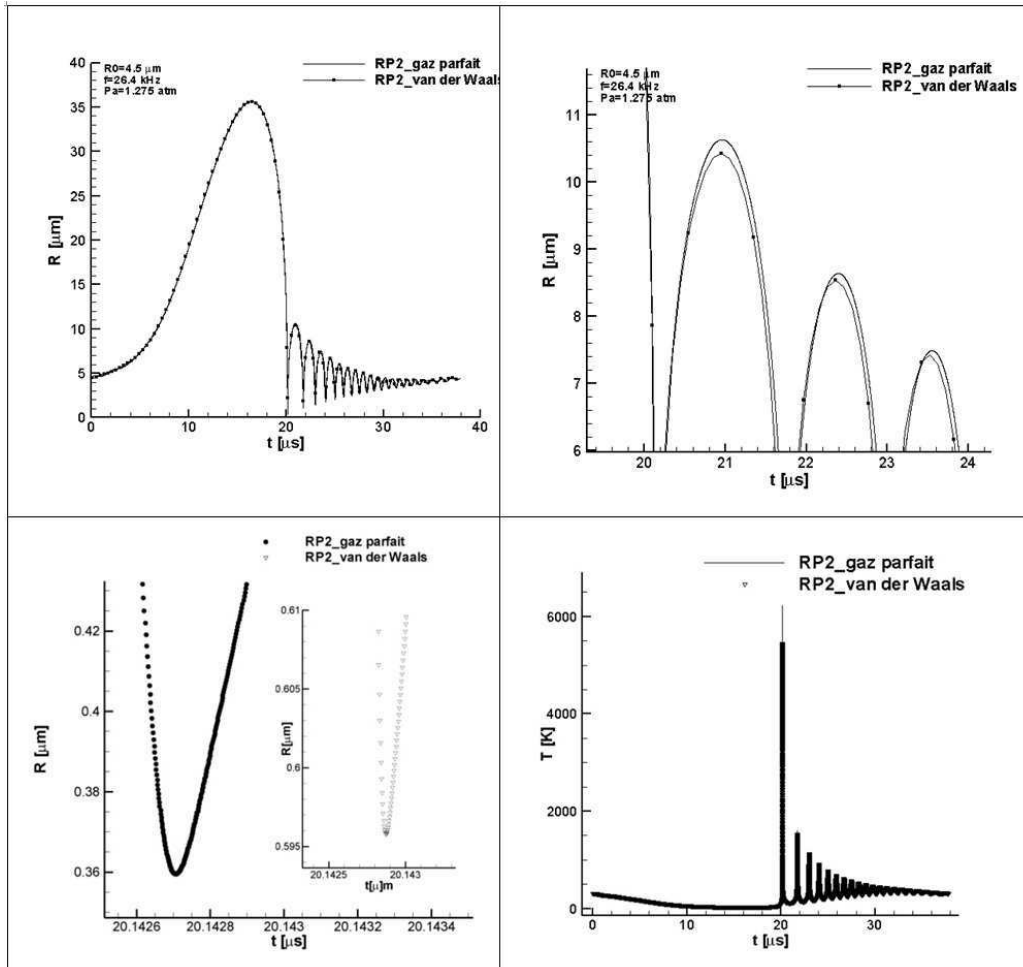


Figure 4.10: (a) Comparison of radius profiles obtained by RP2 with the hypothesis of PFG and VDW EOS. (b) Zoom of 2th, 3th and 4th maximum radius. (c) Zoom of first collapse of (a). (d) Temperature profiles.

4.5. RESULTS

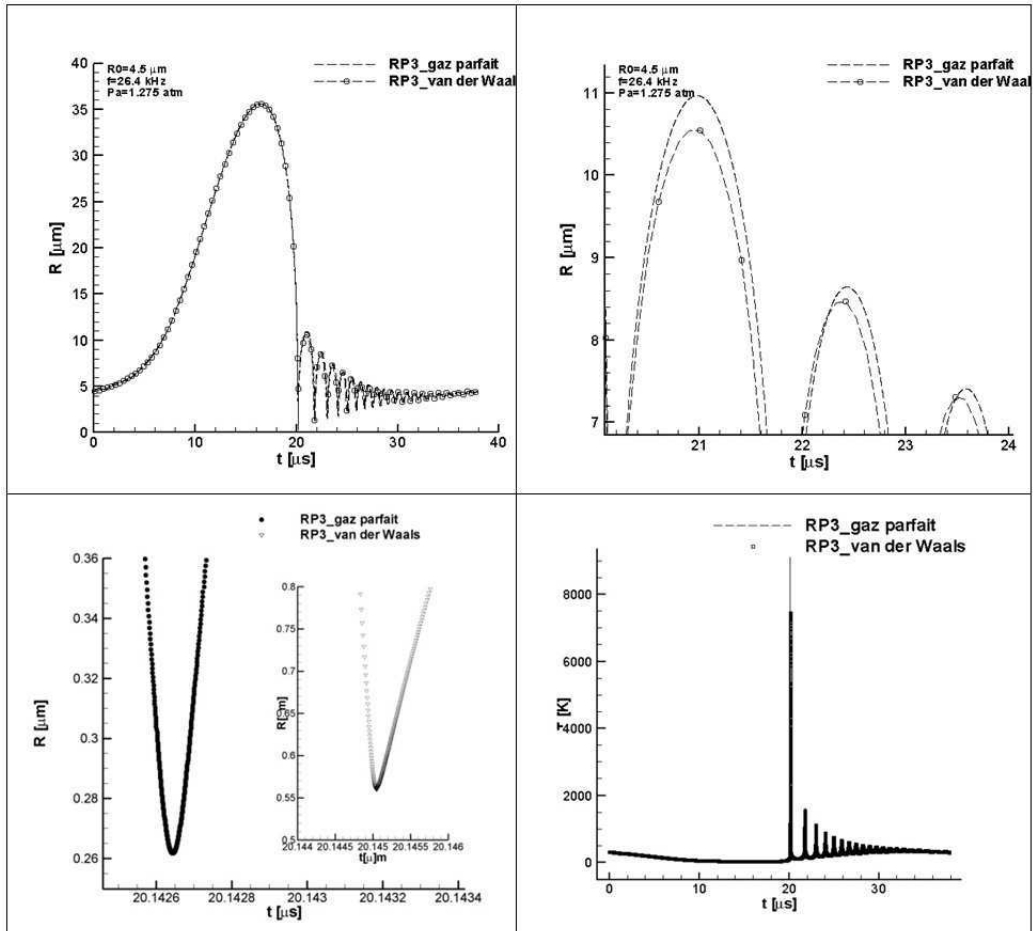


Figure 4.11: (a) Comparison of radius profiles obtained by RP3 with the hypothesis of PFG and VDW EOS. (b) Zoom of 2th, 3th and 4th maximum radius. (c) Zoom of first collapse of (a). (d) Temperature profiles.

4.5.3 Compressible Effect Evaluation

As explained before (see Appendix A for more details), the compressible effect has been taken into account. The classical Rayleigh-Plesset equations and the others (RP1, RP2 et RP3) are different because of a different estimation of compressible term $\frac{\rho}{c} \frac{d^2}{dt^2}(R^2 \dot{R})$. In this part of work, the influence of compressible effect on evaluation of bubble behavior has been considered. At our knowledge, in literature there are not comparisons between classical Rayleigh-Plesset and a version in which the compressible effect is considered. The test cases, chosen for this comparison (Yuan [4] and Lofstedt [3]), present important compressible effects, because the estimated minimal radius is very low, closed to zero. In test case of Yuan [4], the gas transformation is supposed as isothermal when the bubble radius is higher than the initial radius R_0 , while it is supposed adiabatic when $R < R_0$. On the contrary, in the test case of Lofstedt [3], the gas transformation is always supposed as isothermal ($\gamma = 1$). It is evident, in both test cases, that the compressible effects influence the frequency of rebounds (Fig.(4.12)), Fig.(4.11-d)). In fact, comparing the collapse times, results obtained without compressible effect are nearly three times more elevated than the collapse time obtained with the equation considering the compressible effect. This consideration does not concern the first collapse that is not influenced by compressible effect.

4.5.4 Radicals estimation

During collapse phase, the volume of bubble decreases and then an increase of temperature is induced. This effect allows the water dissociation in the bubble, in the form of vapor. The water develops radicals that are hydroxyl radicals OH, following the equation $H_2O \rightleftharpoons H + OH$. Yasui [30] gave the formula to compute speed of dissociation reaction and association for the reaction:

$$v_r = \frac{d[H_2O]}{dt} = -\frac{d[H]}{dt} = \frac{d[OH]}{dt} = A_r T^{B_r} e^{-\frac{C_r}{T}} [H][OH], \quad (4.15)$$

$$v_d = \frac{d[H]}{dt} = \frac{d[OH]}{dt} = \frac{d[OH]}{dt} = A_d T^{B_d} e^{-\frac{C_d}{T}} [H_2O], \quad (4.16)$$

where r and d indicate, respectively, the association and the dissociation phase. The constant value are indicated in [30]:

4.5. RESULTS

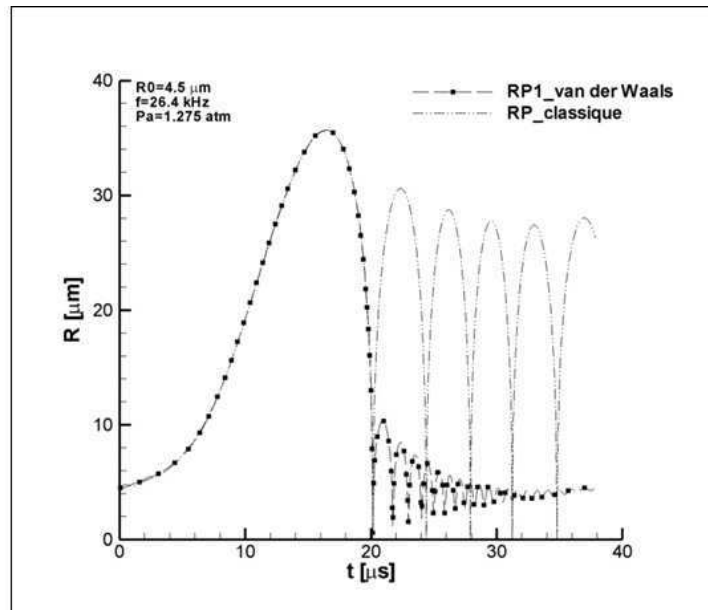


Figure 4.12: Comparison between radius evolution profiles obtained by classical RP and by RP1 (with liquid compressible effect) in the case described by Yuan [4]

4.5. RESULTS

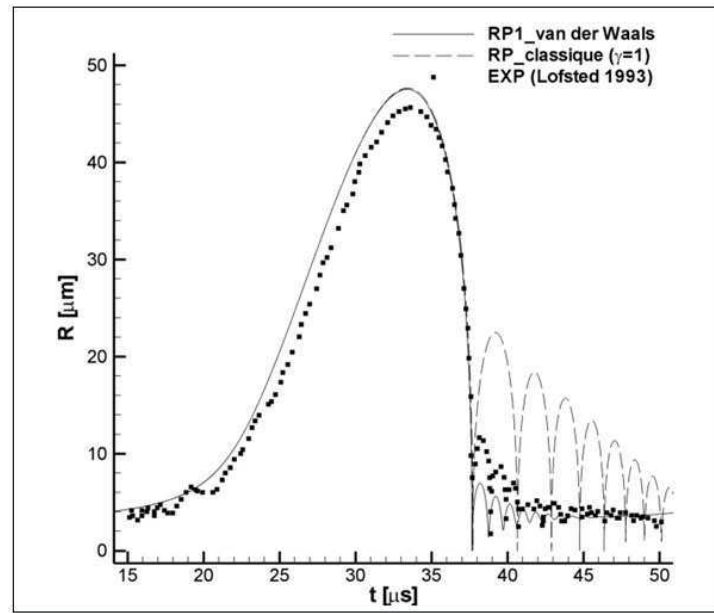


Figure 4.13: Comparison between radius evolution profiles obtained by classic RP and by RP1 (with liquid compressible effect) in the case described by Lofstedt [3]

4.5. RESULTS

$$\begin{aligned} & A_r = 2.25 \times 10^{10} \text{ m}^3 \text{ mol}^{-1} \text{ s}^{-1} \\ \{ & \quad \beta_r = -2 \\ & \quad C_r = 0 \\ & A_d = 1.96 \times 10^{16} \text{ m}^3 \text{ mol}^{-1} \text{ s}^{-1} \\ \{ & \quad \beta_d = -1.62 \\ & \quad C_d = 59700 \text{ K} \end{aligned}$$

It is possible to suppose a thermodynamic equilibrium, because the chemical reaction times are several orders of magnitude lower than collapse times. At the equilibrium, the two phases are the same:

$$\frac{[H][OH]}{[H_2O]} = \frac{k_d}{k_r} = \frac{A_d}{A_r} T^{\beta_d - \beta_r} e^{\frac{C_d - C_r}{T}} = K(T). \quad (4.17)$$

This allows obtaining the equilibrium constant $K(T)$, that is exclusively function of temperature. Replacing the Eq.(4.5.4) in Eq.(4.17) :

$$K(T) = 8.711 \times 10^5 T^{0.38} e^{-\frac{59700}{T}}. \quad (4.18)$$

The Eq.(4.17) allows estimating the OH or H radical concentration as a function of temperature:

$$n_{OH} = \sqrt{K(T)n_{H_2O}V}, \quad (4.19)$$

where V is the bubble volume and T is the temperature. The number of water moles that are in the bubble n_{H_2O} have been calculated on the base of EOS and bubble radius. An hypothesis has been made, that the water vapor is very short compared to the gas in the bubble. This hypothesis is perfectly respected in the simulated test cases because the vapor saturation pressure is 2330 Pa that is lower than the initial gas pressure, *i.e.* nearly 1.3^5 Pa . Finally it is possible to compute the number of vapor moles on the base of EOS. In the case of perfect gas the moles are:

$$n_{H_2O} = \frac{P_v \left[\frac{4}{3} \pi R^3 \right]}{\Re T} [\text{mol of vapor}], \quad (4.20)$$

where \Re is the gas perfect constant $8.914 \text{ J}/(\text{mol} * \text{K})$. The radicals have been computed in the case described by Yuan [4]. Results have been obtained by the three equations RP1, RP2 et RP3 with perfect gas EOS and Van der Waals EOS. In all the simulations the RP equation with the resolution of Van der Waals gives a production of OH radicals more elevated than when the perfect gas is used (Fig.4.12).

4.5. RESULTS

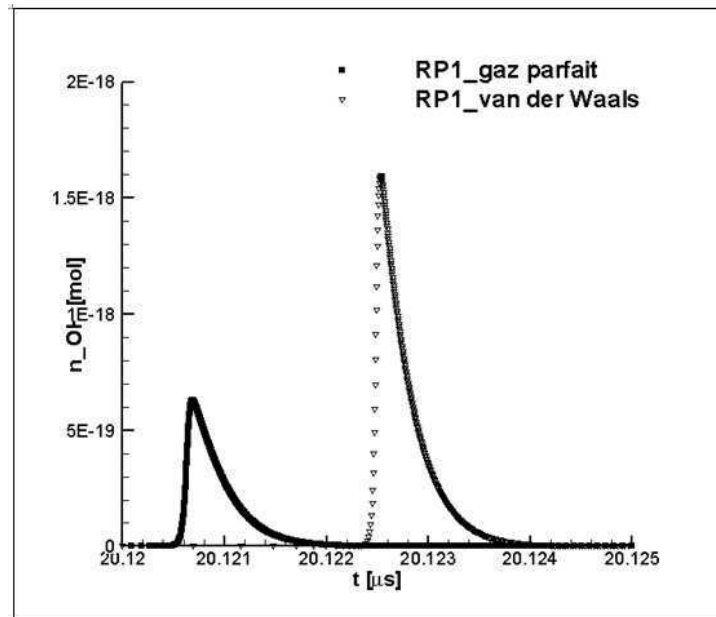


Figure 4.14: Comparison of OH radicals estimations obtained by RP1 with van der Waals EOS and with perfect gas EOS in the test case described by Yuan[4].

4.5. RESULTS

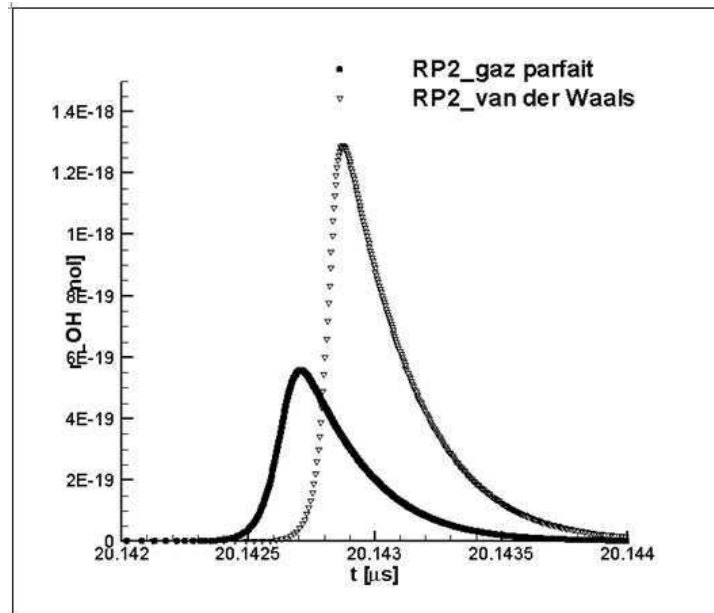


Figure 4.15: Comparison of OH radicals estimations obtained by RP2 with van der Waals EOS and with perfect gas EOS in the test case described by Yuan[4].

4.5. RESULTS

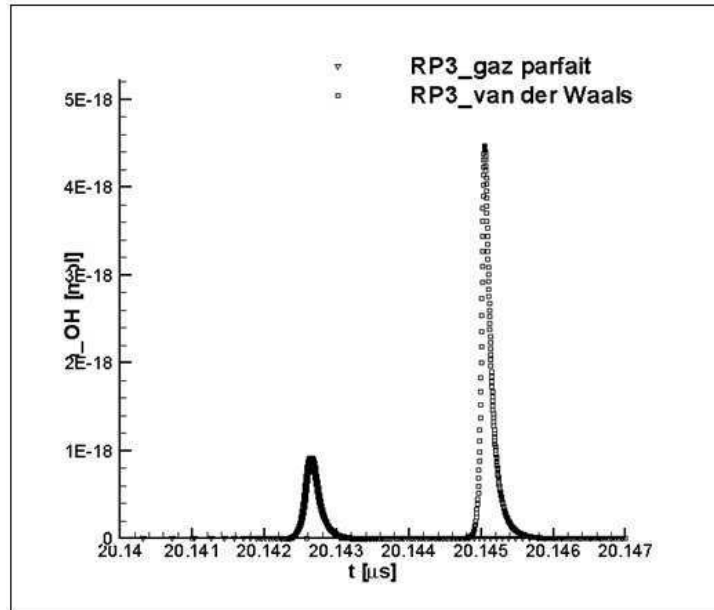


Figure 4.16: Comparison of OH radicals estimations obtained by RP3 with van der Waals EOS and with perfect gas EOS in the test case described by Yuan[4].

4.6 Conclusions

It is known that the degradation of contaminant in the water is enormously influenced by temperature at the center of the bubble during the collapse phase. Then, it is very important to have numerical models allowing to estimate the temperature evolution of the gas bubble. My contribution takes into account the modeling aspect. It has been supposed that pressure and temperature in the bubble are uniform and cavitating bubble behavior has been predicted on the base of several forms of Rayleigh-Plesset equations. These equations have been used in order to reproduce the ultrasonic cavitation and in particular the radius evolution of a bubble subject to an oscillating pressure. This part of work could be resumed in several parts:

- In an in-house code in C language, the classical equation of Rayleigh-Plesset and three others equations (RP1, RP2, RP3), based on Rayleigh-Plesset have been considered
- A first study about the discretization method has been presented. The Runge-Kutta Fehlberg 4-5 and three stages Runge-Kutta TVD have been implemented. The two methods gave nearly the same results, but the Runge-Kutta Fehlberg 4-5 method have a computational cost more elevated, even if it presents a more accurate error estimation. Then, for all the remaining simulations, three stages Runge-Kutta TVD has been retained.
- The in-house code has been validated, simulating the cavitating condition of Leighton [2] for the classical Rayleigh-Plesset equation and the test-case of Lofstedt et al. [3] for the validation of RP1, RP2 and RP3 equations. The numerical profiles obtained are very similar to numerical and experimental profiles given by Leighton [2] and Lofstedt et al. [3].
- The importance of the equation of state for the thermodynamic of the bubble gas has been observed, adopting the Van der Waals equation and the perfect gas equation of state. In all the simulations in which the Van der Waals EOS is used, the temperature has been estimated higher than that one obtained with the perfect gas equation.
- The influence of compressible effect have been estimated. The test cases, [2] and [3], have been simulated, using the classical Rayleigh-

4.6. CONCLUSIONS

Plesset and the RP1 equation. The profiles have been compared and it could be observed that the compressibility effect influence the bubble rebounds, except for the first collapse.

- Finally the OH radicals have been computed, using the RP1, RP2 and RP3 equations with both van der Waals and perfect gas. In all the simulations the estimation of radicals is higher when a Van der Waals equation is used.

Chapter 5

Thermal Effects

5.1 Governing Equations

In this paragraph, the in-house model and the Fluent model are shown. More attention has been devoted to the description of model that has been proposed and used in the in-house code. On the contrary for more details concerning Fluent model, see Fluent theory-guide [61].

5.1.1 Quasi-1D Model

A quasi-one dimensional steady flow in a converging-diverging nozzle has been simulated. The continuity and momentum equations have been solved for the continuous phase coupled with three other equations in order to describe the secondary phase that are a volume fraction equation, the Rayleigh-Plesset equation for the evolution of bubble radius and finally a bubble momentum equation for the estimation of bubble velocity. No equations for the turbulence terms have been considered.

Physical conditions and assumptions

The present study has been based on the following assumptions:

- Liquid and bubbles are in initial dynamic and thermal equilibrium.
- The bubbles contain only vapor and non-condensable gas.

5.1. GOVERNING EQUATIONS

- There is not friction and heat transfer between the flow and the nozzle walls.
- There is not source terms for condensation and evaporation.
- In all simulations, the vapor fraction is shorter than liquid fraction, then it is neglected in continuity and momentum equations.
- The bubbles have a uniform size at any nozzle cross-section.
- Neither coalescence nor fragmentation are considered.
- The flow is incompressible and liquid and vapor density, ρ_l and ρ_v , are constant.
- The temperature and pressure within the bubble are always uniform.

Bubbly flow equations

Let us suppose that the flow develops in only x direction along channel axis, so the normal velocity components can be neglected. Then, in the duct, the vapor fraction is always lower than liquid fraction. The continuity and momentum equations of bubbly flow have been widely studied by Wang and Brennen [62, 63] and they take the following forms:

$$\frac{\partial(1-\alpha)A}{\partial t} + \frac{\partial(1-\alpha)Au}{\partial x} = 0, \quad (5.1)$$

$$\frac{\partial u}{\partial t} + u \frac{\partial u}{\partial x} = -\frac{1}{2(1-\alpha)} \frac{\partial Cp}{\partial x}, \quad (5.2)$$

where $Cp(x, t) = (p(x, t) - p_0)/(0.5\rho_l u_0^2)$ is the fluid pressure coefficient, $p(x, t)$ is the fluid pressure, p_0 is the upstream fluid pressure, u_0 is the upstream liquid velocity, $A(x)$ is the cross-section area. The definition of bubbly void fraction $\alpha(x, t) = 4/3\pi\eta R(x, t)^3/[1 + 4/3\pi\eta R(x, t)^3\eta_s]$ introduces a new unknown in the system that is the radius of the bubble $R(x, t)$.

Bubble Equations

As explained in the previous paragraph, it is necessary an equation in order to take into account the evolution of bubble radius $R(x, t)$ in the Ventury tube. Introducing a classical Rayleigh-Plesset equation [9], a relation between the pressure field and the bubble radius is solved. In this work, the Rayleigh-Plesset equation (RP) includes the viscosity term (second last left term in Eq.(5.3), the surface tension term (last left term in Eq. (5.3)), the term of incondensable gas (first right term in Eq.(5.3)), the pressure term (second right term in Eq.(5.3)) and the thermal effect term (last right term in Eq.(5.3)):

$$R \frac{D^2 R}{Dt^2} + \frac{3}{2} \left(\frac{DR}{Dt} \right)^2 + \frac{4\nu_l DR}{RDt} + \frac{2S}{\rho_l R} = \frac{p_{g0}}{\rho_l} \left(\frac{R_0}{R} \right)^{3k} + \frac{P_v(T_\infty) - p(x, t)}{\rho_l} + \frac{P_v(T_b) - P_v(T_\infty)}{\rho_l}, \quad (5.3)$$

where D/Dt is a Lagrangian derivative, ν_l is the liquid viscosity, S is superficial tension, ρ_l is the liquid density, T_b is bubble temperature and T_∞ , is the flow temperature far from the bubbles, corresponding to the upstream liquid temperature, p_{g0} is the incondensable gas pressure and $k = 1.4$ is the coefficient of the polytropic law. The RP equation permits to introduce in the system a term for the estimation of the thermal effects. As explained by Brennen [9] and successively by Franc [14], in the term (d) of Eq.(5.3), $P_v(T_b)$ and $P_v(T_\infty)$ are the vapor pressures corresponding, respectively, to bubble temperature and liquid temperature far from the bubble. In the case of isothermal hypothesis, the two vapor pressures are equal because $T_b = T_\infty$, otherwise, this term takes into account the difference of temperature between the upstream liquid and the bubble, because of the phase transition after the apparition of cavitation. Then the vapor pressure corresponding to the bubble temperature is lower than the upstream or liquid temperature far from cavitating zone. If the difference of temperature is small, as in the simulated cases, the Taylor expansion can be computed as $P_v(T_b) - P_v(T_\infty) = (dP_v/dT)(T_b - T_\infty)$ where the temperature difference is calculated by balancing the latent heat associated with evaporation or (condensation) with the heat exchanged between the liquid and the bubble [14, 64]:

5.1. GOVERNING EQUATIONS

$$\frac{D}{Dt} \left(\frac{4}{3} \pi R^3 \rho_v \right) L_{ev} = 4\pi R^2 h_b (T_\infty - T_b), \quad (5.4)$$

where L_{ev} is the liquid latent heat and h_b is the bubble convective heat transfer coefficient. Finally substituting the Eq.(5.4) in Eq.(5.3) and considering the Taylor expansion, the RP equation becomes:

$$\begin{aligned} R \frac{D^2 R}{Dt^2} + \frac{3}{2} \left(\frac{DR}{Dt} \right)^2 + \frac{4v_l DR}{RDt} + \frac{2S}{\rho_l R} = \frac{p_{g0}}{\rho_l} \left(\frac{R_0}{R} \right)^{3k} + \\ + \frac{P_v(T_\infty) - p(x, t)}{\rho_l} + \frac{dP_v}{dT} \frac{L_{ev} \rho_v}{\rho_l h_b} \frac{DR}{Dt} \end{aligned} \quad (5.5)$$

By means of the heat balance equation (Eq.(5.4)) between the liquid and the bubble, the convective heat transfer coefficient h_b is introduced in the model and it represents a crucial parameter that it is difficult to estimate.

Convective Heat Transfer Coefficient Modeling

For a better estimation of the temperature decrease, it is necessary to give an accurate prediction of this coefficient. In the first part of this study, the h_b coefficient has been considered as a constant. It has been varied in a range between 1×10^{03} and $1 \times 10^{+10}$ in order to know the influence of this parameter on the prediction obtained by cavitation model. All the results have been compared with experimental data allowing to find the best range of h_b permitting to reproduce the experimental results. On the contrary, in the second part of this work, several h_b models have been tested in cryogenic flows and they have been compared with respect to experimental data. A significant issue in cryogenic flows is to find the operative range of convective heat transfer coefficient for different cryogenic fluids. Before presenting results of sensitivity analysis, let us explain the physical meaning of h_b coefficient and its correlation to cavitation model. The heat transfer coefficient h_b is the ratio between the heat flux, q , per unit area, q/A , transferred by convection or phase transition, and the difference of temperature ΔT , in cavitating flow, between the bubbles and the surrounding liquid:

$$h_b = \frac{q}{A \Delta T}. \quad (5.6)$$

Then, the liquid phase gives (or absorbs) heat in order to evaporate (or to condensate) and this exchange produces a reduction (or increase) of liquid

5.1. GOVERNING EQUATIONS

temperature. Then, initial liquid evaporation depends on the liquid capacity to exchange heat. Then, it is possible to observe a very elevated temperature drop, corresponding to a short vapor production (or vice-versa). If heat exchange in cavitating flows should be estimated, it is evident the importance of convective heat transfer coefficient h_b . Let us suppose evaporation of a liquid and that a wrong value of h_b is considered:

- If h_b is over-estimated, this means that a temperature difference inferior to the real difference in the liquid is supposed. Let us consider the last term of Eq.(5.3), representing thermal effects. More h_b increases, more this term approaches to zero. In this case, *i.e.* for the last term of Eq.(5.3) close to zero, the Eq.(5.3) becomes a classical Rayleigh-Plesset equation for isothermal flows. Then, a value of h_b very high generates a bubble radius forty or fifty time bigger than initial radius, and thus an elevated vapor fraction [44, 62, 63].
- On the contrary, if h_b is under-estimated, this means that a temperature difference superior to the real difference is supposed. Then, the bubble growth or its collapse is dominated by the thermal effect. In fact, the last term of Eq.(5.3) is greater than other terms, then a value of h_b very low determines a reduction of cavity and a small vapor fraction [65, 12, 26, 66].

In this work, three models have been analyzed in order to estimate the bubble convective heat transfer coefficient:

- Ranz and Marshall [5] studied the evaporation of droplets in connection with spray drying and presented an equation for molecular transfer rate during evaporation along the flight path of the droplet. They propose the following correlation for the bubble Nusselt number:

$$Nu_b = 2 + 0.6Re_b^{1/2}Pr^{1/3} \text{ and } h_b = \frac{Nu_b \lambda_l}{2R}. \quad (5.7)$$

Although this model has been proposed for the evaporation of the droplets, this model has been used also in other fields of application. Deligiannis *et al.* [19] used this model in order to study the depressurization of a subcooled or saturated liquid (water or Freon 21). It has been already used in cryogenic flow by Li *et al.* [67], investigating the boiling flow. Finally, the Ranz and Marshall model [5] is implemented

5.1. GOVERNING EQUATIONS

also in the commercial code Fluent and CFX, then for this reason this model has been considered in this study. The model is a function only of the bubble Reynolds number and Prandtl number.

- Recently, Oresta *et al.* [6] combined two asymptotic forms of Nusselt number obtained for high or low bubble Péclet number, obtaining the following correlation for Nu_b :

$$Nu_b = Nu_{b,0} \left[1 + \left(\frac{Pe_b}{Pe_c} \right)^{n/2} \right]^{1/n} \text{ and } h_b = \frac{Nu_b \lambda_l}{2R}, \quad (5.8)$$

where n is a fitting of other results [6] and it is assumed equal to 2.65. An analysis of sensitivity of n has been taken into account, but the bubble temperature profiles, obtained at different values of n , present only slightly differences. $Nu_{b,0} = 2 + (6Ja/\pi)^{1/3} + (12Ja/\pi)$ is the Nusselt number defined for low bubble Péclet number, with $Ja = \rho_l c_{pl}(T_\infty - T_{sat})/\rho_v L_{ev}$. Also $Pe_c = \pi Nu_{b,0}^2/4$ is the crossover Péclet number and the bubble Péclet is defined $Pe_b = Re_b Pr = 2R|v - u|/\kappa$, with κ is the liquid thermal diffusivity. This model has been tested exclusively in conditions of natural convection of water flows. However, this model is a function of bubble Reynolds number and Prandtl number through the Péclet number and then it is also a function of temperature by means of the Jacob number appearing in the bubble Nusselt number. The dependence from the temperature gives the possibility to estimate its influence in the prediction of h_b coefficient and also of the temperature drop. This model has been used in condition of natural convection of water.

- The last approach has been used by Christopher *et al.* [7] in order to study the Marangoni effect on a bubble that moves on a heated wire:

$$h_b = \frac{2\hat{\sigma}}{2 - \hat{\sigma}} \frac{\rho_v L_{ev}^2}{T_v} \left(\frac{\bar{M}}{2\pi \bar{R} T_v} \right)^{1/2} \left[1 - \frac{P_v(T_b)}{2L_{ev}\rho_v} \right] \quad (5.9)$$

where $\hat{\sigma}$ is the accommodation coefficient equal to 0.03 for water flow, \bar{M} is the vapor molecular weight, \bar{R} is the universal gas constant and T_v is the vapor temperature equal to bubble temperature

5.1. GOVERNING EQUATIONS

for the pressure inside the bubble, obtained by Laplace and Clausius-Clapeyron equation: $T_v = T_{sat} + [2\sigma T_{sat}/(L_{ev}\rho_v R)]$, with T_{sat} is the saturation temperature at the upstream pressure p_0 . This last model presents very different characteristics compared to the first two models, because it is a function exclusively of bubble conditions. Also in our previous study [68], we estimated the validity of this model in the simulation of cryogenic cavitating flow and for the estimation of thermal effects. Then, we have compared this model to the others.

Bubble Velocity

In the definition of Re_b , used in the Ranz and Marshall and Oresta models, the relative motion between the phases occurs and so the bubble velocity equation is solved. The bubble momentum equation has been used in a cavitating simulation by Albagli [69]. It neglects the term of history forces and the material transport term:

$$\rho_v v \frac{Dv}{Dt} + \frac{1}{2} \rho_l \left(\frac{Dv}{Dt} - \frac{Du}{Dt} \right) = -\frac{\partial p(x, t)}{\partial x} - \frac{3}{8} \rho_l C_D \frac{(v - u)|v - u|}{R}, \quad (5.10)$$

where $v(x, t)$ is the bubble velocity and the C_D is the drag coefficient equal to 0.444 (see [69]). *Numerical Methods*

Numerical Methods

All terms of Eq.(2.2)-(5.10) have been transformed in their dimensionless form, using the upstream value, obtained considering the following dimensionless variables $\bar{u} = u/u_0$, $\bar{x} = x/R_0$, $\bar{R} = R/R_0$, $\bar{\eta} = \eta R_0$, $\bar{L} = L/R_0$, $\bar{t} = tu_0/R_0$ where the upstream condition are denoted by subscript "0", the variables dimensional value is denoted by superscript "-". t is the time, u is the velocity of flow. R is the bubble radius and η is bubble population for unit of liquid volume, obtained by considering the relation $(1 - \alpha_0) = 1/(1 + 4/3\pi\bar{\eta})$, and L is the length of the nozzle. This gives the possibility to introduce in the equations, the dimensionless Reynolds number $Re = \rho_l u_0 R_0 / \mu_l$, the dimensionless Weber number, $We = \rho_l u_0^2 R_0 / S$ and the cavitation number $\sigma = (p_0 - P_v(T_\infty)) / (0.5 \rho_l u_0^2)$. Only steady 1D flows are considered in this work, so the final equation system is:

$$(1 - \alpha) \bar{u} \bar{A} = (1 - \alpha_0) = constant \quad (5.11)$$

5.1. GOVERNING EQUATIONS

$$\bar{u} \frac{d\bar{u}}{d\bar{x}} = -\frac{1}{2(1-\alpha)} \frac{dCp}{d\bar{x}} \quad (5.12)$$

$$\alpha(x, t) = \frac{\frac{4}{3}\pi\eta\bar{R}}{\left[1 + \frac{4}{3}\pi\eta\bar{R}\right]} \quad (5.13)$$

$$\begin{aligned} \bar{R} \left(\bar{u}^2 \frac{d^2\bar{R}}{d\bar{x}^2} + \bar{u} \frac{d\bar{u}}{d\bar{x}} \frac{d\bar{R}}{d\bar{x}} \right) + \frac{3\bar{u}^2}{2} \left(\frac{d\bar{R}}{d\bar{x}} \right)^2 + \frac{4\bar{u}}{Re\bar{R}} \frac{d\bar{R}}{d\bar{x}} + \frac{2}{We} \left(\frac{1}{\bar{R}} - \frac{1}{\bar{R}^{3k}} \right) = \\ -\frac{Cp}{2} - \frac{\sigma}{2} \left(1 - \frac{1}{\bar{R}^{3k}} \right) + \frac{dP_v}{dT} \frac{L_{ev}\rho_v}{\rho_l h_b u_0} \bar{u} \frac{d\bar{R}}{d\bar{x}} \end{aligned} \quad (5.14)$$

$$h_b = f(Re, Pr) \text{ or } h_b = f(Re, Pr, Ja) \text{ or } h_b = f(\text{bubble conditions}) \quad (5.15)$$

$$\left(\rho_v + \frac{1}{2}\rho_l \right) \bar{v} \frac{d\bar{v}}{d\bar{x}} + \frac{1}{2}\rho_l u_0^2 \frac{d\bar{u}}{d\bar{x}} = -\frac{p}{\bar{x}} - \frac{3}{8}\rho_l C_D u_0^2 \frac{(\bar{v} - \bar{u})|\bar{v} - \bar{u}|}{\bar{R}} \quad (5.16)$$

The governing equations (Eq.(5.11)-(5.16)) are integrated in space using a four stage Runge-Kutta scheme [70]. This scheme has been widely used in previous studies for the resolution of Rayleigh-Plesset equations. Finally, this model presents two tuning parameters, *i.e.* the initial bubble radius and the initial vapor fraction. In all the simulations we assume that $R0 = 0.0001$ ([62, 71]). On the contrary, the value of α_0 has been calibrated in order to obtain the experimental results.

5.1.2 Ansys-Fluent Model

The numerical simulations have been performed by using the commercial code FLUENT (release 12.1), using the multiphase cavitation modeling approach. It consists in the use of standard viscous flow equations governing the transport of phases (Eulerian multiphase), a $k - \varepsilon$ turbulent model and a model to estimate the liquid-vapor mass transfer due to cavitation phenomenon. The numerical model uses an implicit finite volume scheme, based on the SIMPLE Pressure-Based Algorithm. A second order differentiating scheme is used, except for vapor fraction for which a QUICK schemes have

5.1. GOVERNING EQUATIONS

been used. Continuity and momentum equations are solved for each phase [61].

$$\frac{\partial \alpha_q \rho_q}{\partial t} + \nabla \cdot (\alpha_q \rho_q \vec{v}_q) = \sum_{p=1}^2 (\dot{m}_{pq} - \dot{m}_{qp}), \quad (5.17)$$

$$\begin{aligned} \frac{\partial \alpha_q \rho_q \vec{v}_q}{\partial t} + \nabla \cdot (\alpha_q \rho_q \vec{v}_q \vec{v}_q) = & -\alpha_q \nabla p + \nabla \cdot \bar{\bar{\tau}} + \alpha_q \rho_q \vec{g} + \\ + \sum_{p=1}^2 \left(\vec{R}_{pq} + \dot{m}_{pq} \vec{v}_{pq} - \dot{m}_{qp} \vec{v}_{qp} \right) + & (\vec{F}_q + \vec{F}_{lift,q} + \vec{F}_{vm,q}), \end{aligned} \quad (5.18)$$

where the subscript q characterizes the phase, α_q is the vapor fraction of phase, ρ_q is the physical density, \vec{v}_q is the velocity and \dot{m} characterizes the mass transfer between the two phases, p is the average pressure, $\bar{\bar{\tau}}$ is the phase stress-strain tensor, \vec{R}_{pq} is the interaction force between phases, \vec{v}_{qp} is the interphase velocity and finally \vec{F}_q , $\vec{F}_{lift,q}$, $\vec{F}_{vm,q}$ are respectively the external body force, the lift force and the virtual mass force. In the $k - \varepsilon$ turbulent model, the near-wall region has been modeled by a wall function that bridge the viscosity-affected region between the wall and the fully-turbulent region. A named *standard wall function* has been used basing on the work of Launder and Spalding [72]. As explained before, it is necessary a model for the estimation of mass transfer between the two phases, governed by the vapor transport equation:

$$\frac{\partial \alpha_v \rho_v}{\partial t} + div \cdot (\alpha_v \rho_v \vec{v}_v) = \frac{\rho_v \rho_l}{\rho} \frac{D\alpha}{Dt} = \dot{m}, \quad (5.19)$$

where the subscript v indicate the vapor phase. The mass transfer between the two phases \dot{m} is modeled by Schnerr and Sauer model[73] supposing the same mass for evaporation and the condensation. This model, implemented in Fluent, supposes, also, the presence of a large number of spherical bubbles and it proposes a relation between the vapor volume fraction and radius of bubble:

$$\alpha = \frac{\frac{4}{3}\pi n_b R}{\left[1 + \frac{4}{3}\pi n_b R\right]}, \quad (5.20)$$

where R is the bubble radius and n_b is the nuclei concentration per unit of pure liquid volume. In this case n_b is constant, because it is assumed that

5.2. TEST CASES

no bubbles are created or destroyed. A simplified Rayleigh-Plesset equation is introduced in the system of equations in order to model the bubble radius R :

$$\frac{D\alpha}{Dt} = \sqrt{\frac{2}{3} \frac{P_b - P}{\rho_l}}, \quad (5.21)$$

where D/Dt is the material derivative, P_b is the bubble pressure, P is the pressure far from the bubble. Coupling the Eq.(5.19), Eq.(5.20) and Eq.(5.21) it is possible to obtain a final expression of \dot{m} as follows:

$$\dot{m} = \frac{\rho_v \rho_l}{\rho} \frac{D\alpha}{Dt} = \frac{\rho_v \rho_l}{\rho} \alpha (1 - \alpha) \frac{3}{R} \sqrt{\frac{2}{3} \frac{P_b - P}{\rho_l}}. \quad (5.22)$$

To estimate the thermal effects, it is necessary to introduce two separate enthalpy equations for each phase:

$$\frac{\partial}{\partial t} (\alpha_q \rho_q h_q) + \text{div} \cdot (\alpha_q \rho_q h_q \vec{v}_q) = -\alpha_q \frac{\partial}{\partial t} p + \sum_{p=1}^2 (Q_{pq} + \dot{m}_{pq} \vec{v}_{pq} - \dot{m}_{qp} \vec{v}_{qp}), \quad (5.23)$$

where Q_{pq} is the heat exchange between phases and it is a function of the difference of temperature between the two phase and the convective heat exchange coefficient h_b :

$$Q_{pq} = h_b (T_p - T_q). \quad (5.24)$$

Also in Fluent, the h_b coefficient in Eq.(5.12), should be modeled by an evaluation model. In the code, the Ranz and Marshall model[5] (see Eq.(5.7)) is already implemented. In order to obtain the last objective of this work, *i.e* to confirm the conclusion obtained in the first part of the work, it has been necessary to implement in Fluent, the Christopher model [7] (see Eq.(5.9)) by a purposely-developed C external routine.

5.2 Test Cases

In this work, we deal with numerical simulation of a cavitating hydrogen flow in a Venturi orifice. This configuration has been widely studied experimentally by Hord [1], where 32 cases at different operating conditions and

5.2. TEST CASES

for each case have been presented, and the temperature and pressure experimental profiles have been given. Numerical domain considered in this study is shown in Fig. 5.1. It is constituted by an axial-symmetric geometry that gives the possibility to reproduce the cavitating flow by means of a quasi-one dimensional model.

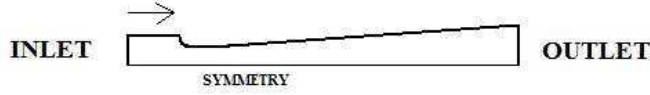


Figure 5.1: Partial view of experimental apparatus reproduced in this study.

The Ventury dimensionless area is given by:

$$\bar{A}(x) = \begin{pmatrix} \frac{(r+c-\sqrt{2rR_0\bar{x}-\bar{R}_0^2\bar{x}^2})^2}{(r+c)^2} & 0 < \bar{x} < r \\ \frac{c^2}{(r+c)^2} & r < \bar{x} < d \\ \frac{(tg(2^\circ,15)R_0(\bar{x}-x_0)-c)^2}{(r+c)^2} & d < \bar{x} < \bar{L}, \end{pmatrix}$$

where $r = 0.0033m$, $c = 0.01238250m$, $d = 0.016764m$ and $x_0 = 0.016764m$. For each case, B-factor of Stepanoff has been computed, considering the ratio between the real temperature drop ΔT and the theoretical temperature drop ΔT^* . In particular, ΔT represents the difference between the inlet temperature T_0 and the lowest experimental temperature observed in cavitating region. The computed B-factor has been called B_{EXP} . Most of values of B_{EXP} are between 1.5 and 3 (Fig.5.2) and this shows that the temperature drop is more elevated than the theoretical temperature drop. It is interesting the growing trend of B_{EXP} compared with cavitation number σ (Fig.5.2). More elevated values appear in the cases with $\sigma > 1.8$ (Fig.5.2) and inlet temperature $T_0 < 0.63K$ (in Fig.5.2). These cases are characterized by a tax of cavitation shorter or corresponding to inception of cavitation. It is not possible to obtain a trend of B_{EXP} with respect to Reynolds number (Fig.5.2).

5.2. TEST CASES

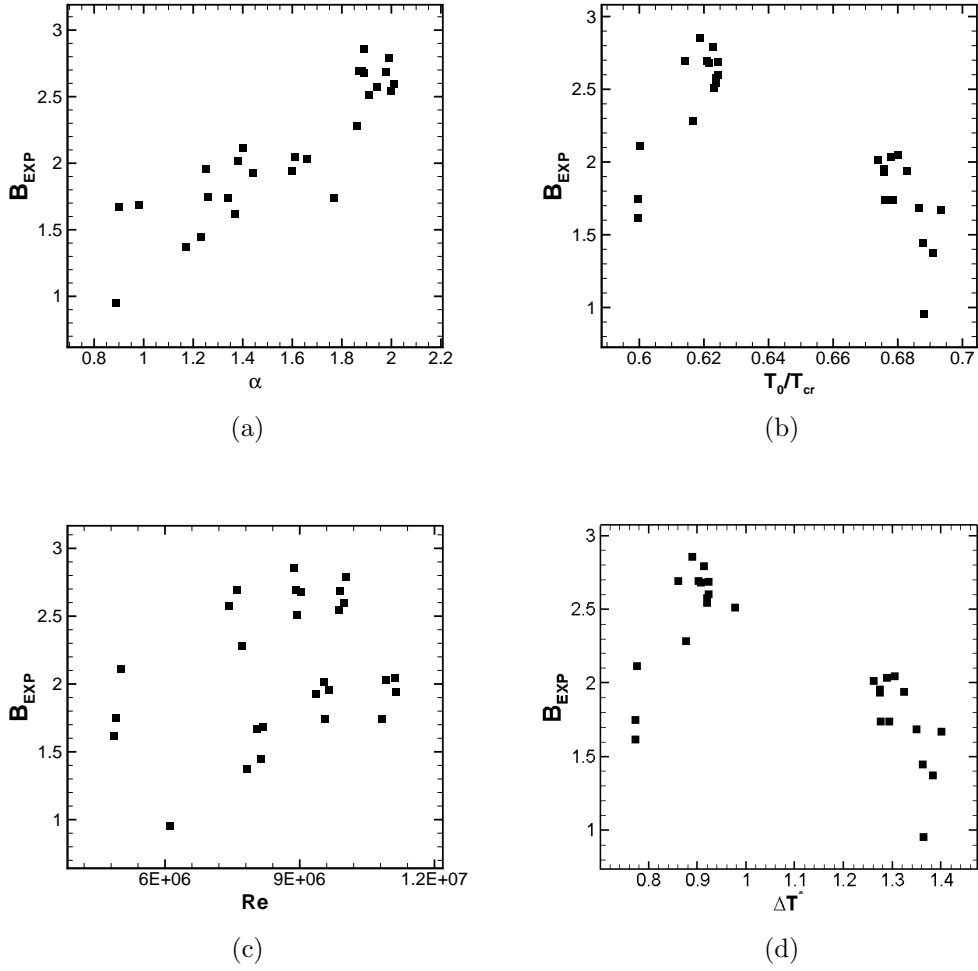


Figure 5.2: B_{EXP} compared with (a) cavitation number σ , (b) inlet temperature T_0 , (c) Reynolds number Re and (d) theoretical temperature drop ΔT^*

5.3 Grid Convergence for 1D CFD code

The grid convergence study has been performed simulating the cavitating flow obtained with velocity inlet $v_0 = 32.3m/s$, pressure inlet $p_0 = 0.230MPa$ and hydrogen temperature inlet $T_0 = 22.77$, corresponding to 121B test-case [1]. The flow-field has been computed on uniform grids of increasing density: the finer grid is of 480×10^6 of points and the coarser one is of 30×10^6 of points. The scheme's order of convergence is estimated following the Roache's method [74] based on Richardson extrapolation. The computed order of convergence is based on the liquid velocity u (Fig.5.4), the velocity of bubble interface dR/dx and bubble radius R (Fig.5.3). In order to identify the grid that assures a good trade-off between the solution accuracy and the computational cost, the grid convergence index (GCI) on the grid of 60 millions of points has been computed, which represents an estimate of how far the numerical solution is from its asymptotic value. GCIs of 0.61%, 0.46% and $2.5e-04\%$ have been found for dR/dx , R and u , respectively, indicating that the solution is well within the asymptotic range. Considering the errors lower than 1%, the grid of 60 millions of points has been used for all the other simulations. As it can be seen in the next figure, solution obtained with 60 millions of points is well converged.

5.4 Results and Discussion

The objectives of this work are the following:

- A sensitivity analysis of the convective heat transfer coefficient in hydrodynamic cavitation at high Reynolds number and in cryogenic environment, using an in-house code. The aim is to identify:
 - The influence of the parameter h_b on cavitation prediction in cryogenic fluids.
 - A characteristic range of h_b for hydrogen cavitation.

They are presented in paragraph 5.4.1.

- Analysis of three models for convective heat transfer coefficients prediction, proposed by Ranz and Marshall [5], Oresta *et al.* [6] and Christopher *et al.* [7]. They have been coupled to mixture mass and momentum conservative equations. The aim is :

5.4. RESULTS AND DISCUSSION

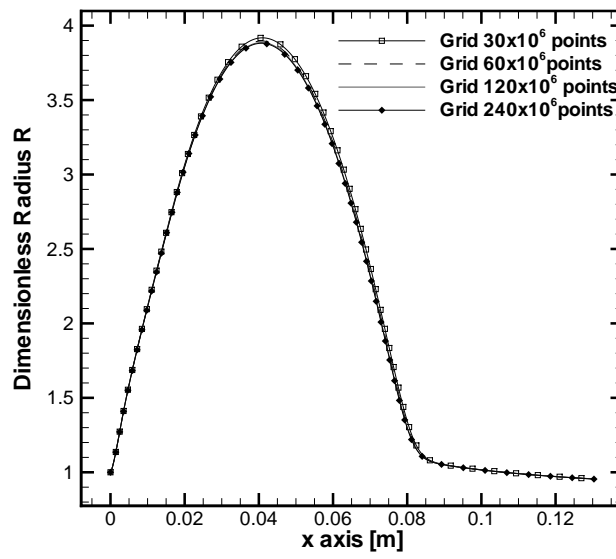


Figure 5.3: Profiles of bubble radius R in 121B case [1] obtained by using four different grids.

5.4. RESULTS AND DISCUSSION

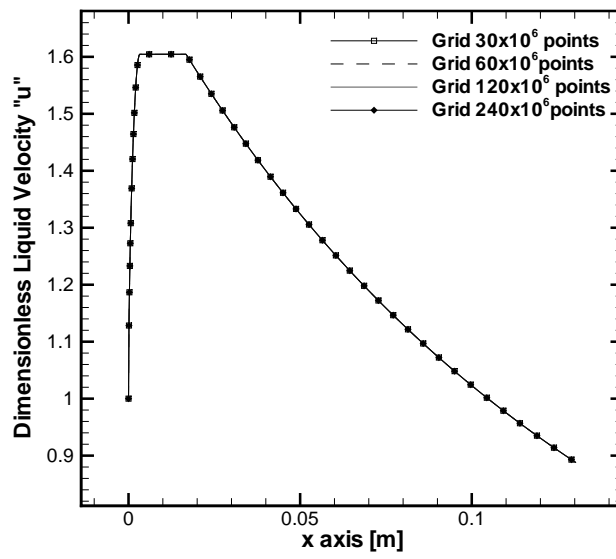


Figure 5.4: Profiles of liquid velocity in 121B case [1] obtained by using four different grids.

- To re-examine the validity of these models in the framework of cryogenic fluids.

They are presented in paragraph 5.4.2.

- Two-dimensional simulation of a test case [1] by means of FLUENT code. The aim is :
 - To confirm the conclusions obtained by the analysis with the quasi-1D code.
 - To implement in the CFD code a new model for a better estimation of temperature decrease in cryogenic cavitating flow.

They are presented in paragraph 5.4.3.

As already said, in the first part of the work, a 1D model has been used, even if the simplified model does not allow predicting accurately the cavitation phenomenon, because it is based on assumptions that neglect some complex characteristics of the phenomenon. On the other hand, our aim is not to develop a new cavitation model, but to investigate the thermal effect in cryogenic cavitation through the study on the convective heat transfer coefficient. For the simulation in Fluent, a 2D steady Euler model has been used [61]. The interactions between the two phases due to cavitation are modeled with Schnerr and Sauer model [73] implemented in the code, coupled with two of the models for h_b estimation, used before.

5.4.1 Constant Convective Heat Transfer Coefficient h_b

A sensitivity analysis of h_b has been performed in order to obtain a reasonable order of magnitude of this parameter in cavitating flows for hydrogen (H₂). The analysis has been carried out by varying h_b coefficient between 1×10^{10} and 1×10^{03} and varying, for each h_b , the upstream vapor fraction between 1×10^{-10} and 1×10^{-03} . Then, a set of 576 simulations has been performed for 26 cases simulated [1]. Numerical solutions have been compared to experimental data in terms of temperature and pressure [1]. To understand the influence of convective heat transfer coefficient h_b , for the case 121B [1] the temperature and vapor profiles obtained with the highest

5.4. RESULTS AND DISCUSSION

$h_b = 1 \times 10^{10}$ and a very low $h_b = 1 \times 10^{05}$, have been shown. The simulation have been obtained varying the inlet vapor fraction α_0 , that represents our tuning parameter. Usually, in isothermal case, when α_0 grows, the initial bubble number in the Ventury is supposed greater and then the vapor fraction increases [62]. Supposing a flows with thermal effect, also the value of h_b influences the profiles of vapor fraction and temperature. In the first case, *i.e.* with a $h_b = 1 \times 10^{10}$, when the inlet vapor fraction α_0 increases, the vapor fraction increases in the Ventury as far as the creation of flashing phenomenon (see [62] with $\alpha_0 \geq 1 \times 10^{06}$ (Fig.5.6). However, the temperature profiles are close to the initial liquid temperature T_0 (Fig.5.5). This means that: (i) the value of h_b is very high and it resets the thermal term in Rayleigh-Plesset equation (last term of Eq.(5.3)). Then, the cavitation phenomenon is controlled exclusively by the pressure term (second last term of Eq.(5.3)) as it is possible to observe in Fig.5.7, where the absolute value of thermal effect and the pressure effect are compared; (ii) the value of h_b is wrong because the temperature profiles presents a very high error compared to the experimental temperature drop. Anyway, when $h_b = 1e + 05$, the growth of vapor is controlled by the thermal term (Fig.5.10). Then, the numerical temperature drop gives a good estimation of experimental temperature drop (Fig.5.8). The value of h_b is wrong again in this case, because the experimental cavity length is greater than the numerical one.

We defined several parameters, useful in order to analyze qualitatively the results:

- h_{bMAX} , such that for every $h_b > h_{bMAX}$, growth is governed exclusively by mechanical forces, represented in Eq.(5.3) by c term in Eq.(5.3)(see Brennen [9]).
- h_{bOPT} that represents the range of values permitting to obtain the best profiles of temperature and pressure by comparison with experimental data.
- h_{bMIN} , such that for every $h_b < h_{bMIN}$, growth is governed exclusively by thermal effects, represented in Eq.(5.3) by d term in Eq.(5.3) (see Brennen [9]).

Basing on previous remarks, h_{bMAX} is the value for which the simulation can provide a prediction for the difference of temperature between the inlet temperature T_0 and the lowest temperature in the throat $\Delta(T)_{NUM} =$

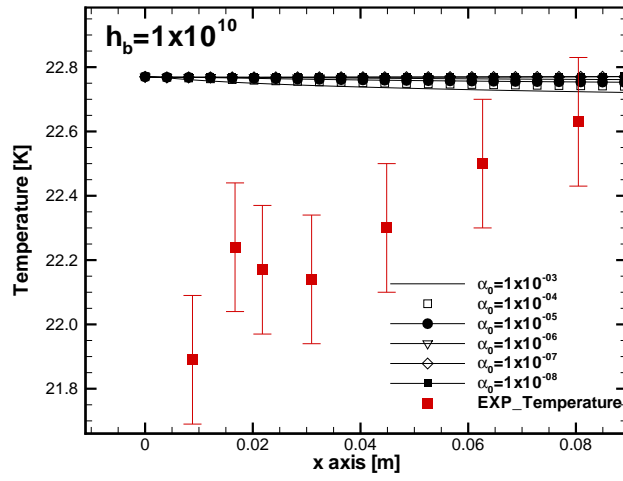


Figure 5.5: Comparison of temperature profiles for the case 121B [1] with $h_b = 1 \times 10^{+10}$ at different upstream vapor fraction α_0 and initial radius $R_0 = 1 \times 10^{-04}m$. The experimental temperature error is of $\pm 0.1K$.

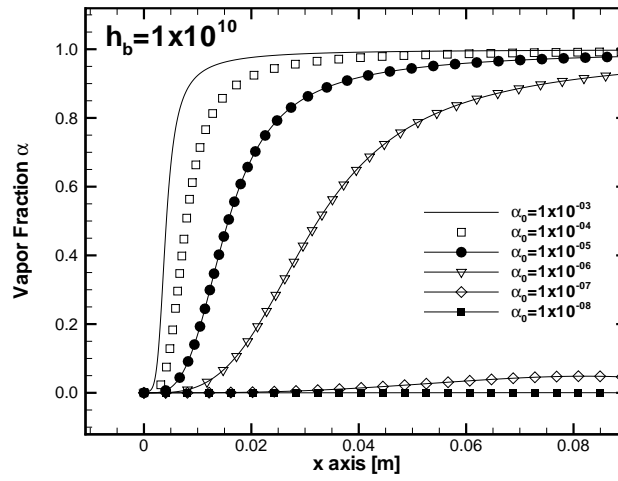


Figure 5.6: Comparison of vapor fraction profiles for the case 121B [1] with $h_b = 1 \times 10^{+10}$ at different upstream vapor fraction α_0 and initial radius $R_0 = 1 \times 10^{-04}m$.

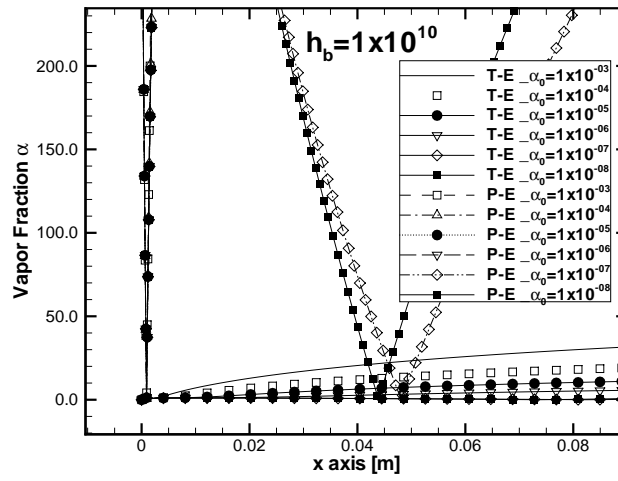


Figure 5.7: Comparison of absolute value of thermal (T-E) and pressure (P-E) effects for a $h_b = 1 \times 10^{+10}$ at different upstream vapor fraction α_0 and initial radius $R_0 = 1 \times 10^{-04}m$.

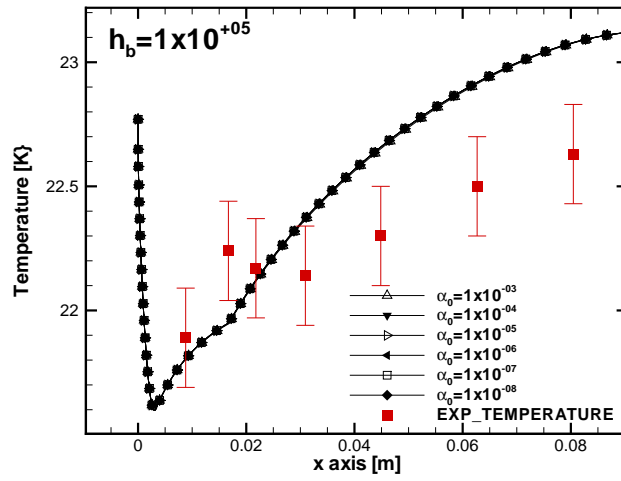


Figure 5.8: Comparison of temperature profiles for the case 121B [1] with $h_b = 1 \times 10^{+05}$ at different upstream vapor fraction α_0 and initial radius $R_0 = 1 \times 10^{-04}m$. The experimental temperature error is of $\pm 0.1K$.

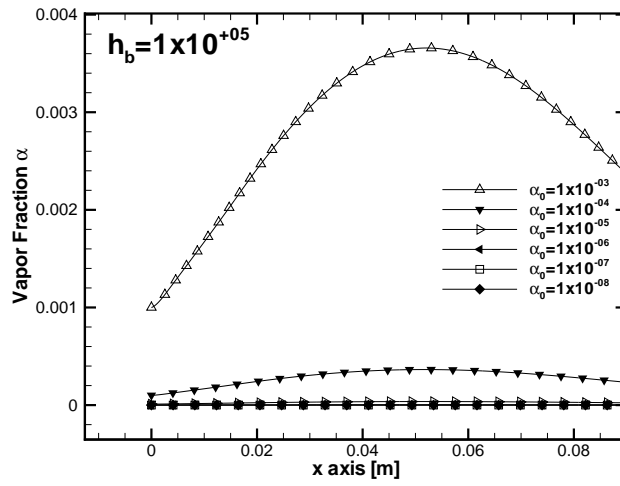


Figure 5.9: Comparison of vapor fraction profiles for the case 121B [1] with $h_b = 1 \times 10^{+05}$ at different upstream vapor fraction α_0 and initial radius $R_0 = 1 \times 10^{-04}m$.

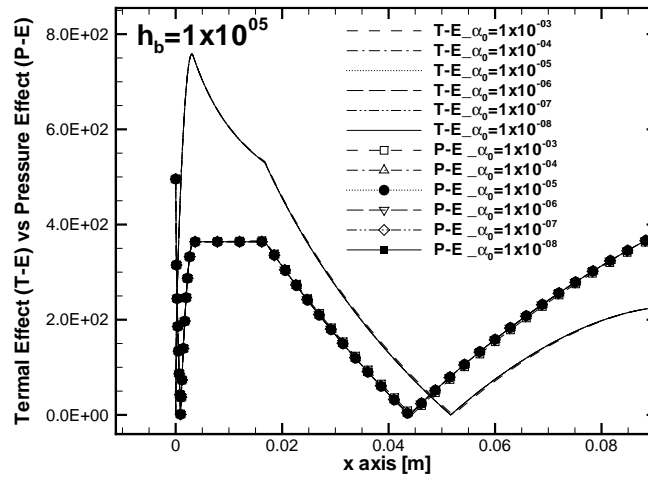


Figure 5.10: Comparison of absolute value of thermal (T-E) and pressure (P-E) effects for a $h_b = 1 \times 10^{+05}$ at different upstream vapor fraction α_0 and initial radius $R_0 = 1 \times 10^{-04}m$.

5.4. RESULTS AND DISCUSSION

$0.3\Delta T_{EXP} = (T_0 - T_{EXP})$ and the temperature profiles obtained at different inlet vapor fraction α_0 that are constant (Fig.(5.3)). This threshold has been arbitrarily chosen in order to identify the region in which the growth is controlled exclusively by mechanical force. Conversely, h_{bMIN} is the value permitting to obtain or over-estimate, the experimental temperature drop, but the difference between the profiles of temperature, pressure and vapor fraction obtained at different initial vapor fraction α_0 are negligible. This threshold has been again arbitrarily chosen. For each case, comparisons of the numerical profiles of temperature and pressure, obtained with a constant value of h_b , with experimental data [1] have been performed. It can be observed, that: (i) in several cases, there is not a value of h_b that allows to obtain a perfect fit between numerical and experimental results; (ii) however there is a range of value, that we called h_{bOPT} , for which it is possible to obtain the temperature and pressure profiles presenting a short error compared with experimental data (Fig. 5.11 and Fig. 5.12).

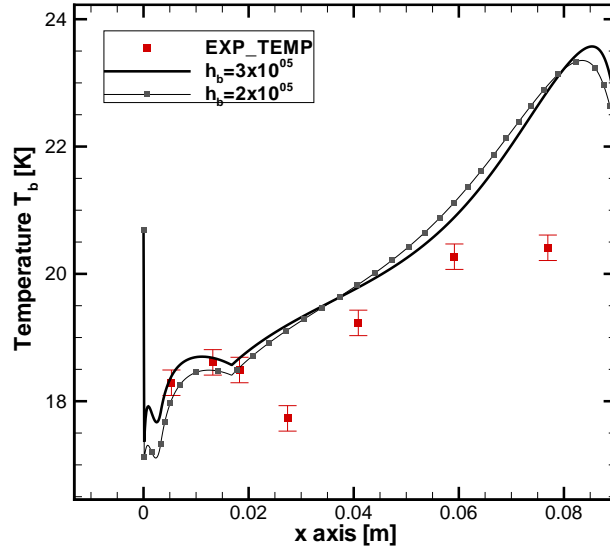


Figure 5.11: Comparison between numerical bubble temperature T_b and experimental temperature for the case 134[1], with $Re = 9.9 \times 10^{+06}$, $T_0 = 20.69$, $\sigma = 2.01$ and $\alpha_0 = 1 \times 10^{-03}$. The experimental temperature error is of $\pm 0.1K$.

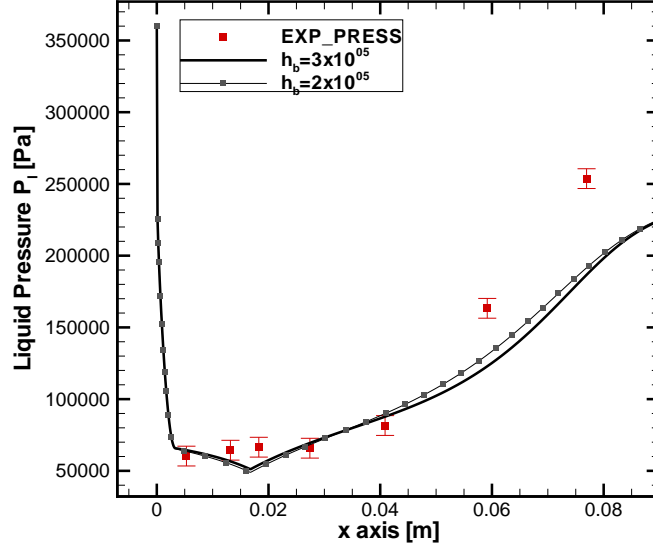


Figure 5.12: Comparison between numerical liquid pressure P_l and experimental liquid pressure for the case 134[1], with $Re = 9.9 \times 10^{+06}$, $T_0 = 20.69$, $\sigma = 2.01$ and $\alpha_0 = 1 \times 10^{-03}$. The experimental pressure error is of $\pm 6900 Pa$.

For each case, the h_{bMAX} , h_{bOPT} and h_{bMIN} have been computed and represented in Fig.(5.13)-Fig.(5.16) with respect to B-factor, cavitation number σ , Reynolds number Re and T_0/T_c (with critical temperature $T_c = 33.145K$), respectively. The h_{bOPT} is marked with a bar representing the range of value of h_b for which a solution is considered as acceptable. This value is closed to h_{bMIN} value, confirming that in hydrogen cavitating flow the growth of bubbles is more controlled by thermal effect than mechanical force (Fig.(5.14)). Even if all cases present very similar operative conditions and it is difficult to observe clear trends of h_{bOPT} , however, slight differences can be observed. A parametric study on three variables (inlet temperature T_0 , the number of cavitation σ and the Reynolds number Re) have been performed by varying one variable each time. Results show that:

- If Re is almost constant and $19.87 < T_0 < 20.34$, the h_b coefficient do not change, because also the σ remains almost constant. Conversely when the inlet temperature is $22.69 < T_0 < 22.98$ the h_b coefficient

5.4. RESULTS AND DISCUSSION

increases with the increase of σ (Fig.(5.14)).

- If Re and σ are almost constant, increasing the inlet temperature induces an increase of h_b with the exception of cases with an inlet temperature $T_0 > 22.69$ for which the h_b coefficient do not vary consistently.
- By varying Reynolds number, there are not clear trends of h_b coefficient.

From this analysis, it is possible to observe an high influence of cavitation number on trends of h_b , more than inlet temperature. In fact, for the same σ , h_b increases with the increase of inlet temperature, even if the conditions approach critical conditions (critical temperature of hydrogen is $T_c = 33.145$). However, the cases with a more elevated inlet temperature present, also, a cavitation number $\sigma < 1.6$ for which a "developed" cavitation regime exists and the vapor fraction appears more elevated. Only values for h_b more elevated allow obtaining a more elevated vapor fraction, because a bubble mechanical growth is supposed.

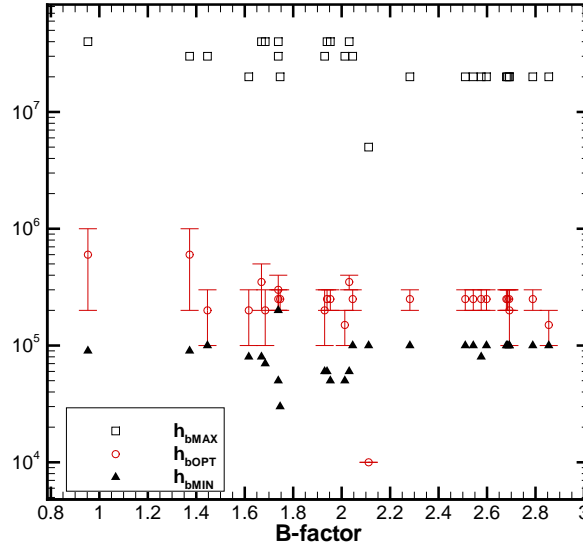


Figure 5.13: h_{bMAX} , h_{bOPT} and h_{bMIN} obtained for each case, with respect to B-factor.

5.4. RESULTS AND DISCUSSION

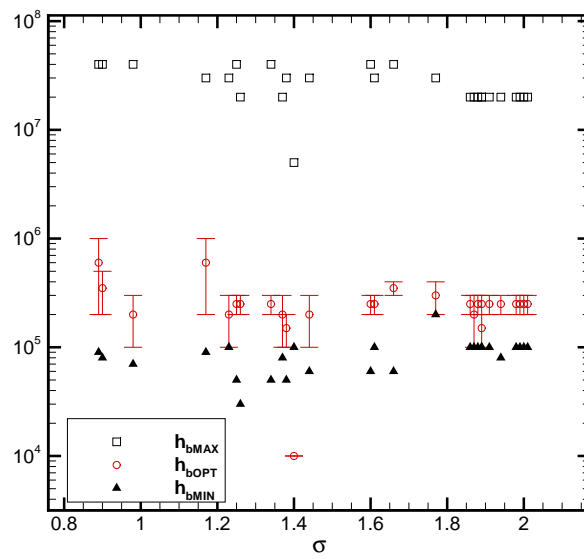


Figure 5.14: h_{bMAX} , h_{bOPT} and h_{bMIN} obtained for each case, with respect to cavitation number σ .

5.4. RESULTS AND DISCUSSION

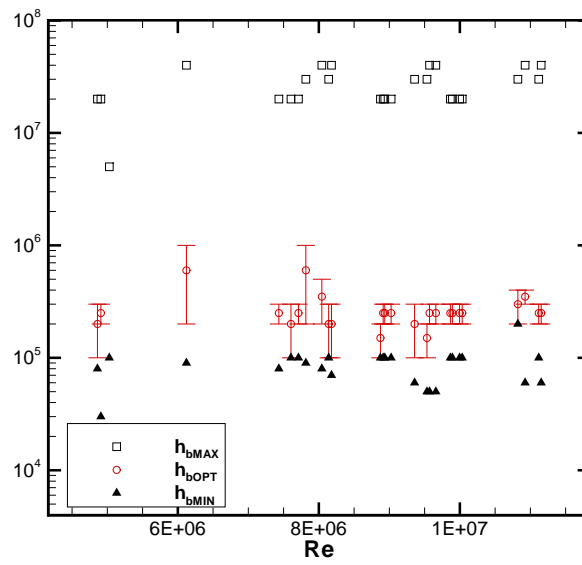


Figure 5.15: h_{bMAX} , h_{bOPT} and h_{bMIN} obtained for each case, with respect to Reynolds number.

5.4. RESULTS AND DISCUSSION

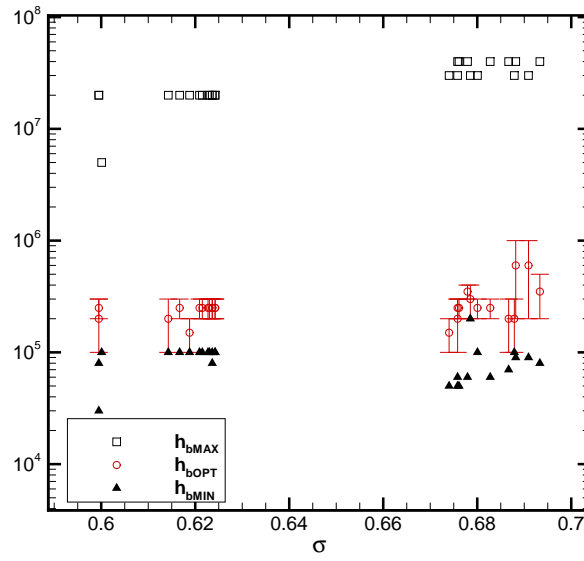


Figure 5.16: h_{bMAX} , h_{bOPT} and h_{bMIN} obtained for each case, with respect to T_0/T_c (with critical temperature $T_c = 33.145K$)

5.4.2 Theoretical Models for the Estimation of Convective Heat Transfer Coefficient $h_b(x)$

The previous sensitivity analysis pointed out two important remarks: (i) there is an optimal range for hydrogen cavitating flow that is about $1 \times 10^{05} < h_b < 1 \times 10^{06}$, then it is necessary to adopt a model for the estimation of h_b coefficient; (ii) the optimal value of h_b is more influenced by inlet temperature T_0 and by σ , than Reynolds number. Basing on this consideration, beyond the classical Ranz and Marshall model [5], largely used in previous studies and implemented in commercial CFD code, we focus on models that, in their formulations, present a dependence on some factors permitting to improve the prediction of h_b in cryogenic flows. However, at our knowledge, only Ranz and Marshal model[5] has been used with cryogenic fluid. For all the cases, the profiles obtained with the three models have been compared with experimental data and, in particular, three cases have been shown, 125A, 120B and 123B (see [1]), because they present, respectively, an experimental temperature drops of 0.2K, 1.2K and 2.7K (Fig.(5.17)-(5.19)). It is evident that the Ranz and Marshal model[5] gives always an over-estimation of temperature drop (Fig.(5.17)-(5.19)), that becomes very evident when the thermal effects are short as in the case 125A (Fig.(5.17)). The Ranz and Marshal model[5] gives always a value of h_b coefficient lower than the optimal range estimated with the sensitivity analysis at constant h_b , that in Fig.(5.26)-(5.28) is represented by a grey rectangle. A lower h_b value determines also a low estimation of radius growth (Fig.(5.23)-(5.25)) as in non-cavitating flow. Conversely, the other two models are in good agreement with experimental data of pressure (Fig.(5.20)-(5.22)) and temperature (Fig.(5.17)-(5.19)), except for the case 125A, that presents an experimental temperature drop of 0.2K, while Christopher [7] and Oresta model [6] determine, respectively, a temperature drop of 0.4 and 0.8K (Fig.(5.17)). By observing the formulation of the three models, the Ranz and Marshall model [5] and the Oresta model [6] are dependent on bubble Prandt number and on bubble Reynolds number (Eq.(5.7)-(5.8)). Unlike Ranz and Marshall model, Oresta model presents also the dependency on bubble temperature, by means of the Jacob number. In the last model, the h_b coefficient is dependent on the bubble pressure corresponding at bubble temperature, and there is not a relation with the bubble Reynolds number (Eq.(5.7)). Probably, in condition of cavitating cryogenic flow, the bubble Reynolds number represents a limit factor for the models that, however, have been tested mainly in natural convection,

5.4. RESULTS AND DISCUSSION

where there is not a temperature drop and a difference of velocity high as in cavitating flows.

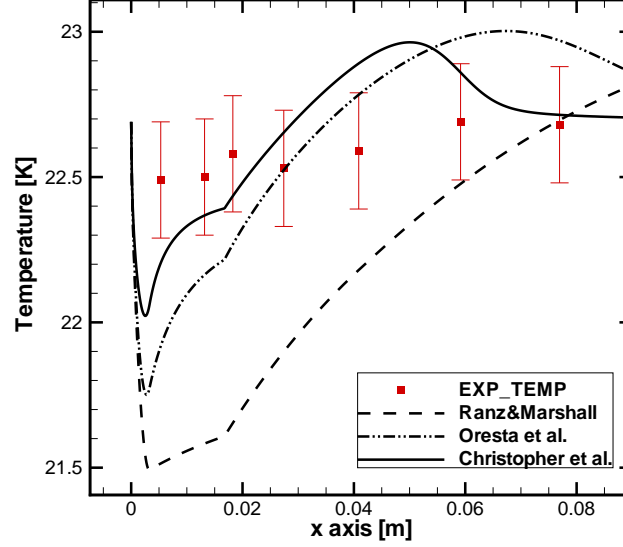


Figure 5.17: Comparison between bubble temperature T_b , obtained with the Ranz& Marshall [5], Oresta *et al.* [6], Christopher *et al.* [7] model, and experimental temperature for the case 125A, with $Re = 6.2 \times 10^{+06}$, $\sigma = 1.3$, $Pr = 1.1917$, $T_0 = 22.69$ and $\alpha_0 = 5 \times 10^{-04}$

5.4.3 Ansys-Fluent Results

The case 121B [1] has been simulated by means of Fluent in order to verify the results and remarks obtained in the previous analysis. A 2D mesh has been used and complex Eulerian model (with respect to 1D code) has been considered. Also in 2D results, the temperature profiles obtained with the Ranz and Marshall model [5] gives an over-estimation of temperature drop in the throat as in the case 1D, while the Christopher model [7] gives a perfect estimation of temperature compared to experimental data (Fig.(5.29)). The profiles estimated with the 2D code have a better prediction of physical phenomenon, however they have the same behavior in the throat observed in 1D results. In fact also the value of h_b estimated in 2D simulations are comparable to the values founded in 1D case (Fig.(5.30)). Then in order to

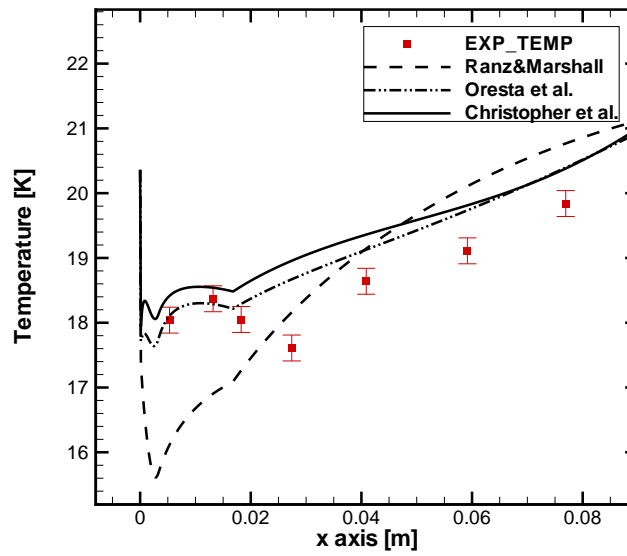


Figure 5.18: Comparison between bubble temperature T_b , obtained with the Ranz&Marshall [5], Oresta *et al.* [6], Christopher *et al.* [7] model, and experimental temperature for the case 120B, with $Re = 7.6 \times 10^{+06}$, $\sigma = 1.3$, $Pr = 1.2541$, $T_0 = 20.36$ and $\alpha_0 = 2 \times 10^{-04}$

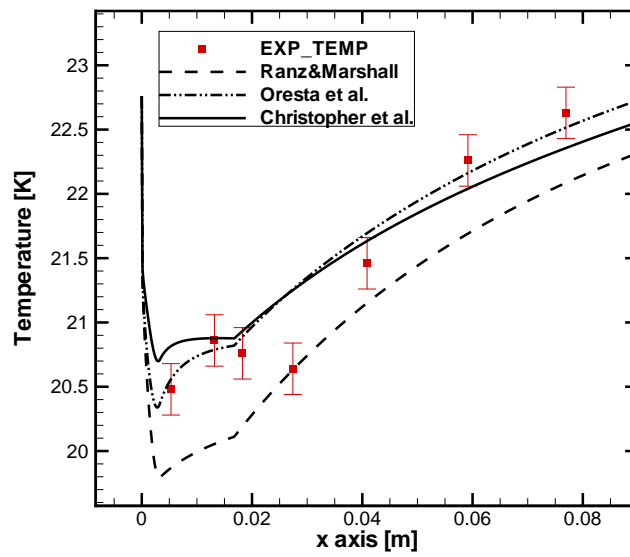


Figure 5.19: Comparison between bubble temperature T_b , obtained with the Ranz&Marshall [5], Oresta *et al.* [6], Christopher *et al.* [7] model, and experimental temperature for the case 123B, with $Re = 6.2 \times 10^{+06}$, $\sigma = 1.3$, $Pr = 1.1917$, $T_0 = 22.69$ and $\alpha_0 = 4 \times 10^{-05}$

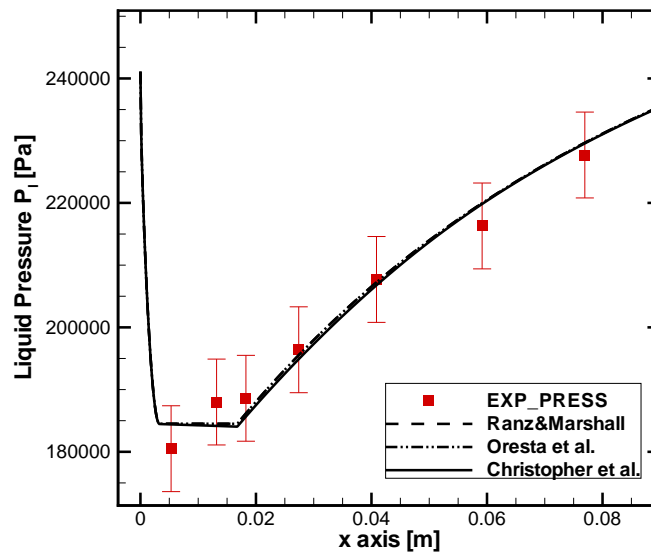


Figure 5.20: Comparison between liquid pressure P_l , obtained with the Ranz&Marshall [5], Oresta *et al.* [6], Christopher *et al.* [7] model, and experimental temperature for the case 125A, with $Re = 6.2 \times 10^{+06}$, $\sigma = 1.3$, $Pr = 1.1917$, $T_0 = 22.69$ and $\alpha_0 = 5 \times 10^{-04}$

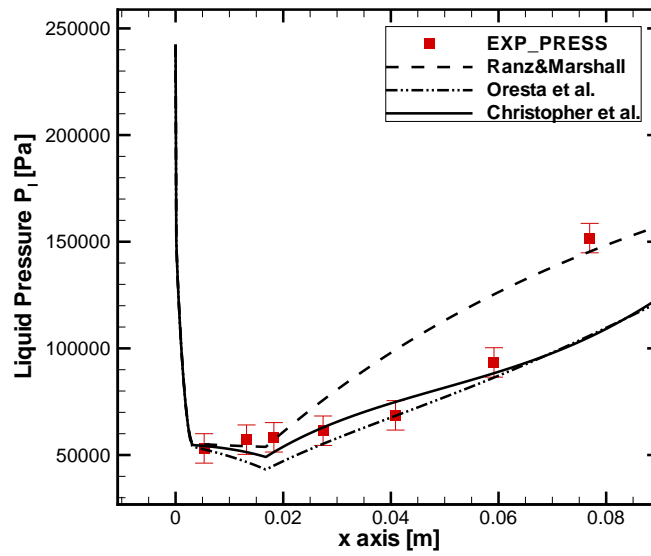


Figure 5.21: Comparison between liquid pressure P_l , obtained with the Ranz&Marshall [5], Oresta *et al.* [6], Christopher *et al.* [7] model, and experimental temperature for the case 120B, with $Re = 7.6 \times 10^{+06}$, $\sigma = 1.3$, $Pr = 1.2541$, $T_0 = 20.36$ and $\alpha_0 = 2 \times 10^{-04}$

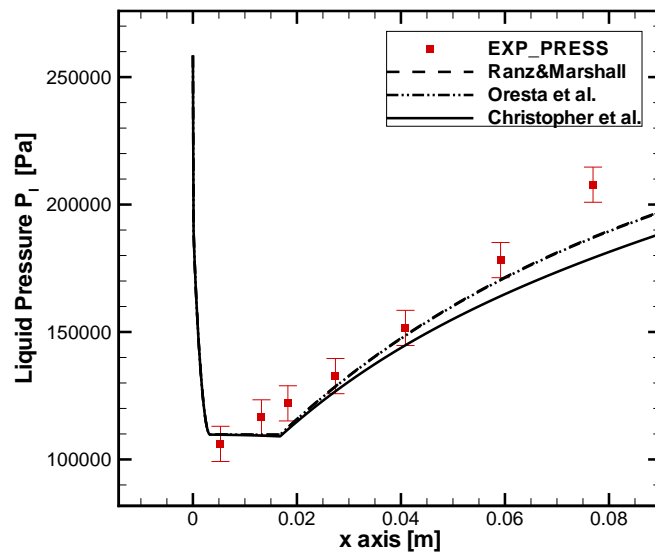


Figure 5.22: Comparison between liquid pressure P_l , obtained with the Ranz&Marshall [5], Oresta *et al.* [6], Christopher *et al.* [7] model, and experimental temperature for the case 123B, with $Re = 6.2 \times 10^{+06}$, $\sigma = 1.3$, $Pr = 1.1917$, $T_0 = 22.69$ and $\alpha_0 = 4 \times 10^{-05}$

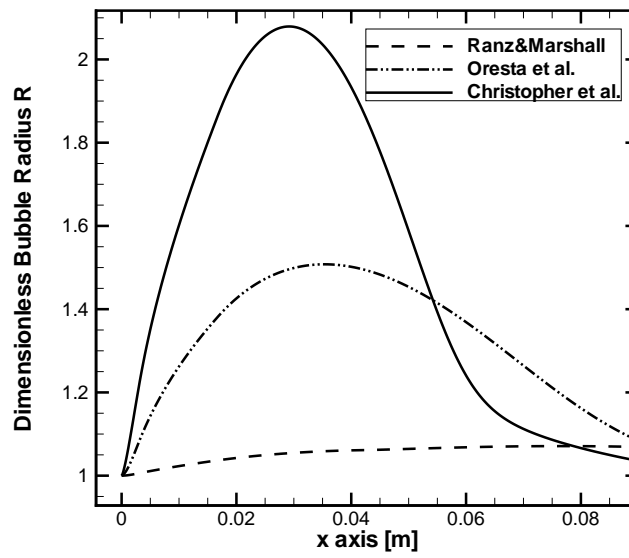


Figure 5.23: Comparison between bubble radius, obtained with the Ranz&Marshall [5], Oresta *et al.* [6], Christopher *et al.* [7] model, and experimental temperature for the case 125A, with $Re = 6.2 \times 10^{+06}$, $\sigma = 1.3$, $Pr = 1.1917$, $T_0 = 22.69$ and $\alpha_0 = 5 \times 10^{-04}$

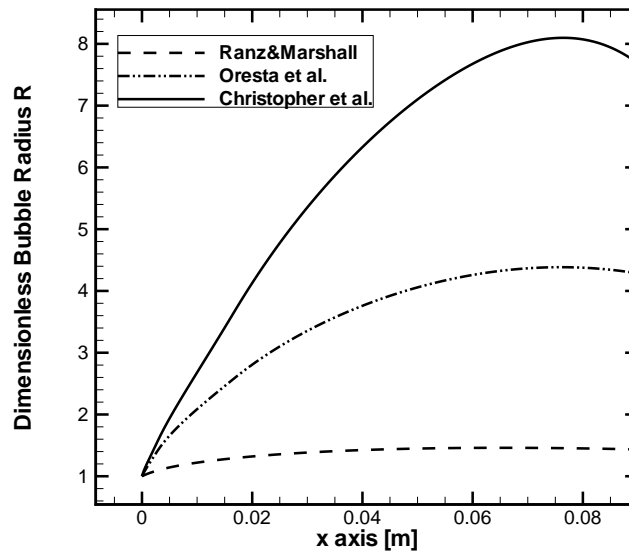


Figure 5.24: Comparison between bubble radius, obtained with the Ranz&Marshall [5], Oresta *et al.* [6], Christopher *et al.* [7] model, and experimental temperature for the case 120B, with $Re = 7.6 \times 10^{+06}$, $\sigma = 1.3$, $Pr = 1.2541$, $T_0 = 20.36$ and $\alpha_0 = 2 \times 10^{-04}$

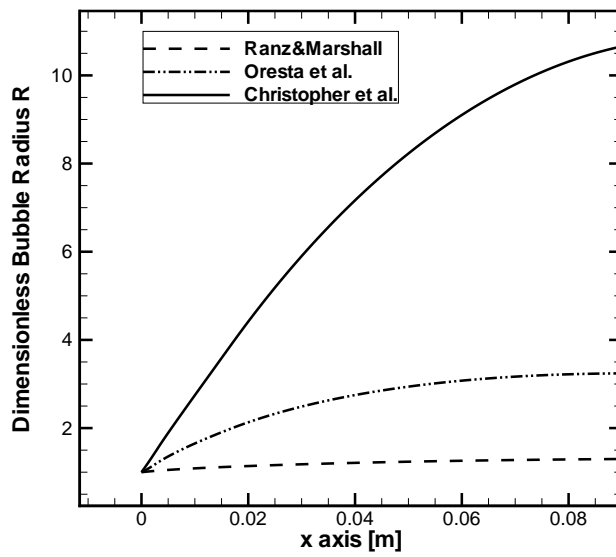


Figure 5.25: Comparison between bubble radius, obtained with the Ranz&Marshall [5], Oresta *et al.* [6], Christopher *et al.* [7] model, and experimental temperature for the case 123B, with $Re = 6.2 \times 10^{+06}$, $\sigma = 1.3$, $Pr = 1.1917$, $T_0 = 22.69$ and $\alpha_0 = 4 \times 10^{-05}$

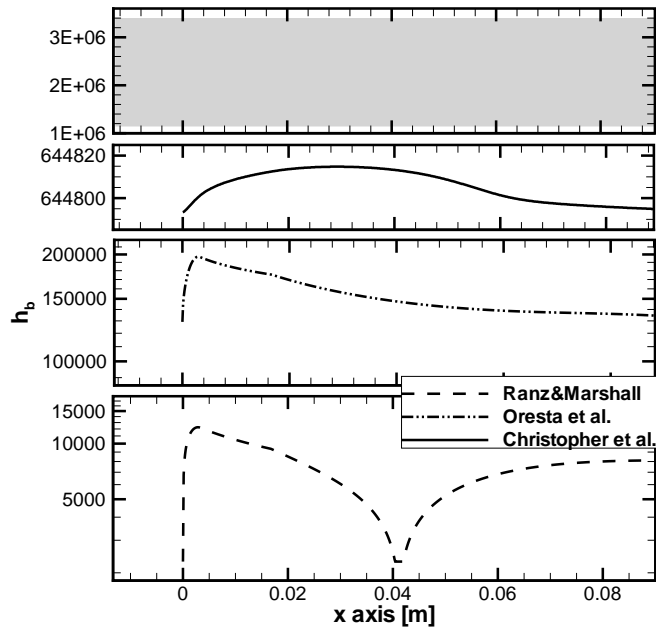


Figure 5.26: Comparison between convective heat transfer coefficient h_b , obtained with the Ranz&Marshall [5], Oresta *et al.* [6], Christopher *et al.* [7] model, and experimental temperature for the case 125A, with $Re = 6.2 \times 10^{+06}$, $\sigma = 1.3$, $Pr = 1.1917$, $T_0 = 22.69$ and $\alpha_0 = 5 \times 10^{-04}$

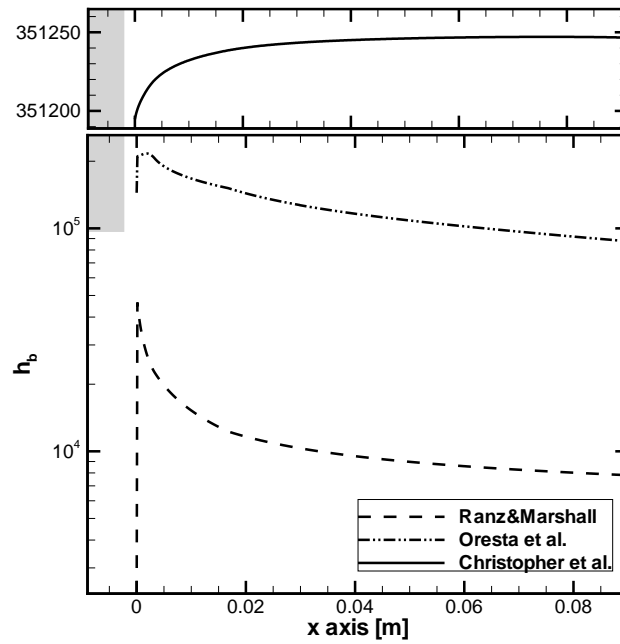


Figure 5.27: Comparison between convective heat transfer coefficient h_b , obtained with the Ranz&Marshall [5], Oresta *et al.* [6], Christopher *et al.* [7] model, and experimental temperature for the case 120B, with $Re = 7.6 \times 10^{+06}$, $\sigma = 1.3$, $Pr = 1.2541$, $T_0 = 20.36$ and $\alpha_0 = 2 \times 10^{-04}$

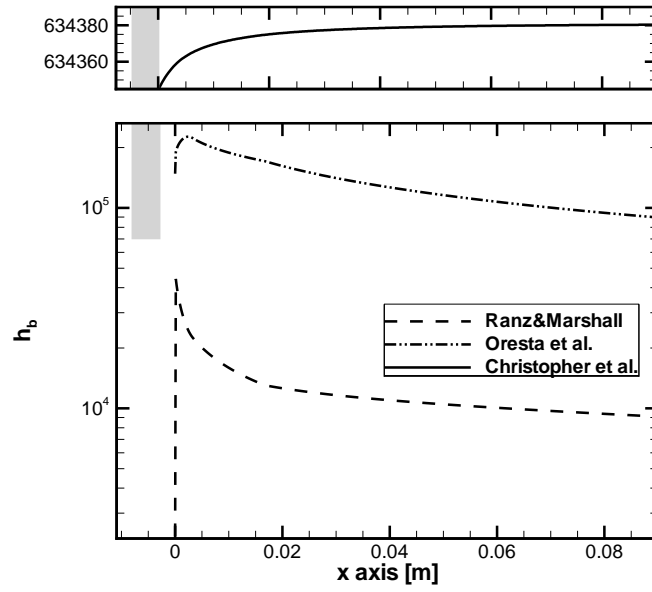


Figure 5.28: Comparison between convective heat transfer coefficient h_b , obtained with the Ranz&Marshall [5], Oresta *et al.* [6], Christopher *et al.* [7] model, and experimental temperature for the case 123B, with $Re = 6.2 \times 10^{+06}$, $\sigma = 1.3$, $Pr = 1.1917$, $T_0 = 22.69$ and $\alpha_0 = 4 \times 10^{-05}$

5.4. RESULTS AND DISCUSSION

obtain a good prediction of temperature drop, it is necessary an estimation of $h_b > 4 \times 10^5$ as founded in the sensitivity analysis at constant h_b (grey rectangular in Fig.(5.30)) It is possible to observe that, for $x > 0.06m$, the two temperature profiles, obtained with 2D code, give the same levels of temperature as well as the h_b profiles becomes constant. Analyzing the mass transfer contour (Fig.(5.31)), in the region where $x > 0.06m$, it is possible to observe the phase of condensation of the bubble (Fig.(5.31)). Then, the importance of convective heat transfer coefficient estimation is more evident in the phase of evaporation, while it is negligible when the bubble collapse. Finally, as observed in the 1D simulation, by estimating an h_b more elevated, the Christopher model [7] is able to predict a vapor fraction more elevated than the Ranz and Marshall model [5]; however the difference is less evident than in 1D simulation (Fig.(5.32)).

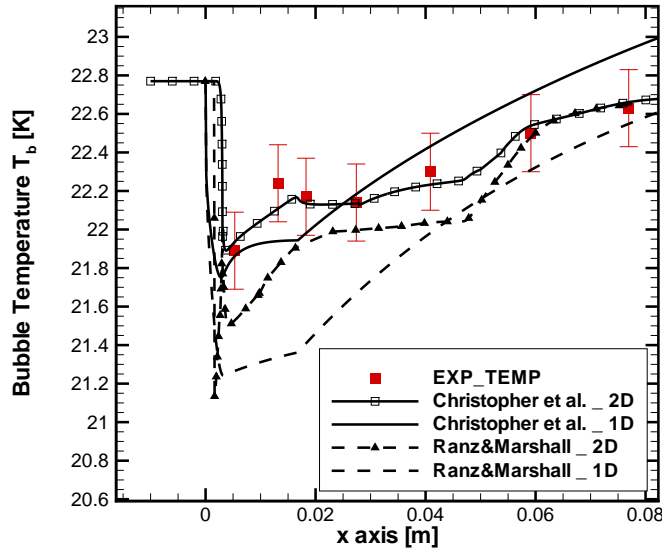


Figure 5.29: Comparison between temperature profiles, obtained with the Ranz&Marshall [5] and Christopher *et al.* [7] model and with 1D and 2D code for the case 121B [1] with $\alpha_0 = 1 \times 10^{-04}$ and initial radius $R_0 = 1 \times 10^{-04}m$. The experimental temperature error is of $\pm 0.1K$.

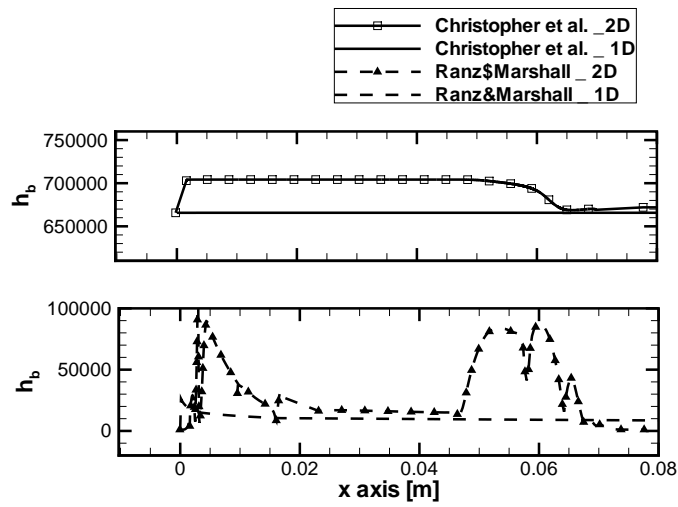


Figure 5.30: Comparison between convective heat transfer coefficient, obtained with the Ranz&Marshall [5] and Christopher *et al.* [7] model and with 1D and 2D code for the case 121B [1] with $\alpha_0 = 1 \times 10^{-4}$ and initial radius $R_0 = 1 \times 10^{-4}m$. The experimental temperature error is of $\pm 0.1K$.

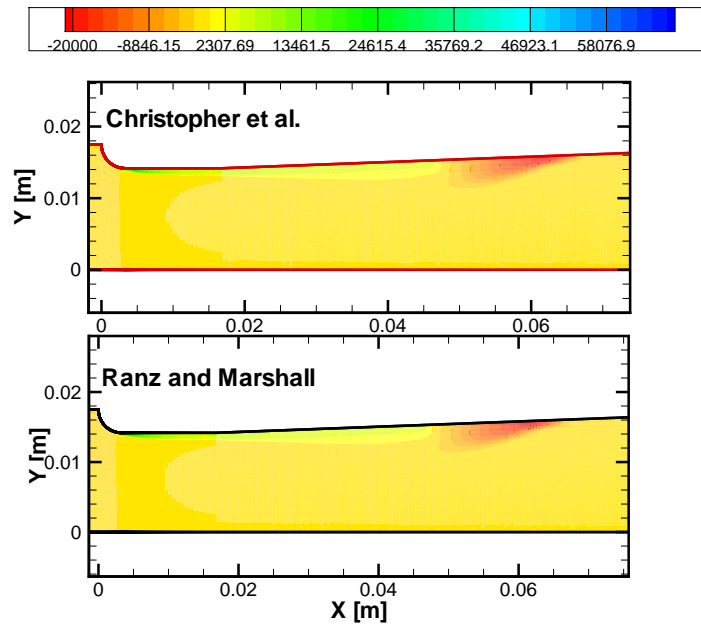


Figure 5.31: Comparison between the contour of mass transfer, obtained with the Ranz&Marshall [5] and Christopher *et al.* [7] model in 2D code for the case 121B [1] with $\alpha_0 = 1 \times 10^{-04}$ and initial radius $R_0 = 1 \times 10^{-04}m$. The experimental temperature error is of $\pm 0.1K$.

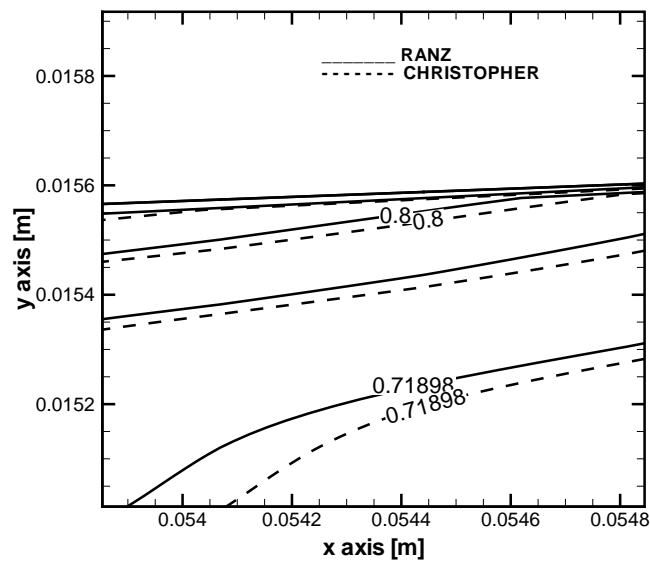


Figure 5.32: Comparison of vapor contour, obtained with the Ranz&Marshall [5] and Christopher *et al.* [7] model in 2D code for the case 121B [1] with $\alpha_0 = 1 \times 10^{-04}$ and initial radius $R_0 = 1 \times 10^{-04}m$. The experimental temperature error is of $\pm 0.1K$.

5.5 Conclusions

The present section has the objective to analyze the thermal effects in a cryogenic cavitating flow, through the study of convective heat transfer coefficient h_b . The work is divided in two parts consisting in a first analysis of sensitivity at constant h_b , followed by an analysis about several models for a more correct estimation of h_b , both performed by a 1D code. In the second part, a comparison between the 1D results and the 2D results obtained with the commercial code Fluent has been performed. For the 1D code, the cavitating flow is modeled by steady-state mixture model that reproduces the operating conditions of experimental cases in a Venturi tube[1]. It consists in conservative equations of continuity and momentum equations of the bubbly flow, coupled with a Rayleigh-Plesset equation in order to predict the cavitation development and with a bubble momentum equation to predict the bubble velocity. The thermal effects are taken into account considering a term in Rayleigh-Plesset in which the vapor pressure is computed at the bubble temperature, which is different from the liquid temperature far from the bubble. In this term, the convective heat transfer coefficient h_b appears. In literature there is not a complete study permitting to estimate the value to consider for this parameter in cryogenic cavitating fluids. A wrong value can generate a bad estimation of thermal effects. For the 2D code, numerical simulations have been performed using the multiphase cavitation modeling approach. It consists in the use of standard viscous flow equations governing the transport of phases (Eulerian multiphase), a $k - \varepsilon$ turbulent model and a model to estimate the liquid-vapor mass transfer due to cavitation phenomenon. Continuity, momentum and energy equations are solved for each phase. The mass transfer term is modeled by Schnerr and Sauer model [73]. A sensitivity analysis of the convective heat transfer coefficient, in cryogenic cavitation, has been performed in order to identify the mechanisms that govern the bubble growth. For all tested cases the coefficient h_b varied between 1×10^{10} and 1×10^{03} and for each h_b , the upstream vapor fraction α_0 varied between 1×10^{-10} and 1×10^{-03} . In order to analyze qualitatively the results, for each case, three parameters have been identified, h_{bMAX} , h_{bOPT} and h_{bMIN} , that represent respectively the minimal value for which the growth is governed exclusively by mechanical forces, the range of values permitting to obtain the best profiles of temperature and pressure with respect to experimental data and the maximum value for which the growth is governed exclusively by thermal effects. Then three models for convective heat trans-

5.5. CONCLUSIONS

fer coefficients prediction have been analyzed, the Ranz and Marshall model [5], Oresta model [6] and Christopher model [7]. Finally, in order to validate the results obtained with the in-house code, 121B case [1] have been simulated also with Fluent. The main conclusions of the present section are the following:

- An over-estimation of h_b determines that the bubble growth is governed by mechanical forces producing an increase of vapor fraction and a negligible temperature drop in the throat. On the contrary, an under-estimation determines that the bubble growth is governed by thermal force producing a good estimation of temperature drop, even if the vapor fraction increases not sufficiently
- In all the simulated cases h_b is close to h_{bMIN} value, confirming that in hydrogen cavitating flow the growth of bubbles is more controlled by the thermal effect than the mechanical force
- There is an optimal range for hydrogen cavitating flow that is about $1 \times 10^{05} < h_b < 1 \times 10^{06}$, then it is better to use a model for the estimation of h_b coefficient
- The optimal value of h_b is more influenced by inlet temperature T_0 and by σ , than Reynolds number
- By comparing the three models, it can be observed that the Oresta and Christopher model give a good estimation of temperature drop. The Ranz and Marshall model gives an error more elevated compared to the other two model in terms of temperature drop in the throat
- By comparing Fluent results with the others, it can be observed that it is very important a good estimation of h_b and that the choice of the model is more evident in the phase of evaporation, while it is negligible when the bubble collapse, because the two models give the same temperature results.

Second Part: Experimental Study

Chapter 6

Experimental Study on Two-Phase Cryogenic Flow

6.1 Experimental Nucleation in Cavitating Flow

For cryogenic flows, cavitation phenomenon is similar to boiling. Generally, these two processes can be distinguished by the fact that cavitation is the process of nucleation in a liquid when the pressure falls below the saturated vapor pressure, while the boiling is the process of nucleation that occurs when the temperature is raised above the saturated vapor temperature. In cryogenic flows, there is a lack of experimental investigations in literature. In aerospace field, cryogenic fluids are usually used as rocket propellant obtained as mixture of liquid oxygen (LOx) and liquid hydrogen (LH2). These fluids can be employed under particular conditions as low temperature, microgravity and the environmental space, but they can be associated to cavitation phenomena, because a slight difference of temperature could induce a transition of phase. The aim of this work is to examine the results of a flow visualization study on two-phase cryogenic flows passing through an internal nozzle. The transient growth process of the cloud cavitation induced by flow through the throat is observed using high-speed video images and analyzed by pressure and accelerometer signal.

6.1.1 Experimental Set-Up

A schematic illustration of the experimental set-up, used to investigate the internal nozzle flow, is shown in Fig.(6.1) and Fig.(6.2). The liquid nitrogen

6.1. EXPERIMENTAL NUCLEATION IN CAVITATING FLOW

has been chosen as the cryogenic working fluid. The set-up consists of a nitrogen supply tank, at a temperature of 77 K, two on-off valves and a flow visualization test section. A global view of the entire test section (bulk flow) is given in Fig.(6.12). The test section is an assembly of a central internal nozzle, in which the fluid flows; two vacuum chambers, for the thermal isolation and two flanges. In order to perform the continuous monitoring of cavitation phenomenon, 4 quartz glass are fitted between the assembly components. The supply tank is connected to the visualization chamber by a 2m long pipe. Geometrical details of the flow channel are shown in Fig.(6.4). The test section is a 15mm long rectangular orifice nozzle with a throat cross section 2mm by 8mm. After the visualization chamber, the nitrogen liquid is ejected in atmosphere as gas. The line is filled with pressurized cryogenic liquid at a pressure of 2 bar and flow immediately occurred when the first on-off valve after the nitrogen pressure tank is opened. The cavitation phenomenon can be observed within the flow, at a certain flow rate, in the throat section. If the pressure is below the vapor pressure at the flow temperature, cavitation occurs. The acquisition and data elaboration system is based on:

- Two KISTLER 701A piezoresistive pressure sensors, with a sensitivity of $-80pC/bar$ and a temperature range of $-190/200C$. They are placed according to Fig.(6.4).
- A KISTLER piezoresistive amplifier, used for pressure signals
- A NI-DAQCard-6024E acquisition board at $200KS/s$, used for the pressure signals.
- A KISTLER 8702B100 accelerometer.
- A NI-DAQCard-6020E acquisition board up to $1.25Ms/s$, used for accelerometer signal.
- A high speed camera CCD Kodak Motion Corder Analyzer FASTCAM-Super 10k.

The images have been acquired at $125fps$ and then have been downloaded and stored on a PC to be subsequently processed digitally. For the different test-cases, the pressure and accelerometer signals have been acquired at a maximum frequency of $100kHz$ and 10^5 samples, for a total data period of 1s. Then the signals have been amplified, filtered and collected into the two

6.1. EXPERIMENTAL NUCLEATION IN CAVITATING FLOW

boards. The voltage working range, for our test-cases, was between $-2V$ and $2V$; it has been possible to obtain a gain in order to acquire also a minimum voltage variation of $2.44mV$. The acquisition programs have been developed in-situ using the software Labview and the signal processing code has been developed using MATLAB software. Part of the uncertainty is inherent to the flow conditions: the flow velocity, the pressure in the test section, the cavitation number. The uncertainty on the pressure is about 3%. The resulting cavitation number variability is estimated to be ± 0.05 . For the pressure transducers calibration, the deviation toward linearity was about $250Pa \sim 0.25\%$ of the measurement range. The test conditions are summarized in Tab.6.1.



Figure 6.1: Experimental Set-Up

6.1.2 Results

The aim of these experiments is to characterize the cavitating cryogenic flow in term of time occurrence, space, and intensity for various hydrodynamic conditions. The experimental methods used in the study are:

- Accelerometer measurements
- Upstream and downstream pressure measurements
- Optical observations (CCD)

6.1. EXPERIMENTAL NUCLEATION IN CAVITATING FLOW

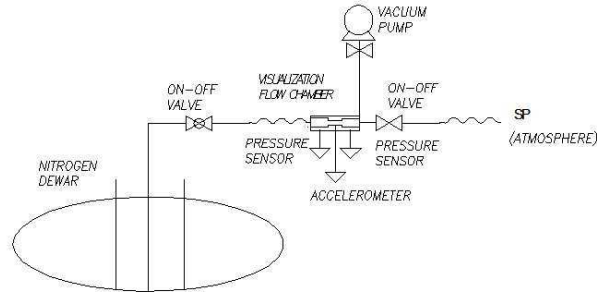


Figure 6.2: Sketch of the Experimental Set-up

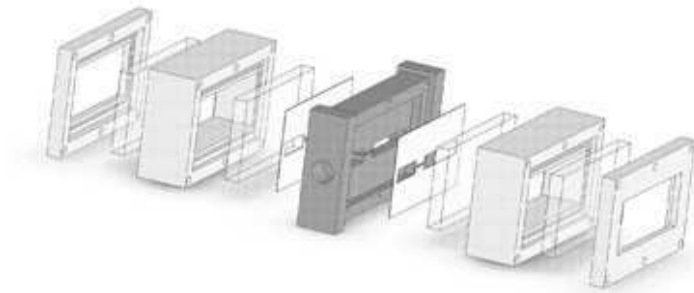


Figure 6.3: Visualization flow test section.

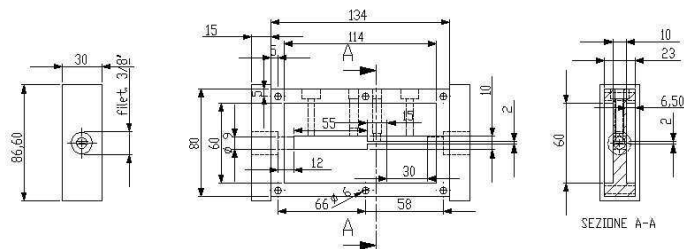


Figure 6.4: Test section particular.

6.1. EXPERIMENTAL NUCLEATION IN CAVITATING FLOW

Test Case	Upload Pressure [bar]	Download Pressure [bar]	$Q[m^3/s]$	σ
1	1.08	1.0015	0.0011	1.364
2	1.49	1.0226	0.0008	1.104
3	1.77	1.0234	0.0006	1.066
4	2.04	1.0223	0.0003	1.047
5	2.05	1.0236	0.0002	1.034
6	0.95	0.9320	0.0011	0.990
7	1.06	0.9275	0.0010	0.986
8	1.35	0.9216	0.0008	0.980
9	1.80	0.9177	0.0005	0.977
10	2.01	0.9167	0.0004	0.976

Table 6.1: Operating conditions of experimental case

A number of experiments have been carried out in order to determine the characteristics of the cavity length at different cavitation numbers defined as:

$$\sigma = [(p_{up} - p_v)/(p_{up} - p_{dw})] \quad (6.1)$$

where p_{up} and p_{dw} are, respectively, the upstream and the downstream pressure. The p_v is the vapor pressure at the flow temperature, that, for the test-cases, is considered as the Dewar temperature, then $T = 77K$, and consequently $p_v = 0.9744bar$. The acquired signals have been studied in time domain and frequency domain, in order to obtain information correlated to the cavitation phenomena. It is well known that cavitation inception in a liquid is due to the explosive growth of microscopic bubbles or nuclei initially present in the liquid; the inception of cavitation happens when the local pressure drop below a critical low pressure. The determination of the number of these nuclei is important to control the phenomena and to validate the numerical modeling. The vapor bubbles contain non-condensable gas and vapor, then it is assumed that both sides of the bubble interface is in thermodynamic equilibrium [75]:

$$p_g + p_v = p_\infty + (2S/R) \quad (6.2)$$

6.1. EXPERIMENTAL NUCLEATION IN CAVITATING FLOW

where p_g and p_∞ are, respectively, the pressure of non condensable gas and the liquid pressure, while S is the surface tension and R is the bubble radius. Considering that the p_g can be re-written in function of bubble radius and a K factor, that is proportional to the mass of non condensable gas, an equilibrium curve can be defined, characterized by a minimum point denominated "critical point" with the following values of pressure and radius:

$$R_c = \sqrt{\frac{3K}{2S}} \quad (6.3)$$

$$p_c = p_v - \frac{4S}{3R_c} \quad (6.4)$$

If the nuclei undergoes a pressure drop below the minimum p_c , it also grows indefinitely without reaching a new equilibrium and form a cavitation bubble. When these bubbles travel across a high pressure zone, they implode with a correspondent local maximum in the pressure signal. For this reason from temporal analysis, it has been possible to count the concentration of nuclei Fig.(6.5), during their transit through the nozzle, at different cavitation number. It is possible to observe a higher density of nuclei for lower cavitation number, because the liquid pressure is low, that allows the bubble growing and collapsing. Also the standard deviation of the downstream pressure signal (Fig.(6.6)) shows a higher oscillation for lower number cavitation, less than 1. It seems that the cavitation number $\sigma = 0.99$ is a critical value, below that value the cavitation increases, showing an high number of activated nuclei and then an higher standard deviations. The pressure signals, measured upstream and downstream of the contraction area in the orifice, and the accelerometer signal, have been processed to calculate the characteristic frequency content of the aforementioned signals. The formation of cavitation bubbles and their collapse generate observable pressure fluctuations. The Fast Fourier Transform of the measured signals was carried out considering the pressure fluctuations components around the time integrated mean value. In Fig.(6.7), Fig.(6.8) and Fig.(6.9) the amplitude spectrum of Fourier Transform of upstream and downstream pressure and of accelerometer are shown at different flow conditions (different cavitation number, σ). The complete development of cavitation phenomenon can be related to fluctuations measured before and after the throat. It is noticeable that for the upstream flow the main frequency content is in the range of low frequencies, up to $500Hz$, especially for low cavitation number, related to the impacts

6.1. EXPERIMENTAL NUCLEATION IN CAVITATING FLOW

due to the vapor bubbles implosion. The frequency spectrum of the downstream pressure signals can be related to the characteristic behavior of the different cavitating regimes. In fact, the spectra show different characteristic frequencies with the variation of the cavitation number. At higher cavitation numbers, the spectra reveal relatively high dominant frequencies distributed in broad ranges of few hundred Hertz width. At lower cavitation numbers, less than 1, the spectra show sharp dominant spectral peaks also at higher frequencies. The increase of some typical frequency component amplitudes, at small cavitation number is related to a sharp increase in the length of the cavitating zone, as evident also by the flow visualization by the CCD (Tab.(6.2)).

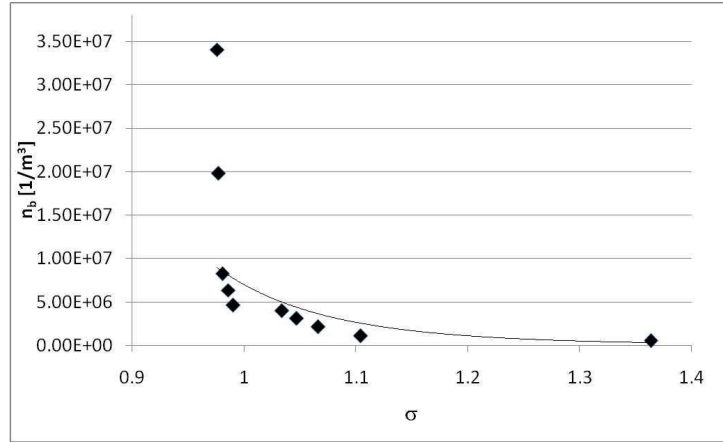


Figure 6.5: Distribution of density of activated nuclei density for different cavitation numbers.

In particular, a characteristic frequency is found at values close to $400Hz$; peaks at this frequency are present only in the downstream pressure signals and not at the upstream section. The amplitude peaks at this frequency has an increasing behavior at low cavitation numbers, as shown in Fig.(6.10). For the accelerometer signal, it is not possible to locate a range of frequencies, probably due to the high implosion intensity. Starting from the amplitude spectrum of Fourier Transform, it is interesting to calculate the function $S(f_1 - f_2)$:

$$S(f_1, f_2) = \int_{f_1}^{f_2} s(f)df. \quad (6.5)$$

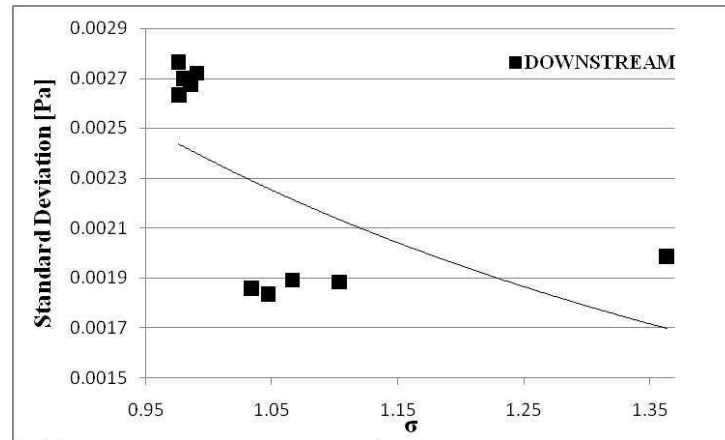


Figure 6.6: Standard deviation of downstream pressure signals for different cavitation numbers

This equation represents the area between the spectrum and the frequency axis and between the f_1 and f_2 frequencies. Then it is possible to confirm the FFT spectrum results. In fact, the Fig.(6.11) shows the $S(0 - 10kHz)$ function for the downstream pressure signal at different cavitation numbers; it is evident that an increase of areas corresponds to a decrease of cavitation number.

6.1.3 Conclusions

Some experimental results on the cavitation of cryogenic fluids have been presented. In particular, a flow visualization and pressure measurements on two-phase cryogenic flow passing through an orifice nozzle installed in a horizontal pipe has been carried out in order to clarify the fundamental characteristics of the cavitating structures. Pressure signals have been analyzed both in time domain and in frequency domain, to characterize the cavitating cryogenic flow in terms of time occurrence, space, and intensity for various hydrodynamic conditions. The concentration of activated bubbles nuclei has been obtained, this could be useful for modeling validations. An increase of nuclei due to a decrease of cavitation number has been observed. Then the standard deviation of the pressure signals, recorded downstream the restricted nozzle area has been studied in order to obtain an evaluation

6.1. EXPERIMENTAL NUCLEATION IN CAVITATING FLOW

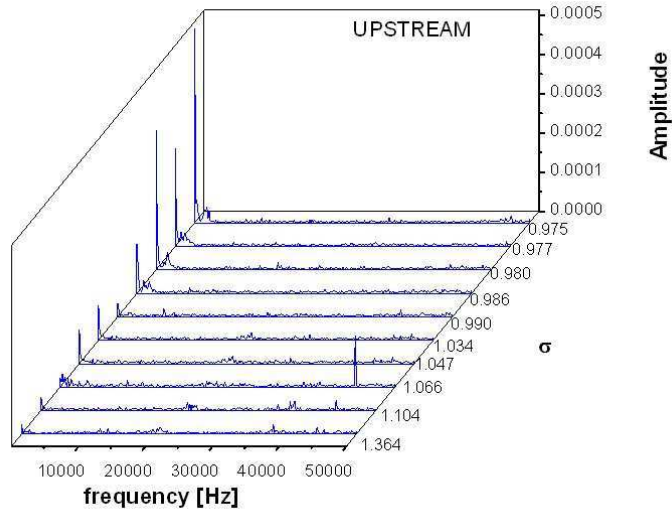


Figure 6.7: FFT Amplitude Spectrum of the upstream pressure for different cavitation numbers

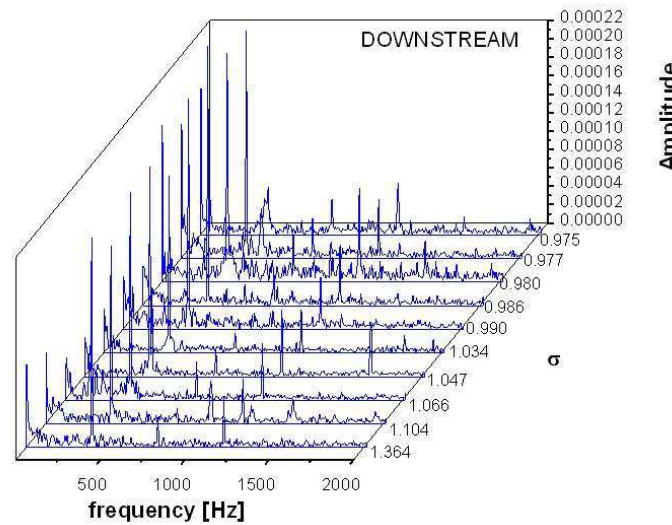


Figure 6.8: FFT Amplitude Spectrum of the downstream pressure for different cavitation numbers.

6.1. EXPERIMENTAL NUCLEATION IN CAVITATING FLOW

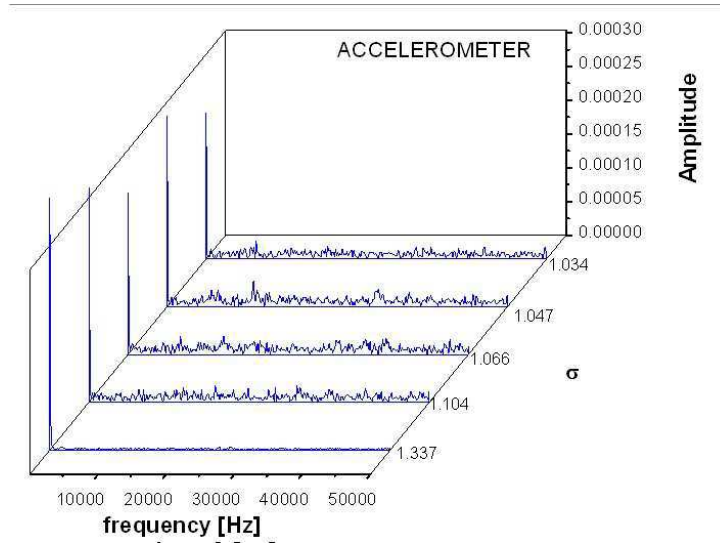


Figure 6.9: FFT Amplitude Spectrum of accelerometer for different cavitation numbers.

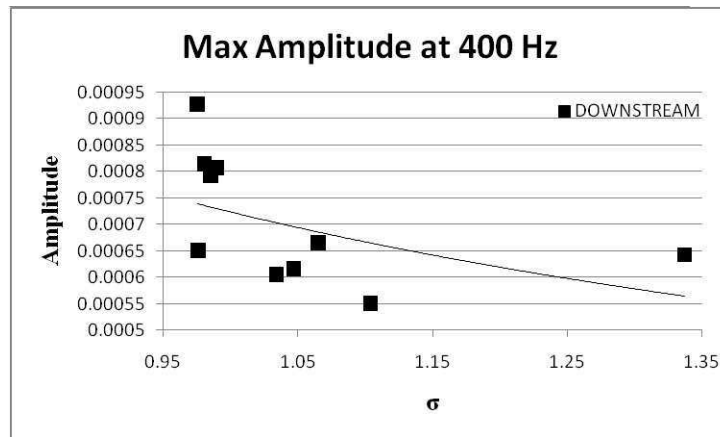


Figure 6.10: Maximal Amplitude obtained at 400Hz of downstream pressure signal at different cavitation numbers.

6.1. EXPERIMENTAL NUCLEATION IN CAVITATING FLOW

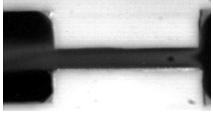
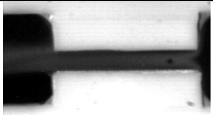
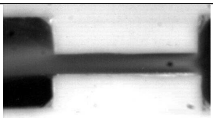
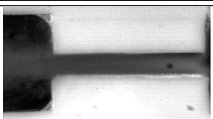
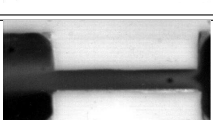
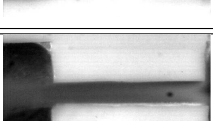
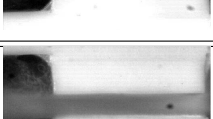
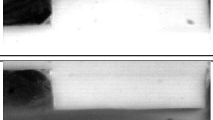
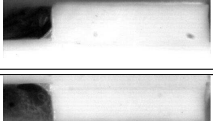
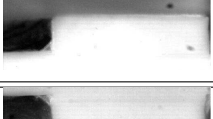
Test Case	<i>Vapor Production</i>	σ
1		1.364
2		1.104
3		1.066
4		1.047
5		1.034
6		0.990
7		0.986
8		0.980
9		0.977
10		0.976

Table 6.2: Flow visualizations at different cavitation numbers σ .

6.2. EXPERIMENTAL THERMAL EFFECT IN WATER AND CRYOGENIC CAVITATING FLOW

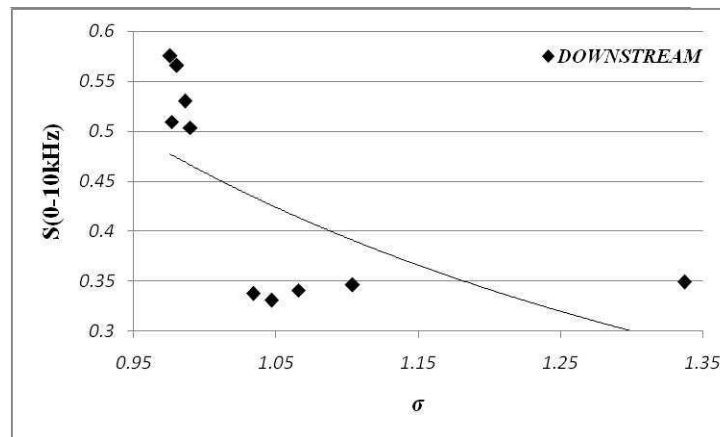


Figure 6.11: $S(0 - 10kHz)$ function for the downstream pressure signal at different cavitation numbers.

about the oscillation of pressure signals due the development of cavitation. By means of the Fourier Transform, it has been possible to locate a range of characteristic frequencies for the upstream pressure and downstream pressures.

6.2 Experimental Thermal Effect in Water and Cryogenic Cavitating Flow

Here, an experimental study has been presented that focused on the formation of cavitation in cold and hot water and in cryogenic fluid, characterized by strong variations in fluid properties caused by a change in temperature. Cavitation phenomenon is investigated in water and nitrogen flows in a convergent-divergent nozzle through pressure measurements and the optical visualization method. High-speed photographic recordings have been made, the cavitation phenomena evolution and the related frequency content are investigated by means of pixel intensity time series data. In the case of cryogenic fluid frequency peaks are shifted towards lower frequencies, with respect to cold water and the magnitude of the signal increases, in particular at low frequencies, for nitrogen and hot water. This can be due to thermal effects that contribute also to the low frequencies in the case of cryogenic

6.2. EXPERIMENTAL THERMAL EFFECT IN WATER AND CRYOGENIC CAVITATING FLOW

fluid. To verify the validity of this assumption, a simple model based on the resolution of Rayleigh equation is used.

6.2.1 Experimental Set-Up

The cavitating flow in nitrogen and in water has been investigated in the same convergent-divergent nozzle. The experimental set-up for the two fluids is different, due to the methods of storage and usage of the fluids. The test section is an assembly of a central internal nozzle in which the fluid flows, two vacuum chambers, for the thermal isolation and two flanges. In order to perform the continuous monitoring of cavitation phenomena, plexiglas windows are fitted between the assembly components. Geometric details of the flow channel are shown in Fig.(6.12). The experimental set-up is shown in Fig.(6.13) and Fig.(6.14). In the water facility, the flow is driven by a $1.10kW$ centrifugal pump (model CR 4-50 A-A-A BUBE) , $2900rpm$, with five impellers, capable of a maximum flow rate of $1.67 \times 10^{-3}m^3/s$, located $1m$ below the test section, in order to prevent cavitation occurrence in the pump. Two Kistler 4045A piezoresistive pressure sensors have been placed. The uncertainty in the pressure measurements is $\pm 3kPa$. Another pressure sensor, the KISTLER 701A, is instead put at the throat of the section, where a KISTLER 8702B100 accelerometer is also installed. The pressure sensors have been coupled to a NI-4472 Dynamic Signal Acquisition Device for PCI (up to $102.4ks/s$ with two pole anti-alias low-pass filter for each input channel) to which the pressure sensors are connected through a Kistler type 4643 piezoresistive amplifier, accuracy 0.5%. The analogue signals are acquired at a sampling rate of $102kHz$, for each channel. The mass flow rate through the test section, and then the pressure upstream of the test section, has been varied by means of two calibrated control valves (control valve 1 and 2 in Fig.(6.13)). In particular, a variable portion of the water flow is by-passed from the test section directly to the intake of the pump by means of control valve 1; control valve 2 is used to modify the upstream pressure. The set-up of nitrogen facility consists of a nitrogen supply tank, at a temperature of $-193C$ and two on-off valves. The supply tank is connected to the test section by a $2m$ long pipe. The line is filled with pressurized cryogenic liquid at a pressure of $2bar$ and flow immediately occurs when the first on-off valve after the nitrogen pressure tank is opened. The upstream and downstream pressure, in the test section, is measured with KULITE CT-375M cryogenic miniature ruggedized pressure transducers. Instead, the

6.2. EXPERIMENTAL THERMAL EFFECT IN WATER AND CRYOGENIC CAVITATING FLOW

throat pressure is measured with a KULITE CT-190-100A cryogenic miniature ruggedized pressure transducer.

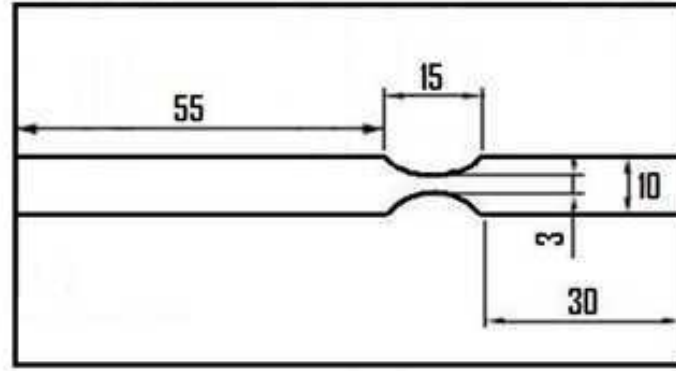


Figure 6.12: Test section for water and nitrogen cavitation experimental analysis. The lengths are in mm and the nozzle depth is 10mm.

6.2.2 Mathematical Model

The in-house CFD model(see Eq.(5.11)-(5.16)), introduced in the chapter 5, has been used for the simulation of same test-case, obtained experimentally, through the convergent-divergent nozzle (Fig. (6.12)). The dimensionless cross-section has been determined to have the minimum value of pressure coefficient, denoted as C_{pMIN} , located at $L/2$ (L is the length of the nozzle) and to result in a sinusoidal pressure distribution:

$$\bar{A}(x) = \begin{cases} \left[1 - \frac{1}{2}C_{pMIN} \left[1 - \cos\left(\frac{2\pi x}{L}\right)\right]\right]^{1/2} & 0 \leq x \leq L \\ 1 & x < 0, x > L \end{cases}$$

The model Ranz and Marshall [5] for the estimation of convective heat transfer coefficient has been used (see Eq.(5.7)).

6.2.3 Results

For the experimental study, two fluids have been considered: liquid nitrogen at a temperature of $T = 82K$; water at $T = 293K$ and $T = 348K$ for

6.2. EXPERIMENTAL THERMAL EFFECT IN WATER AND CRYOGENIC CAVITATING FLOW

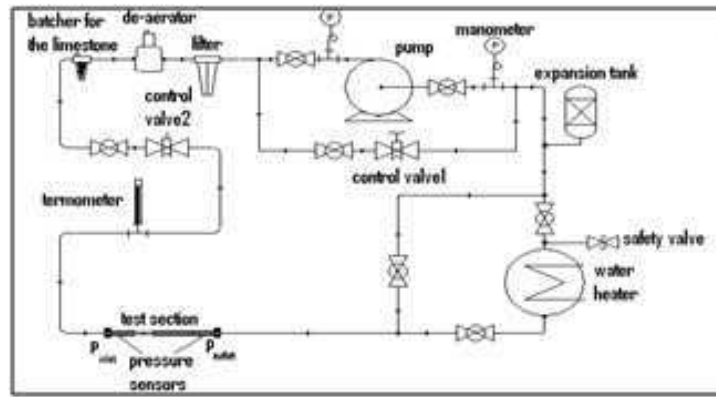


Figure 6.13: Experimental set-up for water cavitation.

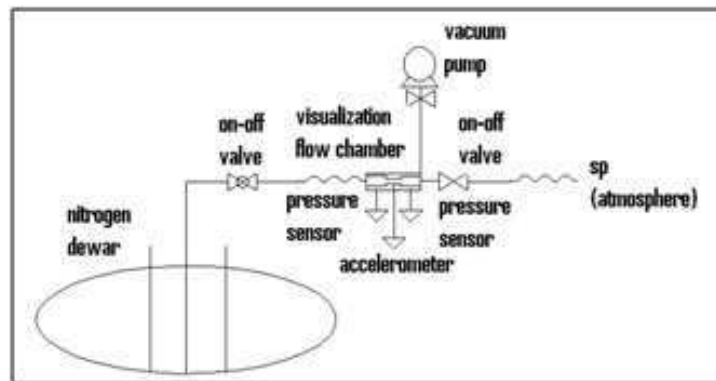


Figure 6.14: Experimental set-up for nitrogen cavitation.

6.2. EXPERIMENTAL THERMAL EFFECT IN WATER AND CRYOGENIC CAVITATING FLOW

different cavitation number. The test section has a well-defined shape, given by Eq.(6.2.2) with a minimum pressure coefficient $C_{pMIN} = 10$, characterized by a throat of $3mm$ and an initial section $A_0 = 100mm^2$, determining an area ratio $A_{throat}/A_0 = 3$. Water cavitation has been analyzed at two different temperatures to observe the thermal effects, that are negligible in room condition. The cavitation numbers obtained for water experiments are higher than in nitrogen experiments, but inception cavitation has been observed for both fluids. A reason for this difference is due to thermal effects, because, as Kikuta et al.[65] studied, the temperature liquid nitrogen, that in this case is of $82K$, is near the critical point ($T_{cNITROGEN} = 126.192K$, $T_{cWATER} = 647.096K$), and then the correspondent vapor density is more elevated that far from the critical point. The consequence is that liquid nitrogen needs more heat to cavitate and so, at the same cavitation number, the water develops a more elevated cavity length [12, 76, 65]. Fig.(6.15) shows the Fourier transformation (FFT) amplitude spectrum of the upstream pressure signals for the nitrogen fluid at $T = 82K$, at different cavitation numbers σ . According to the FFT values, the interesting frequency range for nitrogen experiments spans to no more than $100Hz$ for all the cavitation regime. Fig.(6.16) shows a comparison of frequency spectra obtained from pressure signals for nitrogen ($T = 82K$ and $\sigma = 1.55$) and water at different temperatures ($T = 293K$ and $\sigma = 8.0$; $T = 348K$ and $\sigma = 8.0$). It is evident how frequency peaks are shifted towards higher frequencies in the case of water, as well as the fact that the magnitude of the signal rises, in particular at the low frequencies, with increasing water temperature. This can be due to thermal effects that contribute to the low frequencies in the case of cryogenic fluid. This is confirmed also by the frequency spectrum obtained by the visualizations. Images obtained from visualization are treated using customized software programmed in Matlab. Four series of images, obtained by visualization method, settings for brightness and contrast were constant and equal for all points during the experiment. Although the exact relationship between the size of cavitation and image brightness is not known, certainly the void fraction and thus cavitation size are proportional to the measured pixel brightness. The brightness of each image was calculated by averaging the brightness of the pixels in the image. From brightness values, time series were formed for spectrum analysis. Time series were transformed using fast Fourier transformation (FFT) algorithm into discrete Fourier transform (DFT) so that frequency spectra were obtained. The analysis of figures confirms the trends of frequency spectra obtained from pressures signals, as

6.2. EXPERIMENTAL THERMAL EFFECT IN WATER AND CRYOGENIC CAVITATING FLOW

it is possible to observe in Fig.(6.17) for the nitrogen and in Fig.(6.18) and Fig.(6.19), respectively, for the water at $T = 293K$ and $T = 348K$. However, there is a difference in the amplitude of FFT analysis, in fact in the case of pressure (Fig.(6.15) and Fig.(6.16)), the peaks of FFT amplitude of nitrogen is compared with the picks of water. In the case of FFT images (Fig.(6.17)-(6.19)), visualization spectra show still greater changes in FFT magnitude between nitrogen and water, in particular the picks of nitrogen are even more evident than in the case of water, in fact there is a difference of three orders of magnitude. With the numerical model described before, the experimental cases of nitrogen and water have been simulated. The aim of this comparison is to explain the trend in frequency spectra obtained experimentally. The operating conditions of the different test cases are summarized in the Tab.(6.3). Fig.(6.20) shows bubble size distribution in the converging-diverging nozzle, experimentally analyzed. The bubble starts to grow just before the throat of the orifice. Then it reaches the maximal size before starting to oscillate in the downstream portion. According to Fig.(6.20) the thermal effects are very low in the present orifice, experimentally tested, characterized by $C_{pMIN} = -10$, and the bubble growth is similar at the different temperature. This is confirmed at the different cavitation regimes (see Fig.(6.21)). However, assuming $C_{pMIN} = -1$, the bubble expands larger in the case of cold water, as shown in Fig.(6.22). Besides, the frequency of bubble oscillation are influenced by the operating conditions. In Fig.(6.21) the frequency appears to be influenced by the different cavitating regimes, rather than by temperature difference. However at highest C_{pMIN} , the bubble frequency is very influenced also by thermal effects as shown in Fig.(6.22). In particular, in the case of cold water the maximum bubble radius is larger than the case of hot water so bubble requires more time to grow and shrink. The modeling of the thermal effects becomes important in the modeling of nitrogen, as can be seen in the comparison of Fig.(6.23) and Fig.(6.24). Fig.(6.23) shows that the bubble radius distribution of the simulations, assuming that the bubble temperature is equal to the liquid temperature $T_c = T_\infty$, has a completely different trend from the results obtained estimating the thermal effects. In particular the simulations where the temperature depression near the bubble is neglected, give a larger predicted radius. The temperature drops by some degrees in the region of bubble growth, then the temperature increases by a few degrees during the collapse, as shown in Fig.(6.25). Observing the predicted cavity extension, this is qualitatively in agreement with the experimental visualizations (see Tab.(6.4)), and in particular with the experimental

6.2. EXPERIMENTAL THERMAL EFFECT IN WATER AND CRYOGENIC CAVITATING FLOW

vapor profile (Fig.(6.26)). The experimental vapor profiles are obtained by the normalized values of the image brightness, subtracting from the brightness value of each pixel, the value of the pixel in absence of cavitation, and normalized in respect to the maximum, corresponding to vapor. Comparing the position of the bubble collapse for water and nitrogen at the operating conditions during experiments, it is clear that the collapse for the nitrogen bubble is downstream with respect to water, so it could explain the lower frequency for nitrogen experiments. Then after the first collapsing process, it is clear that bubble starts to oscillate in the downstream portion in the case of water, but in the case of nitrogen, it seems there is no oscillation effect.

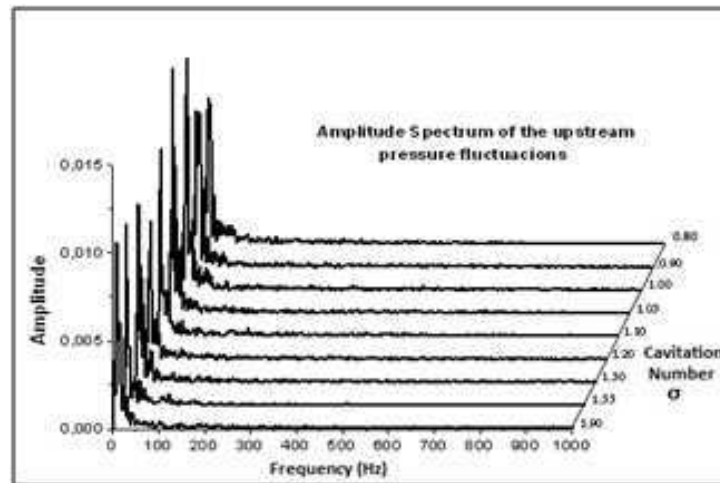


Figure 6.15: Fourier transformation (FFT) amplitude spectrum of the upstream pressure signals for the nitrogen fluid at $T = 82K$ at different cavitation numbers σ .

6.2.4 Conclusions

The present work reports the results of a cavitating converging-diverging nozzle, performed for water and nitrogen, in order to analyze thermodynamic effects encountered in cryogenic fluids. The comparison of results in nitrogen and in cold water, without thermal effects, shows differences in the frequency behavior given by FFT of pressure signals and images. In the case of cryogenic fluid, frequency peaks are shifted towards lower frequencies, with re-

6.2. EXPERIMENTAL THERMAL EFFECT IN WATER AND CRYOGENIC CAVITATING FLOW

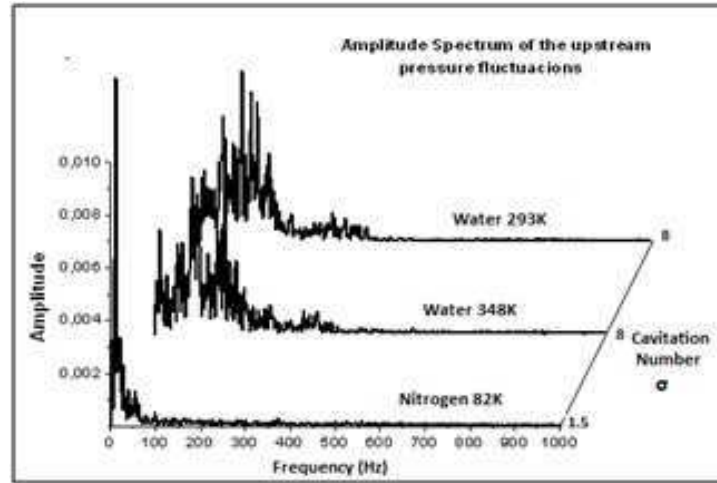


Figure 6.16: Fourier transformation (FFT) amplitude spectrum of the upstream pressure signals for the nitrogen fluid at $T = 82K$ and $\sigma = 1.55$, and for water at $\sigma = 8$ and at two different temperatures, $T = 293K$ and $T = 348K$.

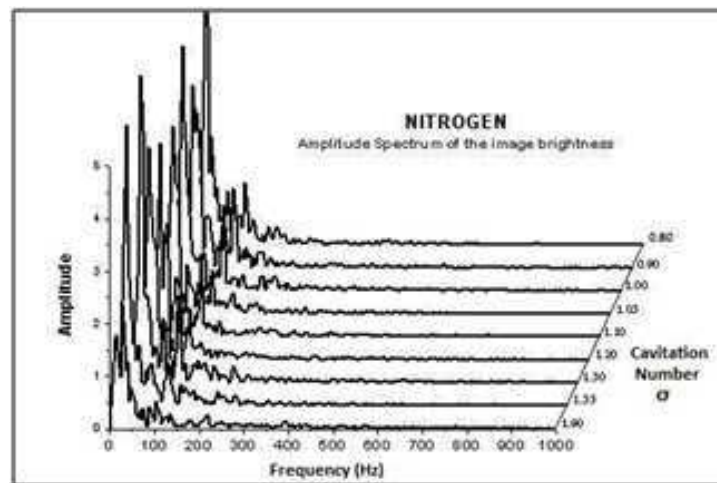


Figure 6.17: Amplitude spectrum of the image brightness for the nitrogen fluid at $T = 82K$ at different cavitation numbers.

6.2. EXPERIMENTAL THERMAL EFFECT IN WATER AND CRYOGENIC CAVITATING FLOW

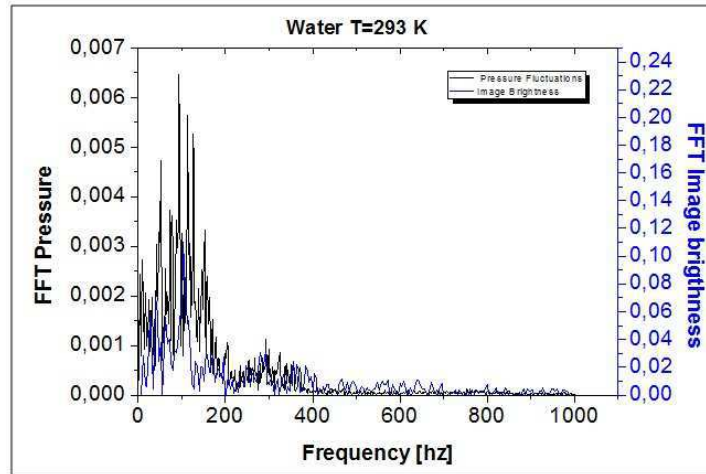


Figure 6.18: Comparison between the FFT image brightness and the FFT of pressure signals for water at $T = 293K$ and at $\sigma = 8.0$.

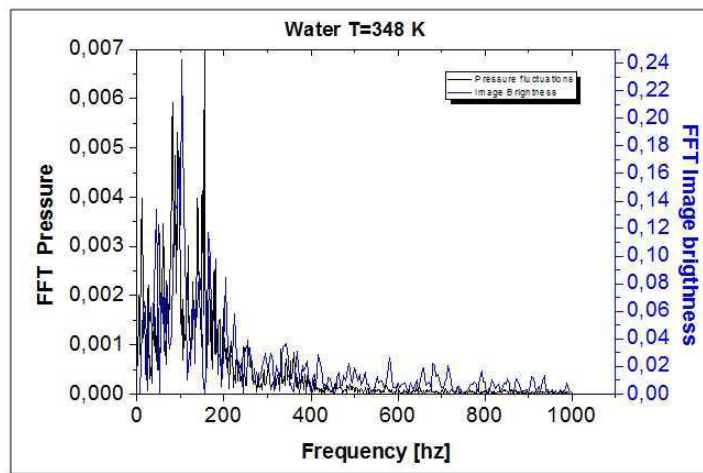


Figure 6.19: Comparison between the FFT image brightness and the FFT of pressure signals for water at $T = 348K$ and at $\sigma = 8.0$.

6.2. EXPERIMENTAL THERMAL EFFECT IN WATER AND CRYOGENIC CAVITATING FLOW

<i>NITROGEN</i>						
Case	Inlet Pressure [bar]	Outlet Pressure [bar]	Vapor Pressure [bar]	T [K]	Re	σ
1	1.66	1.57	1.53	82	2423.68	1.9
2	1.89	1.80	1.53	82	4375.03	1.2
3	1.95	1.80	1.53	82	6554.84	0.8
<i>WATER</i>						
1	4.41	3.85	0.02338	293	1000	8.0
2	5.19	4.62	0.39	348	1000	8.0

Table 6.3: Test case conditions.

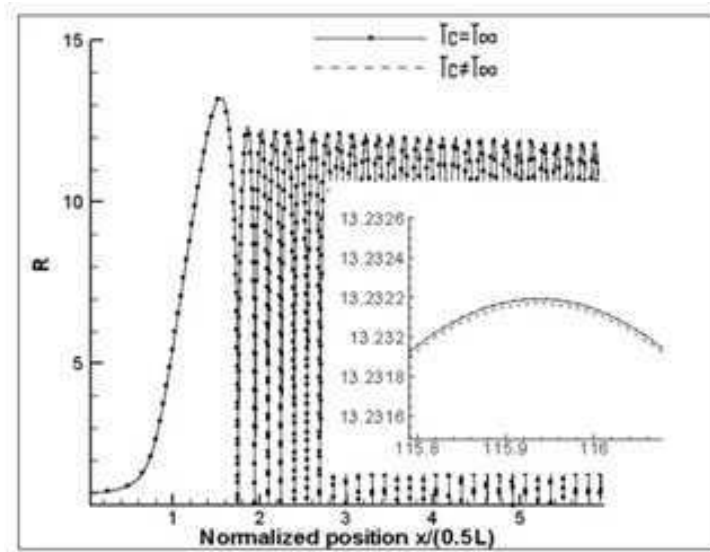


Figure 6.20: Bubble radius distributions in tested converging-diverging nozzle ($C_{pMIN} = -10$), obtained respectively by assuming $T_c = T_\infty$ and $T_c \neq T_\infty$, for water at $T = 348K$ ($Re = 1000$, $\sigma = 8$, $\alpha_0 = 5 \times 10^{-7}$, $R_0 = 0.0001$).

6.2. EXPERIMENTAL THERMAL EFFECT IN WATER AND CRYOGENIC CAVITATING FLOW

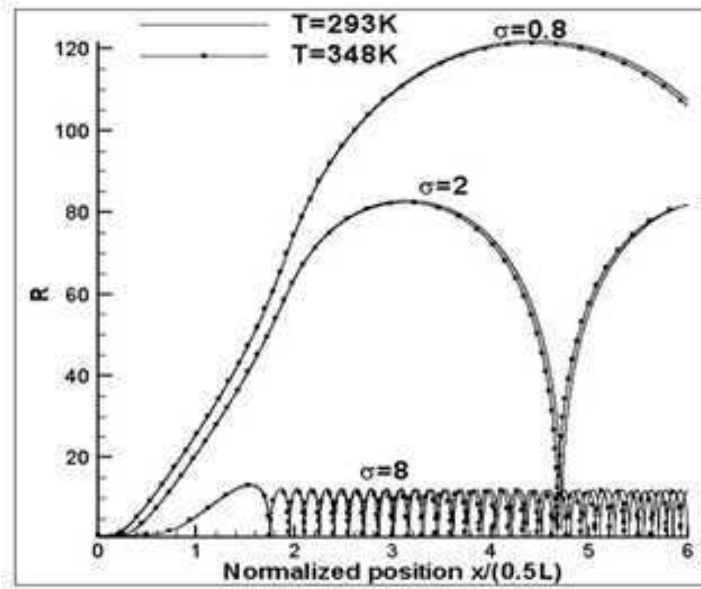


Figure 6.21: Bubble radius distributions in experimentally tested converging-diverging nozzle ($C_{pMIN} = -10$), for water at $T = 348K$ and $T = 293K$, by the isothermal calculations ($\alpha_0 = 5 \times 10^{-8}$, $R_0 = 0.0001$).




Test Case	Vapor Production	σ
1		1.9
2		1.2
3		0.8

Table 6.4: Experimental visualization of nitrogen cavitation length.

6.2. EXPERIMENTAL THERMAL EFFECT IN WATER AND CRYOGENIC CAVITATING FLOW

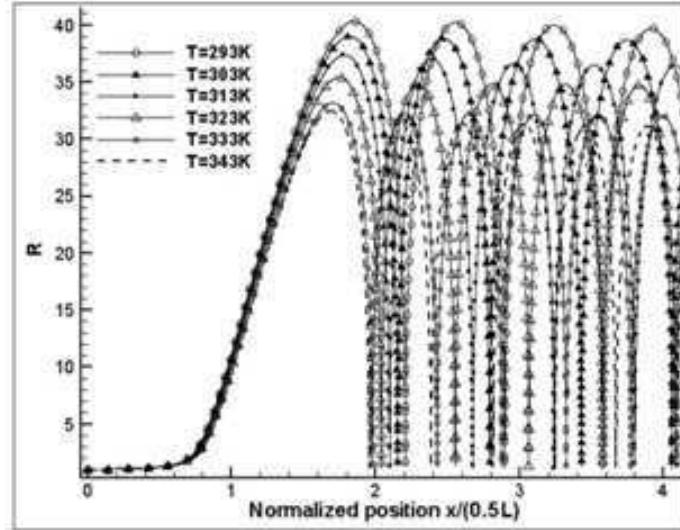


Figure 6.22: Bubble radius distributions in the nozzle ($C_{pMIN} = -1$), for water at different temperatures ($Re = 1000$, $\alpha_0 = 2.5 \times 10^{-6}$, $\sigma = 0.8$, $R_0 = 0.0001$ and $C_{pMIN} = -1$).

spect to cold water. Then the magnitude of the signal increases, in particular at low frequencies, for nitrogen and hot water. This can be due to thermal effects that also contribute to the low frequencies in the case of cryogenic fluid. To verify this assumption, a simple model based on the resolution of Rayleigh equation is used in order to analyze thermal effects in cavitation. The analytical study confirms the presence of different cavitation structure dimensions, in particular smaller bubbles for nitrogen compared to water, especially at room temperature, that are attributed to a thermodynamic effect. In the case of cold water the maximum bubble radius is larger than in hot water then bubble requires more time to grow and shrink. Comparing the position of the bubble collapse for water and nitrogen at the operating conditions during experiments, it is clear that the collapse for the nitrogen bubble is downstream with respect to water, so it could explain the lower frequency for nitrogen experiments. Then after the first collapsing process, it is clear that bubble starts to oscillate in the diverging part of the nozzle in the case of water, but in the case of nitrogen, it seems there is no oscillation effect.

6.2. EXPERIMENTAL THERMAL EFFECT IN WATER AND CRYOGENIC CAVITATING FLOW

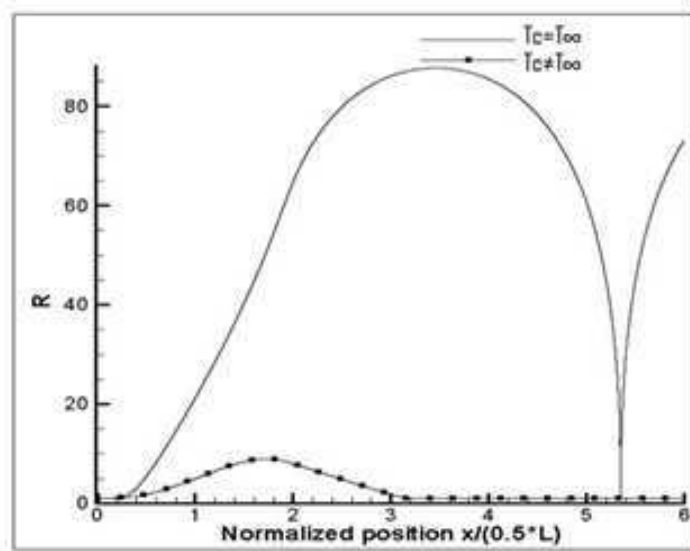


Figure 6.23: Bubble radius distributions in converging-diverging nozzle ($C_{pMIN} = -10$), obtained respectively by assuming $T_c = T_\infty$ and $T_c \neq T_\infty$, for nitrogen at $T = 82K$, $\alpha_0 = 5 \times 10^{-7}$, $R_0 = 0.0001$.

6.2. EXPERIMENTAL THERMAL EFFECT IN WATER AND CRYOGENIC CAVITATING FLOW

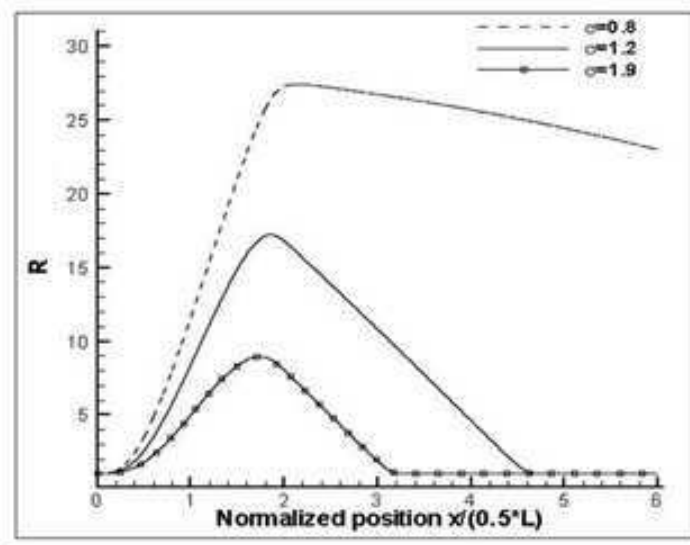


Figure 6.24: Nitrogen Bubble radius distributions in nozzle ($C_{pMIN} = -10$), obtained by assuming $T_c \neq T_\infty$ ($T = 82K$, $\alpha_0 = 5 \times 10^{-6}$, $R_0 = 0.0001$, $h_b = 5 \times 10^{+05}$).

6.2. EXPERIMENTAL THERMAL EFFECT IN WATER AND CRYOGENIC CAVITATING FLOW

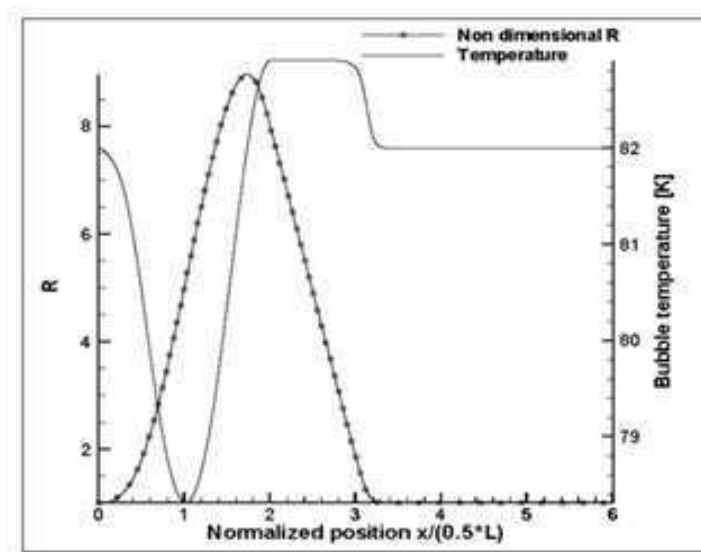


Figure 6.25: Nitrogen bubble radius and temperature distributions ($C_{pMIN} = -10$ obtained by assuming $T_c \neq T_\infty$, ($T = 82K$, $\alpha_0 = 5 \times 10^{-6}$, $R_0 = 0.0001$, $h_b = 5 \times 10^{+05}$, $\sigma = 1.9$).

6.2. EXPERIMENTAL THERMAL EFFECT IN WATER AND CRYOGENIC CAVITATING FLOW

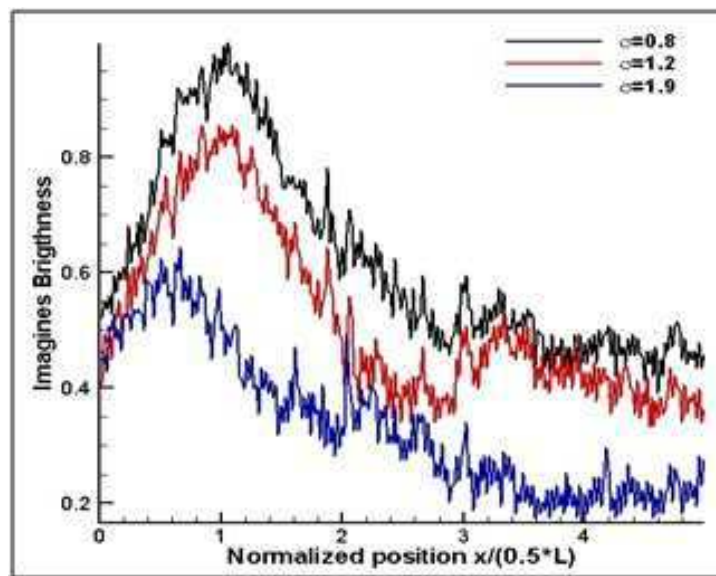


Figure 6.26: Experimental normalized image brightness, for the axial center-line, for the nitrogen fluid at $T = 82K$ at different cavitation numbers.

Chapter 7

Conclusions

This work is devoted to a better understanding of the cavitation phenomenon. More attention has been devoted to the cryogenic flows, making a comparison, when possible, with experimental data. Results presented in this work represent significant advancements with respect to previous literature. Several studies, both numerical and experimental, have been performed, permitting to achieve a set of contributions. From the numerical point of view, first, three cavitation models (the thermal equilibrium model [52], the mechanical equilibrium model [53] and the full cavitation model [54]) have been analyzed. The predictive character of these models have been already demonstrated in previous works for the water. The originality of this study consisted in coupling the cavitation model with the nucleation model (see Chapter 3) and to remove the hypothesis of isothermal phenomenon to consider the thermal effect and in order to improve the estimation of cavitation phenomenon in cryogenic flows. Accuracy of these models have been checked by a detailed comparison with experimental data [1]. Results display the importance of the choice of the cavitation model on the accuracy of the numerical simulations. In particular, the best predictions have been given by the mechanical equilibrium model (ME). Performances of the ME model have been improved by considering both nucleation and thermal effects.

Secondly, the dynamic behavior of a bubble under an oscillating pressure has been studied. The temperature during bubble collapse has been estimated and successively it has been used for the estimation of radicals production in the case of water treatment. The bubble behavior has been modeled by several forms of Rayleigh-Plesset equations, that have been implemented in an in-house numerical C code. Concerning this study, the

following contributions have been performed :

- Comparison of RP equations performance for high value of Mach number, in terms of comparison of the numerical results with experimental data.
- Study of the influence of the equation of state (Van der Waals EOS and Perfect gas EOS) of the gas in the bubble on bubble behavior.
- Proposition of a simple model for the reproduction of water treatment.

When van der Waals EOS has been used, the temperature has been estimated higher than that one obtained with the perfect gas equation. It has been observed that the compressibility hypothesis influence the bubble rebounds, except for the first collapse. Finally, the OH^- radicals have been computed using several forms of RP equations. When a van der Waals equation has been used, the computed number of radicals has been higher.

Thirdly, the thermal effect in a cryogenic cavitating flow, has been taken into account by means of the study of convective heat transfer coefficient h_b . The originality of this study consisted in the full analysis on h_b that allows understanding a physical aspect of cavitation phenomenon and determining the best model for the estimation of h_b in hydrogen cavitating flows. A sensitivity analysis of the convective heat transfer coefficient, in cryogenic flows, has been performed in order to identify the mechanisms governing the bubble growth. For all tested cases the coefficient h_b has been varied between 1×10^{10} and 1×10^{03} and for each h_b , the upstream vapor fraction α_0 has been varied between 1×10^{-10} and 1×10^{-03} . In order to analyze qualitatively the results, for each case, several parameters, *i.e.* h_{bMAX} , h_{bOPT} and h_{bMIN} , have been identified, representing, respectively, the minimal value, for which, the growth is governed exclusively by mechanical forces, the range of values permitting to obtain the best comparison with respect to experimental data and the maximum value, for which the growth is governed exclusively by thermal effects (obviously $h_{bMIN} < h_{bMAX}$). Then, three models, *i.e.* *Ranz and Marshall model* [5], *Oresta model* [6] and *Christopher model* [7], for the convective heat transfer coefficient have been analyzed. These models have been implemented in a commercial CFD code and validated by comparing with the experimental case described in [1]. The most important conclusions of the present work are the following:

-
- An over-estimation of h_b could motivate that the bubble growth is governed by mechanical forces producing an increase of vapor fraction and a negligible temperature drop in the throat. Conversely an under-estimation could motivate that the bubble growth is governed by thermal force producing a good estimation of temperature drop even with a bad estimation of vapor fraction.
 - There is an optimal range for hydrogen cavitating flow that is about $1 \times 10^{05} < h_b < 1 \times 10^{06}$, then it is better to adopt a model for the estimation of h_b coefficient.
 - In all cases the optimal h_b is closed to h_{bMIN} , assessing that in hydrogen cavitating flow the growth of bubbles is more controlled by thermal effect than mechanical force.
 - The optimal value of h_b is more influenced by inlet temperature T_0 and by cavitation number σ , than Reynolds number.
 - From comparison between the three models, Oresta and Christopher model give a good estimation of temperature drop. The Ranz and Marshall model gives an error more elevated compared to the other two models in terms of estimation of temperature drop in the throat and liquid pressure in the Venturi.
 - When these models have been used in the commercial code, the importance of a good choice of convective heat transfer coefficient showed to be more evident during the evaporation, while it is negligible during the collapse, because the two models give the same temperature results.

From the experimental point of view, an experimental apparatus has been set up in the laboratory of University of Salento in order to investigate the cavitating flows in nitrogen and in water and in order to study experimentally the nucleation in cryogenic flows and the influence of thermal effect. The experimental set-up allows a visualization of the phenomenon by means of a CCD camera and a constant monitoring of pressure by means of pressure sensors. Pressure signals have been analyzed both in time domain and in frequency domain, in order to characterize the cavitating cryogenic flows in terms of time occurrence, space, and intensity for various hydrodynamic conditions. Several configurations of convergent-divergent nozzle have been designed and tested in the apparatus. The concentration of activated bubbles

nuclei has been obtained. An increase of nuclei due to a decrease of cavitation number has been observed. Then the standard deviation of the pressure signals, recorded downstream the restricted nozzle area has been studied in order to obtain an evaluation about the oscillation of pressure signals due the development of cavitation. By means of the Fourier Transform, it has been possible to locate a range of characteristic frequencies for the upstream and downstream pressures. In the case of cryogenic flows, it has been observed that the frequency peaks are shifted towards lower frequencies, with respect to cold water. Then the magnitude of the signal increases, in particular at low frequencies, for nitrogen and hot water. This can be due to thermal effects that also contribute to the low frequencies in the case of cryogenic fluid. To verify this assumption, some cases has been numerically simulated with the cavitation models studied in this work.

Appendix A

Classical Equation of Rayleigh-Plesset

A bubble with initial radius R_0 is in equilibrium with a liquid at constant temperature T_∞ . Neglecting the liquid energy equation, because the liquid is at constant temperature, the liquid mass and momentum conservative equations are:

$$\rho \left[\frac{\partial u}{\partial t} + u \cdot \nabla u \right] = -\nabla p + \mu \nabla^2 u + \zeta \nabla \nabla \cdot u$$
$$\frac{\partial \rho h_0}{\partial t} + \nabla \cdot (\rho u) = 0$$

where u is the liquid velocity, ρ the liquid density, p the liquid pressure, μ the molecular viscosity and ζ is volume viscosity. Let us suppose that:

- the viscosity is negligible $\rightarrow \mu \nabla^2 u = 0$
- the field of fluid velocity is only radial, the velocity has only one component on $r \rightarrow u(r, \theta, \varphi) = u(r, 0, 0)$, that allows computing the second term in the left part of Eq.(A) as following :

$$(u \cdot \nabla)u = \left[u_r \frac{\partial u_r}{\partial r} + u_\theta \frac{\partial u_\theta}{\partial \theta} + u_\varphi \frac{\partial u_\varphi}{\partial \varphi} \right] = u_r \frac{\partial u_r}{\partial r} = \frac{1}{2} \frac{\partial u_r^2}{\partial r} \quad (\text{A.1})$$

The velocity can be represented by a potential $u = \nabla\phi = \frac{\partial\phi}{\partial r}$ where the flux is irrotational $\rightarrow \nabla\nabla \cdot u = 0$. The Eq.(A) becomes:

$$\rho \left[\frac{\partial}{\partial r} \left(\frac{\partial\phi}{\partial t} \right) + \frac{1}{2} \frac{\partial}{\partial r} \left(\frac{\partial\phi}{\partial r} \right)^2 \right] = -\frac{\partial p}{\partial r} \frac{\partial\rho}{\partial t} + \nabla\phi\nabla\rho + \rho\nabla \cdot (\nabla\phi) = 0 \quad (\text{A.2})$$

that can be written as:

$$\begin{aligned} \rho \left[\left(\frac{\partial\phi}{\partial t} \right) + \frac{1}{2} \left(\frac{\partial\phi}{\partial r} \right)^2 \right] &= -p \\ \frac{\partial\rho}{\partial t} + \frac{\partial\phi}{\partial r} \frac{\partial\rho}{\partial r} + \rho\nabla^2\phi &= 0 \end{aligned}$$

Introducing the enthalpy in the conservative equations (Eq.(A)) $dH = dp/\rho = (dp/d\rho)(d\rho/\rho) = c^2 d\rho/\rho$:

$$\nabla^2\phi = \left[\frac{u}{c^2} \left(\frac{\partial u}{\partial t} - \frac{\partial H}{\partial r} \right) \right] + \frac{1}{c^2} \frac{\partial^2\phi}{\partial t^2} \quad (\text{A.3})$$

Close to the bubble, the Laplace operator could be applied to the potential ($\nabla^2\phi = 0$) and the term $(1/c^2)\partial_t^2\phi$ is negligible. The solution that satisfies the bubble interface condition $\partial_r\phi(r = R) = \dot{R}$ is :

$$\phi = \phi_\infty(t) - \frac{1}{r}F(t - r/c) \approx \phi_\infty(t) - \frac{1}{r}F(t) + \frac{\dot{F}}{c} \quad (\text{A.4})$$

where the function $F(t) = R^2(\partial R/\partial t) = R^2\dot{R}$, $\phi_\infty(t)$ is the bubble potential law, c is the speed of sound and the last term is:

$$\frac{\dot{F}}{c} = \left(\frac{2R\dot{R}^2 + R^2\ddot{R}}{c} \right) = \left(\frac{2R\dot{R}^2 + R^2\ddot{R}}{v\lambda} \right) \quad (\text{A.5})$$

Supposing the bubble radius is lower than sound wavelength ($R \ll \lambda$), the last term of Eq.(A.4) is negligible (see Eq.(A.5)) and the Eq.(A.4) becomes :

$$\phi = \frac{R^2\dot{R}}{r} + \phi_\infty(t) \quad (\text{A.6})$$

This condition is applied if the radial sound effect of bubble is neglected, on the contrary in the absence of this hypothesis, the potential is :

$$\phi = -\frac{R^2\dot{R}}{r} + \phi_\infty(t) + \frac{d(R^2\dot{R})}{dt} \quad (\text{A.7})$$

Replacing the Eq.(A.7) in Eq.(A.3) and supposing the pressure close to the bubble is $p = -\rho\partial_t\phi_\infty = P_0 + P_{ext}(t)$ with $P_{ext}(t) = -P_a \sin(\varpi t)$, the Eq.(A.3) becomes:

$$\frac{\partial}{\partial t} \left[-\frac{R^2 \dot{R}}{r} + \phi_\infty(t) \right] + \frac{1}{2} \frac{\partial}{\partial r} \left[-\frac{R^2 \dot{R}}{r} + \phi_\infty(t) \right]^2 = -\frac{p[R(t)]}{\rho} \quad (\text{A.8})$$

where $p[R(t)]$ is the bubble interface pressure in the liquid side. Developing the derivatives in Eq.(A.7) the following equation is obtained:

$$-\frac{R^2 \ddot{R}}{r} - \frac{\dot{R}}{r} (2R\dot{R}) - \frac{1}{\rho} [P_0 + P_{ext}(t)] + \frac{1}{2} \frac{R^4 \dot{R}^2}{r^4} = -p[R(t)] \quad (\text{A.9})$$

On the interface $r = R$ the Eq.(A.9) becomes :

$$R^2 \ddot{R} + \frac{3}{2} \dot{R}^2 = \frac{1}{\rho} [-P_0 - P_{ext} + p[R(t)]] \quad (\text{A.10})$$

The pressure $p[R(t)]$ can be defined by the force balance at the interface that satisfies the general form of Laplace law: At the interface $r = R$ the Eq.(A.9) becomes :

$$p_g(t) + \sum_{rr} [r = R(t)] = p_g(t) - p[R(t)] + 2\mu \frac{\partial u}{\partial r} (r = R) = p_g(t) - p[R(t)] + 4\mu \frac{\dot{R}}{R} = 2 \frac{\sigma}{R} \quad (\text{A.11})$$

where \sum_{rr} is the radial component of stress tensor in the liquid, σ is the surface tension of liquid-gas interface and p_g is the gas pressure. Then, the Eq.(A.11) becomes :

$$rho \left[R^2 \ddot{R} + \frac{3}{2} \dot{R}^2 \right] = P_g - P_0 - P_{ext} - \frac{2\sigma}{R} - \frac{4\mu \dot{R}}{R} \quad (\text{A.12})$$

Appendix B

Rayleigh-Plesset equation with compressible effect

The equation A14 has been obtained with the hypothesis that the radial sound effect of bubble can be neglected. When this hypothesis is not true, the potential is expressed by Eq.(A.7) that substituted in Eq.(A.3) becomes:

$$\frac{\partial}{\partial t} \left[-\frac{R^2 \dot{R}}{r} + \phi_\infty(t) + \frac{1}{c} \frac{d(R^2 \dot{R})}{dt} \right] + \frac{1}{2} \frac{\partial}{\partial r} \left[-\frac{R^2 \dot{R}}{r} + \phi_\infty(t) \frac{1}{c} \frac{d(R^2 \dot{R})}{dt} \right]^2 = -\frac{p[R(t)]}{\rho}. \quad (\text{B.1})$$

Developing the derivatives, the Eq.(B.1) becomes :

$$-\frac{R^2 \ddot{R}}{r} + \frac{\dot{R}}{r} (2R\dot{R}) - \frac{1}{\rho} [P_0 + P_{ext}] + \frac{1}{c} \frac{d(R^2 \dot{R})}{dt} + \frac{1}{2} \frac{R^4 \dot{R}^2}{r^4} = \frac{p[R(t)]}{\rho}. \quad (\text{B.2})$$

If $r = R$ replacing the Eq.(A.10), the Eq.(B.2) becomes:

$$\rho \left[R^2 \ddot{R} + \frac{3}{2} \dot{R}^2 \right] = P_g - P_0 - P_{ext}(t) - \frac{2\sigma}{R} - \frac{4\mu\dot{R}}{R} + \frac{\rho}{c} \frac{d^2}{dt^2} (R^2 \dot{R}). \quad (\text{B.3})$$

It is possible to evaluate the importance of compressible effect, comparing the magnitude order of the last term on the right and of the inertial term on the left. It is possible to introduce the ratio between these two terms presenting an order of \dot{R}/c , that is similar to Mach number. This term is negligible when the interface velocity ($dR/dt = \dot{R}$) is lower than speed of sound. By using the compressible term, the Rayleigh-Plesset equation becomes a three-order equation, though the initial condition are expressed

only for R and for \dot{R} . This happens because the term \ddot{R} is chosen to remove the unstable solution of Eq.(B.3). A method is to compute the last term of Eq.(B.3) using always the Rayleigh-Plesset equation. Yuan et al.[16] gives a good explanation of all the system of equations that can be obtained and that are used in this work. The first equation is called RP1 and it has been obtained by Rayleigh, Plesset, Noltingk et Probstsky and then modified by Keller et Kolodner[57]:

$$R\ddot{R} + \frac{3}{2}\dot{R}^2 = \frac{1}{\rho_{l\infty}} \left(P_g(R, t) - P_0 - P_{ext}(t) - \frac{2\sigma}{R} - \frac{4\mu\dot{R}}{R} \right) + \frac{t_R}{\rho_{l\infty}} \frac{d}{dt} [P_g(R, t) - P_{ext}(t)], \quad (\text{B.4})$$

with $t_R = R/c_{l\infty}$, $c_{l\infty}$ is the speed of sound at room condition. The second equation, RP2, comes from the formulation of Keller-Miksis [58]:

$$(1-M)R\ddot{R} + \frac{3}{2} \left(1 - \frac{M}{3} \right) \dot{R}^2 = \frac{1}{\rho_{l\infty}} (1+M) [P(R(t)) - P_0 - P_{ext}(t + t_R)] + \frac{t_R}{\rho_{l\infty}} \frac{dP(R(t))}{dt} \quad (\text{B.5})$$

where $M = \ddot{R}/c_{l\infty}$. The equation RP3 [28] is :

$$(1-M)R\ddot{R} + \frac{3}{2} \left(1 - \frac{M}{3} \right) \dot{R}^2 = (1+M) \left[H_b - \frac{1}{\rho_l} P(t + t_R) \right] + t_R \frac{dH_b}{dt} \quad (\text{B.6})$$

where ρ_l , H_b are, respectively the density and the enthalpy of liquid phase that are defined:

$$c_l^2 \equiv \frac{dP}{d\rho_l} \quad \text{and} \quad H_b \equiv \int_{P_\infty}^P \frac{dP}{\rho_l} \quad (\text{B.7})$$

For water, the Tait EOS gives an expression of ρ_l and H_b :

$$\frac{P+B}{P_\infty+B} \equiv \left(\frac{\rho_l}{\rho_{l\infty}} \right)^n \quad (\text{B.8})$$

where $B=3049.13$ and $n=7.15$, for water at 10^5 bar . Replacing the Eq.(B.8) in Eq.(B.7), this one becomes :

$$c_l^2 = \frac{n(P+B)}{\rho_l} \quad \text{and} \quad H_b = \frac{n}{n-1} \left(\frac{(P+B)}{\rho_l} - \frac{(P_\infty+B)}{\rho_{l\infty}} \right). \quad (\text{B.9})$$

Bibliography

- [1] J. Hord. Cavitation in liquid cryogenics, i-venturi. Nasa cr-2054, 1973.
- [2] T.G. Leighton. *The acoustic Bubble*. ACADEMIC PRESS LIMITED, 1994.
- [3] R.Lofstedt, B.P.Barber, and S.J.Putterman. Toward a hydrodynamic theory of sonoluminescence. *Phys. Fluid A*, 5, 1993.
- [4] L.Yuan, H.Y.Cheng, M.-C.Chu, and P.T.Leung. Physical parameters affecting sonoluminescence: A self-consistent hydrodynamic study. *Physical Review E*, 58:2705–2708, 1998.
- [5] W.E. Ranz and W.R. Marshall. Analysis evaporation from drops. *Chemical Engineering Progress*, 48:141–146, 1952.
- [6] P. Oresta, R. Verzicco, D. Lohse, and A. Prosperetti. Heat transfer mechanisms in bubbly rayleigh-bnard convection. *Physical Review E*, 80:026304–026314, 2009.
- [7] D.M. Christopher, H. Wang, and X. Peng. Numerical analysis of the dynamics of moving vapor bubbles. *International Journal of Heat and Mass Transfer*, 49:3626–3633, 2006.
- [8] J.P.Franc, F.Avellan, B.Belahadji, and et al. *La Cavitation - Mecanismes physiques et aspects industriels*. Presses Universitaires de Grenoble, 1995.
- [9] C.E. Brennen. *Cavitation and Bubble Dynamic*. Oxford University Press, 1995. ISBN 0-19-509409-3.

BIBLIOGRAPHY

- [10] Y. Utturkar, J. Wua, G. Wang, and W. Shyy. Recent progress in modeling of cryogenic cavitation for liquid rocket propulsion.
- [11] B.D.Storey and A.J.Szeri. Mixture segregation within sonoluminescence bubbles. *J. Fluid Mech.*, 396:203–221, 1999.
- [12] S. Watanabe, A. Furukawa, and Y. Yoshida. Theoretical analysis of thermodynamic effect of cavitation in cryogenic inducer using singularity method. *International Journal of Rotating Machinery*, 2008:1–8, 2008.
- [13] E. Goncalves and R. Fortes Patella. Analysis of thermal effects in a cavitating orifice using rayleigh equation and experiments. *Computers & Fluids*, 39:99–113, 2009.
- [14] J.P. Franc and C. Pellone. Analysis of thermal effects in a cavitating inducer using rayleigh equation. *J. Fluids Engineering*, 129:914–983, 2007.
- [15] M.Deshpande, J.Feng, and C.L. Merkle. Numerical modeling of the thermodynamic effects of cavitation. *Journal of Fluid Engineering*, 119:420–427, 1997.
- [16] R. Saurel and O. Le Metayer. A multiphase model for compressible flows with interfaces, shocks, detonation waves and cavitation. *Journal of Fluid Mechanics*, 431:239–273, 2001.
- [17] R. Saurel, F. Petiptas, and R. Abgrall. Modelling phase transition in metastable liquids: application to cavitating and flashing flows. *J. Fluid Mech*, 601:313–350, 2008.
- [18] R. Becker and W. Dring. Knetische behandlung der keimbildung in berstigten dmpfen. *Annalen der Physik*, 19, 135.
- [19] P. Deligiannis and J.W. Cleaver. The role of nucleation in the initial phases of a rapid depressurization of a subcooled liquid. *International Journal of Multiphase Flow*, 16:975–984, 1990.

BIBLIOGRAPHY

- [20] M. Sedl, P. Zima, T. Nec, and F. Mark. Analysis of cavitation phenomena in water and its application to prediction of cavitation erosion in hydraulic machinery. In *ICPWS XV*, 2008.
- [21] M. Guilleumas, M. Pi, M. Barranco, D. M. Jezek, and Jess Navarro. Nucleation in supersaturated solutions of ^3He in ^4He at negative pressures. *Phys. Rev*, 1995.
- [22] J. Dupont-Roca, M. Himberta, N. Pavloffb, and J. Treinerb. Liquid ^3He : A density functional approach with a finite range interaction. In *Proceedings of the 19th International Conference on Low Temperature Physics*, volume 165, 1990.
- [23] D. W. Oxtoby. Nucleation in supersaturated solutions of ^3He in ^4He at negative pressures. *Accounts of Chemical Research*, 31, 1998.
- [24] X. C. Zeng, D.W. Oxtoby, and E. Chengz. Thermal nucleation and cavitation in helium-3 fluids. *J. Chem. Phys.*, 104, 1996.
- [25] S. Tsuda, T. Tokumasu, and K. Kamijo. A molecular dynamics study of bubble nucleation in liquid oxygen with impurities. *Heat Transfer-Asian Research*, 34, 2005.
- [26] M.G. De Giorgi, A. Ficarella, and M.G. Rodio. Cavitation modeling in cryogenic fluid for liquid rocket engine applications. In *AIAA-2008-3842*. AIAA, 2008.
- [27] A. Prosperetti, L. Crun, and K. Commander. Nonlinear bubbles dynamics. *J. Acoust. Soc. Am.*, 83:502–514, 1988.
- [28] F.N. Eglafopoulos V. Kamath, A. Prosperetti. A theoretical study of sonoluminescence. *J. Acoust. Soc. Am.*, 94:248–260, 1993.
- [29] K. Yasui. Effects of thermal conduction on bubble dynamics near the sonoluminescence threshold. *J. Acoust. Soc. Am.*, 98, 1995.
- [30] K. Yasui. Chemical reactions in a sonoluminescing bubble. *Journal of Physical Society of Japan*, 66:2911–2920, 1997.

BIBLIOGRAPHY

- [31] K.Yasui, T.Tuziuti, M.Sivakumar, and Y.Iida. Theoretical study of single-bubble sonochemistry. *J. Chem. Phys.*, 109:4869–4872, 2005.
- [32] S.Sochard, A.M.Wilhelm, and H.Delmas. Modelling of free radicals production in a collapsing gas-vapour bubble. *Ultrasonics Sonochemistry*, 4:77–84, 1997.
- [33] H.Lin, B.D.Storey, and A.J.Szeri. Inertially driven inhomogeneities in violently collapsing bubbles: the validity of rayleigh-plesset equation. *J. Fluid Mech.*, 452:145–162, 2002.
- [34] N.Xu, R.E. Apfel, A.Khong, X.Hu, and L.Wang. Water vapor diffusion effects on gas dynamics in a sonoluminescing bubble. *Phys. Rev. E*, 68, 2003.
- [35] B.D.Storey and A.J.Szeri. Water vapour, sonoluminescence et sonochemistry. *Proc. R. Soc. Lond.*, 456:1685–1709, 2000.
- [36] B.D.Storey and A.J.Szeri. Argon rectification and the cause of light emission in single-bubble sonoluminescence. *Physical Review Letters*, 88, 2002.
- [37] G.Hauke, D.Fuster, and C.Dopazo. Dynamics of a single cavitating and reacting bubble. *Physical Review E*, 75, 2009.
- [38] H.A. Stahl, A.J. Stepanoff, and N.J. Phillipsburg. Thermodynamic aspects of cavitation in centrifugal pumps. *ASME Journal Basic Eng*, 78:1691,1693, 1956.
- [39] A.J. Stepanoff. Cavitation properties of liquids. *Journal Eng. Power*, 1964.
- [40] E. Raposselli and L. d’Agostino. A barotropic cavitation model with thermodynamic effects. In *CAV 2006 Symposium*. CAV 2006, 2006.
- [41] P. Cooper. Analysis of single and two-phase flow in turbopump inducer. *J. Eng. Power*, 89:577–588, 1967.

BIBLIOGRAPHY

- [42] J. Rolland, G. Boitel, S. Barre, E. Goncalves, and R. Fortes Patella. Experiments and modelling of cavitating flows in venturi. part i: stable cavitation. In *CAV 2006 Symposium*. CAV 2006, 2006.
- [43] T. Goel, S. Thakur, R.T. Haftka, W. Shyy, and J. Zhao. Surrogate model-based strategy for cryogenic cavitation model validation and sensitivity evaluation. *Int. J. Numer Meth Fluids*, 58:969–1007, 2008.
- [44] C-C. Tseng and W. Shyyb. Modeling for isothermal and cryogenic cavitation. *International Journal of Heat and Mass Transfer*, 53(2):513–525, 2010.
- [45] X.B. Zhang, L.M.Qiu, Y.Gao, and X.J.Zhang. Computational fluid dynamic study on cavitation in liquid nitrogen. *Cryogenics*, 48:432–438, 2008.
- [46] S.L. Qi, P.Zhang, R.Z. Wang, and L.X. Xu. Flow boiling of liquid nitrogen in micro-tubes:partii-heat transfer characteristics and critical heat flux. *International Journal of Heat and Mass Transfer*, 50:5017–5030, 2007.
- [47] S.K. Kim and G.C. Park. Interfacial heat transfer of condensing bubble in subcooled boiling flow. *International Journal of Heat and Mass Transfer*, 54:2962–2974, 2011.
- [48] K. Oh, S.H. Park, and Y.I. Cho. A study of the effect of ultrasonic vibrations on phase change heat transfer. *Int. J. Heat Mass Transfer*, 45:4631–4641, 2002.
- [49] S. Komarov and M. Hirasawa. Enhancement of gas phase heat transfer by acoustic field application. *International Journal of Heat and Mass Transfer*, 41:289–293, 2003.
- [50] J. Cai, X. Huai, R. Yan, and Y.Cheng. Numerical simulation on enhancement of natural convection heat transfer by acoustic cavitation in a square enclosure. *Applied Thermal Engineering*, 29:1973–1982, 2009.

BIBLIOGRAPHY

- [51] D. W. Zhou. Heat transfer enhancement of copper nanofluid with acoustic cavitation. *International Journal of Heat and Mass Transfer*, 47:3109–3111, 2004.
- [52] F.R. Young. *Cavitation*. McGraw-Hill Book Company, 1989.
- [53] M.G. De Giorgi, A. Ficarella, and F. Chiara. Experimental and numerical investigations of cavitating flows. In *Fluid Dynamics Conference 35th AIAA*, 2005.
- [54] A.K. Singhal, M. M. Athavale, H. Li, and Y. Jiang. Mathematical basis and validation of the full cavitation model. *Journal of Fluid Engineering*, 124:617–624, 2002.
- [55] M. Ishii, S. J. Kataoka, and G. Kocamustafaogullari. The importance of the interfacial area in two phase flow analysis. In *9th U.S natn. Congr. of Applied Mechanics*, pages 73–80, 1982.
- [56] G. Kocamustafaogullari and M. Ishii. Interfacial area and nucleation site density in boiling systems. *International Journal of Heat and Mass Transfer*, 26:1377–1387, 1983.
- [57] J.B.Keller and I.I.Kolodner. *J. Appl. Phys.*, 27, 1956.
- [58] J.B.Keller and M. Miksis. *J. Acoust. Soc. Am*, 68, 1980.
- [59] J.H.Mathews and K.K.Fink. *Numerical Methodes Using Matlab, fourth edition*. Prentice-Hall Inc.
- [60] S.Gottlieb and C-W.Shu. Total variation diminishing runge-kutta schemes. *Mathematics of computation*, 67, 1998.
- [61] *ANSYS FLUENT 12.0, Theory Guide*. Ansys, Inc, 2009.
- [62] Y.C. Wang and C.E.Brennen. One-dimensional bubbly cavitating flows through a converging-diverging nozzle. *Journal of Fluids Engineering*, 120:166, 170, 1998.

BIBLIOGRAPHY

- [63] Y.C. Wang. *Shock Waves In Bubbly Cavitating Flows*. PhD thesis, California Institute of Technology, California, 1996.
- [64] M.G. De Giorgi, D. Bello, and A. Ficarella. Analysis of thermal effects in a cavitating orifice using rayleigh equation and experiments. *Journal of Engineering for Gas Turbines and Power*, 132:092901(1)–092901(10), 2010.
- [65] K. Kikuta, Y. Yoshida, M. Watanabe, and T. Hashimoto. Thermodynamic effect on cavitation performances and cavitation instabilities in an inducer. *Journal of Fluids Engineering*, 130:111302–111307, 2008.
- [66] M.G. De Giorgi, P.M. Congedo, M.G. Rodio, and A. Ficarella. Shape optimization for cryogenic cavitating flows past an isolated hydrofoil. In *FEDSM2008-55119*. ASME, 2008.
- [67] X. Li, R. Wang, R. Huang, and Y. Shi. Numerical investigation of boiling flow of nitrogen in a vertical tube using the two-fluid model. *Applied Thermal Engineering*, 26:2425–2432, 2006.
- [68] M.G. De Giorgi and A. Ficarella. Simulation of cryogenic cavitation by using both inertial and heat transfer control bubble growth. In *AIAA-2009-4039*. AIAA, 2009.
- [69] D. Albagli and A. Gany. High speed bubbly nozzle flow with heat, mass, and momentum interactions. *International Journal of Heat and Mass Transfer*, 46:1993–2003, 2003.
- [70] J.C. Butcher. *Numerical Methods for Ordinary Differential Equation*. John Wiley & Sons, 2003.
- [71] M.G. De Giorgi, M.G. Rodio, and A. Ficarella. Thermodynamic effect on cavitation in water and cryogenic fluids. In *ESDA2010-24694*. ASME, 2010.
- [72] B. E. Launder and D. B. Spalding. The numerical computation of turbulent flows. *Computer Methods in Applied Mechanics and Engineering*, 3:269289, 1974.

BIBLIOGRAPHY

- [73] G.H. Schnerr and J. Sauer. Physical and numerical modeling of unsteady cavitation dynamics. In *International Conference on Multiphase Flow*. Martin-Luther-Universitt Halle-Wittenberg, 2001.
- [74] P.J. Roache. *Verification and Validation in Computational Science and Engineering*. Hermosa Publishers, 1998. Albuquerque, New Mexico.
- [75] T. M. Flynn. In *Cryogenic Engineering*, pages 68–73. CRYOCO, Inc. Lousville, Colorado, USA.
- [76] M.S. Plesset and Zwick S.A. A nonsteady heat diffusion problem with spherical symmetry. *J. Appl. Phys*, 23:95–98, 1952.